LBL-22936

Lawrence Berkeley Laboratory

UNIVERSITY OF CALIFORNIA

Materials & Chemical Sciences Division

RECEIVED
APR 22 1987

Center for Advanced Materials

MEASUREMENT OF DOPANT CONCENTRATION AND LATTICE POSITION IN LEC GaAs BY COMBINED PARTICLE-INDUCED X-RAY EMISSION AND RUTHERFORD BACKSCATTERING TECHNIQUES

J.H. Madok
(M.S. Thesis)

December 1986

TWO-WEEK LOAN COPY

This is a Library Circulating Copy which may be borrowed for two weeks.

Prepared for the U.S. Department of Energy under Contract DE-AC03-76SF00098

LBL-22936 c.2

DISCLAIMER

This document was prepared as an account of work sponsored by the United States Government. While this document is believed to contain correct information, neither the United States Government nor any agency thereof, nor the Regents of the University of California, nor any of their employees, makes any warranty, express or implied, or assumes any legal responsibility for the accuracy, completeness, or usefulness of any information, apparatus, product, or process disclosed, or represents that its use would not infringe privately owned rights. Reference herein to any specific commercial product, process, or service by its trade name, trademark, manufacturer, or otherwise, does not necessarily constitute or imply its endorsement, recommendation, or favoring by the United States Government or any agency thereof, or the Regents of the University of California. The views and opinions of authors expressed herein do not necessarily state or reflect those of the United States Government or any agency thereof or the Regents of the University of California.

LBL-22936

MEASUREMENT OF DOPANT CONCENTRATION AND LATTICE POSITION IN LEC GaAs BY COMBINED PARTICLE-INDUCED X-RAY EMISSION AND RUTHERFORD BACKSCATTERING TECHNIQUES

John Hamilton Madok

Center for Advanced Materials
Lawrence Berkeley Laboratory
and
Department of Materials Science and Mineral Engineering
University of California
Berkeley, California 94720

December 1986

This work was supported by the Director, Office of Energy Research, Office of Basic Energy Sciences, Materials Science Division of the U.S. Department of Energy under Contract DE-AC03-76SF00098.

ABSTRACT

The use of Particle-Induced X-Ray Emission (PIXE) to characterize electronic materials has advantages over the Rutherford Backscattering (RBS) technique. The major advantage is the ability to characterize impurities which are of either similar mass or of less mass than the target atoms, as well as those which are heavier than the target. When combined with RBS channeling measurements, PIXE can be used to extend the range of dopants whose lattice position can be studied. Furthermore, PIXE can be used to determine the specific sublattice site of impurities in III-V compounds.

A scattering chamber which provides the capability to perform both PIXE and RBS measurements simultaneously was constructed. A series of experiments were carried out in which the experimental and data analysis procedures were standardized. Dopant concentration measurements of LEC GaAs show that concentrations can be measured with a 5 uncertainty and that fluctuations in concentration of 8-10 in 1 mm along a bulk crystal can be determined. The minimum detectable limit of the PIXE technique when employing 1.0 and 1.5 MeV protons for a wide range of impurities in bulk GaAs was investigated. PIXE analysis was performed in conjunction with RBS measurements to investigate the lattice position of In, Zn, and Si in as-grown crystals by the channeling technique.

Acknowledgements

I would like to give my most sincere thanks to Professor Eugene E. Haller for giving me the opportunity to explore new challenges over the past two years. I am especially grateful to Dr. Joseph M. Jaklevic for his supervision, time and patience, and most of all, for sharing his knowledge and experience with me so that this project would be a success.

Special thanks to Professor Eicke Weber of the Department of Materials Science and Mineral Engineering and to Professor Boris Rubinsky of the Mechanical Engineering Department for reviewing and making valuable comments on this thesis.

I am appreciative of the technical assistance of W. L. Searles of the Department of Instrument Science and Engineering at Lawrence Berkeley Laboratory. Special thanks to Anthony Moscarelli of the Bldg. 70-A Machine Shop, Lawrence Berkeley Laboratory, for his patience and invaluable instruction which made the construction of the scattering chamber both successful and enjoyable.

Finally, I would like to thank Dr. Edith Bourett and Joseph Guitron of the Electronic Materials Program, the Center for Advanced Materials, Lawrence Berkeley Laboratory for valuable assistance and an enjoyable working experience. The GaAs crystals were provided by Dr. Grant Elliot of the Opto-Electronics Division, Hewlett Packard, Inc.

This work was supported by the Director, Office of Energy Research, Office of Basic Energy Sciences, Materials Science Division of the U. S. Department of Energy under Contract DE-AC03-76F00098.

Table of Contents

I. INTRODUCTION AND BACKGROUND 1
- 1.0 Characterization Demands in Semiconductor Technology 1
  - 1.01 Semiconductor Technology 1
  - 1.02 Silicon 3
  - 1.03 Gallium Arsenide 4
  - 1.04 Gallium Arsenide Crystal Growth 8
  - 1.05 Characterization Requirements 11

II. BEAM CHARACTERIZATION METHODS 12
- 2.0 Rutherford Backscattering 12
  - 2.01 General 12
  - 2.02 Limitations of the RBS Technique 19
- 2.1 Particle Induced X-Ray Emission 22
  - 2.11 General 22
  - 2.12 X-Ray Fluorescence Process 26
  - 2.13 Sensitivity 35
    - 2.13.1 Background Radiation 35
    - 2.13.2 Absorption 42
    - 2.13.3 Sensitivity 43
  - 2.14 Semi-Empirical Approximations 50
  - 2.15 Data Analysis 56
- 2.2 Channeling 59
  - 2.21 General 59
  - 2.22 Surface Interactions 62
  - 2.23 Channeling Within the Bulk 70
    - 2.23.1 The Continuum Model 70
    - 2.23.2 Calculation of Channeling Dips 77
    - 2.23.3 Distribution of Channeled Particles 83
  - 2.24 Monitoring Channeling with X-Rays 88
  - 2.25 Lattice Location of Impurities 91
    - 2.25.1 General 91
    - 2.25.2 Determination of Specific Sublattice Site 92

III. EXPERIMENTAL 106
- 3.0 Experimental Equipment 106
  - 3.01 Scattering Chamber 106
  - 3.02 Detectors and Electronics 110

IV. RESULTS AND DISCUSSION 119
- 4.0 General 119
- 4.10 Concentration Measurements 120
- 4.20 Minimum Detectable Limit 129
- 4.30 Channeling 133
  - 4.31 Axial Scans, GaAs:In:Zn 133
  - 4.32 Sublattice Site Preference, GaAs:Si 141

V. CONCLUSIONS 160

Appendix I 164
Appendix II 170
References 177

I. INTRODUCTION AND BACKGROUND

1.0 Characterization Demands in Semiconductor Technology

1.01 Semiconductor Technology

The Technological Revolution, as did the Industrial Revolution of the 19th century, has brought dramatic changes to each industry and to every aspect of daily life. At the forefront of this phenomenon is the electronics industry which has been in particular affected by this revolution. At the heart of this activity is a group of materials known as semiconductors. Breakthroughs made since the formulation of quantum mechanics and technological advances during and after World War II in the understanding of the physics underlying the behavior of these materials has led to the creation of a new field known as Solid State Electronics. It is a fast moving field with new concepts and technology constantly being applied in a highly competative industrial environment. Future advancements depend on the availability of high quality crystals of exceptional purity as small amounts of impurities drastically alter the semiconducting properties of the material. It is the mission of the materials scientist working with engineers and scientists to supply the industry with state of the art semiconductor materials.

Semiconductors are a class of materials that posses values of resistivity and free carrier concentration in between those of metals and insulators. At very low temperatures lightly doped semiconductors become insulators while at higher temperatures they conduct quite

efficiently. This phenomenon arises from differences in the electronic band structure of the materials. Metals crystallize in close-packed structures, have high numbers of valence electrons, and are metallically bonded. The result is that electrons are loosely bound to host ions and therefore are free to move in the presence of applied electric fields. Semiconductors and insulators crystallize in the less dense diamond, or diamond-type, structures, have low numbers of valence electrons, and are covalently bonded. This leads to an energy gap between the bound and free states which electrons are able to occupy. The difference between semiconductors and insulators lies in the size of the energy gap; the energy gap in semiconductors is up to about three electron volts wide. The creation of free charge carriers in pure semiconductors results from the thermal excitation of electrons accross the energy gap into the conduction band leaving a hole behind in the valence band. Both electrons and holes are charge carriers in semiconductors. Furthermore, by careful control of the addition of impurities to the crystal and of crystal defects the conducting properties of semiconductors can be tailored so as to make possible the construction of electronic devices. It is upon the knowledge of this phenomenon that semiconductor devices and an entire industry are based.

Silicon and, to a lesser degree, germanium have been the semiconductors most used in electronic devices and will continue to be so for some time. However, speed, power, and device size requirements are approaching the practical limits of silicon. Therefore much work is being done in the development of semiconductor materials capable of supplanting silicon as the semiconductor of choice in some current

devices and most certainly in new applications. The III-V compound semiconductors have received a great deal of attention with the most promising member of this group being gallium arsenide. Gallium arsenide posesses a direct band gap structure and high electron mobility, making it useful in applications which require fast switching times with low power input. Current efforts involve growing high quality, high purity GaAs crystals. This task is complicated by the requirement that two elements be controlled during the growth process and, along with desired dopant elements, solidified into a single crystal of low defect concentration. Undesired impurities must not be present in the finished crystal. In order for the type and level of dopant and impurity elements to be ascertained characterization techniques that are fast and reliable must be employed. Rutherford Backscattering, RBS, and Particle Induced X-Ray Emission, or PIXE, are such a techniques.

1.02 Silicon

Silicon is an indirect band gap semiconductor that crystallizes in the diamond structure. It has been the most widely used and most widely studied semiconductor material and forms the basis of the semiconductor industry. Silicon crytals of large size (6" diameter, 6' lengths), low dislocation density (1 per square cm), and high purity ($N_A - N_D = \sim 10^{11}$ cm^{-3}) are readily available. Device performance has been increasing steadily as new technologies are applied.

Increasingly, however, device performance is becoming limited by

the properties of silicon itself. Technological demands require devices that operate beyond the limit of silicons' speed range, which is about 4GHz. Increases in speed through shrinking device geometries is approaching its' limit in the submicron range. Furthermore, silicon substrates are semiconducting necessitating the fabrication of isolation wells which limit circuit density and inhibit performance through the introduction of parasitic capacitance. The saturation velocity of electrons in silicon is roughly the same as for other semiconductors ($\sim 10^7$ cm/sec) but the mobility is lower. Thus, higher voltages must be applied in order for these velocities and, hence, device speeds to be realized. VLSI circuits contain over 100,000 transistors and as such require low voltages in order to minimize power dissapation and excess heat. Also, entire classes of devices such as microwave components, light emitting diodes, and optoelectronic devices are not suited for a semiconductor material with an indirect band gap structure such as silicon. Silicon also does not perform as well as other semiconductors in applications where the circuits are exposed to high levels of radiation. Therefore, further increases in device speeds and devices capable of new functions will be built from semiconductor materials other than silicon.

1.03 Gallium Arsenide

Gallium arsenide is a direct gap semiconductor that crystallizes in the zinc-blende structure. The result of such a band structure is efficient recombination of electrons in the conduction band with holes

in the valence band leading to the emission of photons. For GaAs the wavelength of the emitted light is in the near infrared making GaAs LEDs useful in optical communication and photocoupler applications. Its' unique band structure with local minima in the conduction band away from the center of the Brillouin zone, known as satellite bands, lead to properties unlike those of silicon. In the presence of electric fields in excess of 3300 V/cm, electrons begin to populate the satellite bands. The electron mobility in such bands is lower, the electron velocity decreases, and microwave oscillations are observed. This negative differential velocity gives rise to the Gunn Effect and has been applied to microwave device systems.

The basis for gallium arsenides' performance characteristics lies in the band structure. The effective mass of electrons in GaAs is about 0.068 of the free electron mass while it is about 0.97 of the free electron mass in silicon. This results in electrons with six times the mobility of electrons in silicon and therefore they approach the saturation velocity at much lower electric fields than in silicon. Furthermore, electrons in GaAs exhibit an "overshoot" in the velocity versus electric field dependence. When device dimensions are in the micron range one observes ballistic charge motion exceeding the normal saturation velocities. Typical electron saturation velocities in GaAs are about 1.4×10^7 cm/sec versus $6\text{-}7 \times 10^6$ cm/sec in silicon and velocity overshoots of 2.2×10^7 cm/sec have been observed. These velocities are reached when the applied field is about 4 kV/cm in GaAS while the maximum velocity is achieved in silicon when fields are over 10^5 V/cm. Amplifying devices fabricated from GaAs have operated at frequencies of 18 GHz with frequencies of 30 GHz projected. Clearly,

then, GaAs devices are capable of operating at frequencies far above that of silicon with far less power input. Other attractive features of GaAS are its' higher radiation hardness (10^7-10^8 rads versus 10^3-10^4 rads for silicon) and wider operating temperature range of -200 to +200 degrees centigrade. Figure 1 shows the power versus device speed characteristics for GaAs and silicon devices. The need for microwave components, radar systems, and circuits capable of processing tremendous amounts of data at extremely fast rates make the development of reliable, cost effective gallium arsenide device technology a necessity.

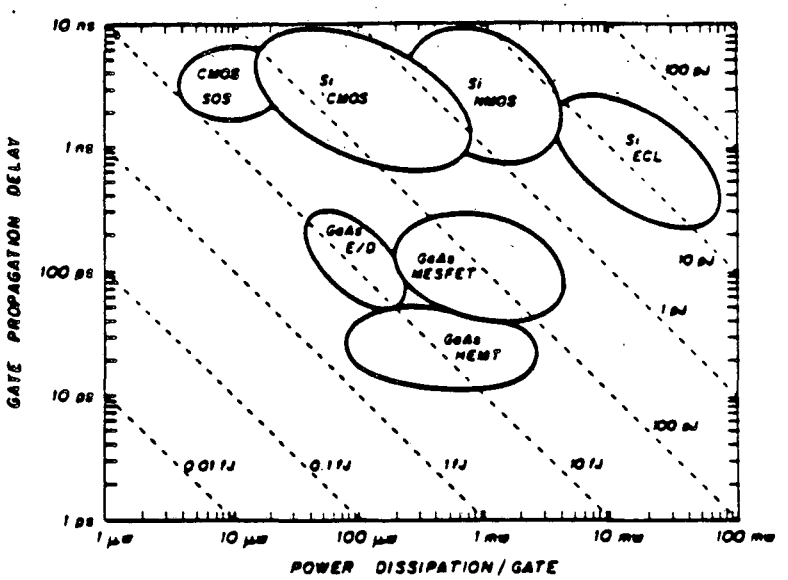

Fig. 1. Operational characteristics of silicon and GaAs digital logic circuits. (B.K. Gilbert, Symp. on Adv. Mat. Sci., GaAs Technology).

There are many technological obstacles that need to be overcome in the development of a gallium arsenide technology. Availability of high quality bulk crystals is limited as, being a compound rather than a single element, growth is far more difficult. Two elements must be brought together so as to form a crystal of proper stoichiometry with low levels of impurities and defects. In the past crystals had to be doped with chromium to compensate for contaminating elements in order to achieve seminsulating behavior. During subsequent device processing the chromium would redistribute itself in unpredictable ways causing faulty device performance and low yields. The purity of bulk GaAs crystals is $N_A - N_D = \sim 10^{15}$ cm^{-3} while for silicon it is $\sim 10^{11}$ cm^{-3}. Dislocation densities are still quite high, being on the order of several hundred to a few thousand per square centimenter. Methods employed to reduce these densities are extremely careful control of temperature gradients during the growth process and the addition of impurities in the same columns of the periodic chart as gallium and arsenic. Device processing is also made much more difficult as again the properties of two elements must be taken into consideration. There is not a stable natural oxide film that readily grows on GaAs as there is in silicon. Therefore, attempts to grow oxides on GaAs have resulted in films with high surface state densities. These surface states interfere with the homogeneous penetration of the electric field from the gate electrode into the bulk resulting in poor performance of MOS devices. Fortunately, MES devices have essentially overcome that problem.

Estimates are that GaAs technology lags behind that of silicon by ten to fifteen years, but is advancing along the same path [EK 83].

Gallium arsenide will not replace silicon in applications where the ultimate in performance is not required but only where device operating demands exceed the capability of silicon to compete. Therefore, future growth in the semiconductor industry will be based on obtaining greater understanding of both silicon and gallium arsenide.

1.04 Gallium Arsenide Crystal Growth

Common bulk GaAs crystal growth techniques include the Horizontal Bridgman and the Czochralski methods. Each approach has inherent advantages and disadvantages. The Czochralski method is the oldest and most common crystal growth method in use today. The majority of bulk crystals used in the industry today are grown by this technique. The melt is contained in a crucible of boron nitride which is slowly rotated as the crystal is pulled from the melt. Careful control of the radial thermal gradients is required in order to maintain the desired diameter. Figure 2 shows a typical Czochrolski puller. Czochralski grown crystals have the advantage of large, circular diameters and large crystal weights. Disadvantages of this method are low pull rates (< 2mm/min) and low purity (ρ < 10 ohm-cm). The thermal gradients needed to control the crystal diameter during growth contribute to dislocation formation because the gradients are responsible for large thermal stresses in the solidified crystal. The GaAs dissociation pressure at growth temperatures is about 0.9 atm causing the vaporization of the arsenic. This decomposition process is suppressed with a thick layer of boric oxide over the melt.

Improvements applied to overcome some crystal growth problems include careful control of the thermal gradients, suppression of convection through external magnetic fields, liquid encapsulation of the melt with B_2O_3 to suppress As vaporization, and isovalent doping for crystal hardening leading to lower dislocation densities. It has been shown that the addition of indium reduces the dislocation density by an order of magnitude over undoped crystals. The cause of this reduction is believed to be a combination of lattice distortion which inhibits dislocation motion and a decrease in the formation of dislocations through the condensation and interaction of point defects [TBE 86].

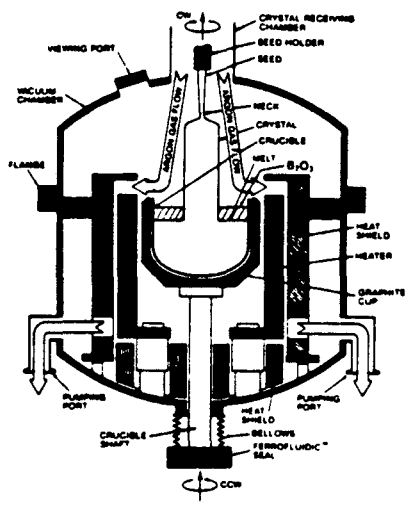

XBL 842-722

Fig. 2. Typical Czochralski puller for GaAs. (CAM Workshop for Electronic Materials, LBL).

Growth of GaAs crystals by the Horizontal Bridgman method takes place inside a sealed ampoule. The crystal is solidified from the melt contained in either a quartz or pyrolitic boron nitride boat (Fig. 3). The GaAs melt is synthesized from liquid gallium which is held at a temperature above the melting point of GaAs with the As source (in the far end of the ampoule) held at a temperature of about 600° C. This provides approximately a 1 atm pressure of As vapor over the melt. The elements react inside the quartz boat forming liquid GaAs. The crystal is solidified starting at the seed end by a controlled thermal gradient set up along the length of the boat. The reduction of the silica boat incorporates silicon into the crystal. The silicon impurities tend to occupy gallium sites in the lattice and thus "donate" the fourth valence electron to the conduction band resulting in n-type material. Chromium, a deep acceptor in GaAs, is added to compensate the shallow donor silicon.

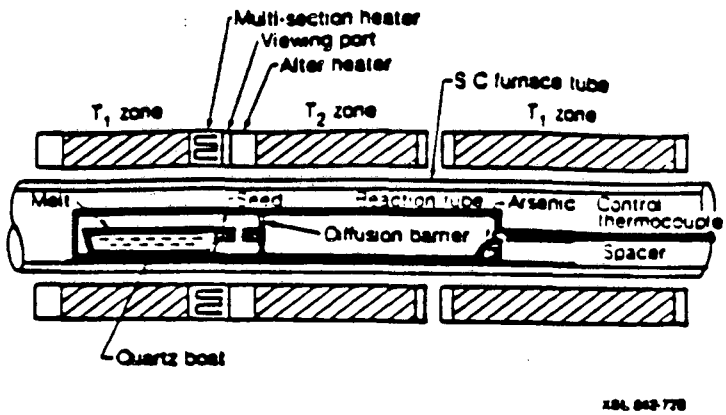

Fig. 3. Schematic of Horizontal Bridgman crystal growth furnace for GaAs. (CAM Workshop for Electronic Materials, LBL).

The major advantages of the Horizontal Bridgman method are that with low thermal stresses the dislocation density is much lower and, by nature of the method, the stoichiometry can be controlled by varying the arsenic overpressure. This ability to adjust the stiochiometry has important advantages in the growth of undoped semi-insulating material. Crystals grown under As-rich conditions have shown this behavior. It is thought that the presence of the EL2 defect, assumed to responsible for semi-insulating properties, is related to As anti-site defects. This, in effect, eliminates the need to dope a crystal with Cr and, in turn, eliminates the associated device processing problems. Horizontal Bridgman grown crystals, however, are of non-cylindrical shape and as such do not lend themselves well to wafer processing. The problem of silicon incorporation can be overcome by using a boat of pyrolytic boron nitride. To achieve cylindrical Bridgman crystals the Vertical Bridgman technique must be employed.

1.05 Characterization Requirements

In order to successfully grow GaAs crystals characterization techniques that are capable of identifying undesired impurities and the desired dopant species and concentration are necessary. Furthermore, the techniques employed must have the ability to measure variations in concentration across the radius and along the length of the crystal. Knowledge of the unwanted impurity species may lead to the indentification of the source and as such is vital to the production of high purity crystals. As the concentration of dopants

is increased the strain imposed upon the lattice increases such that a higher concentration of defects may be observed. One would also like to evaluate the increase in crystal defects with increase in dopant concentration. Also, since desired impurities may not become electrically active unless they are substitutional or induce charge compensating defects if they are interstitial it is important to be able to verify their lattice position. Finally, in the case of compounds such as GaAs, the specific sublattice site occupied by a particular dopant is of great importance in determining the electrical properties of the crystal. Invaluable to a crystal growth program is a technique which will provide verification of the impurities responsible for the observed behavior.

The purpose of this study was to evaluate applicability of the combined Particle Induced X-ray Emission and Rutherford Backscattering techniques to the measurement of concentration, lattice position, and sublattice site of dopants and to determine the minimum detectable limit of impurities in bulk GaAs crystals.

II. BEAM CHARACTERIZATION METHODS

2.0 Rutherford Backscattering

2.01 General

The Rutherford Backscattering (RBS) technique involves directing a collimated beam of energetic charged particles at a target and

measuring the energy of the backscattered projectiles. The analyzing particles undergo a series of collisions with the atoms of the solid, gradually losing energy via small angle scattering with the electron clouds of the target atoms until the projectile comes to rest. A small fraction of the incoming particles experience large angle scattering from coulomb interaction between the energetic ion and the nucleus of a target atom and hence are backscattered. The backscattered particles are detected by a solid state surface barrier detector which produces signals which are proportional to their energy. The energy is in turn proportional to the mass of the projectile ions and of the target atoms. Thus, within certain limitations, the mass of the elememts that are in the target can be determined. Figure 4 shows a schematic of the RBS process.

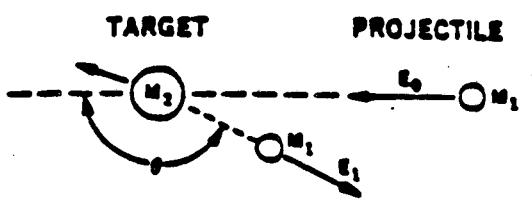

$$K \equiv E_1/E_0$$

$$K(\theta=180^\circ) = \left[\frac{1 - M_1/M_2}{1 + M_1/M_2}\right]^2$$

Fig. 4. Schematic of inelastic collision between projectile ion and target atom that is the basis of the RBS technique. (Courtesy KMY 84).

Analysis of a RBS spectrum requires knowledge of the probability that an incident ion will be backscattered which is described by the scattering cross section, of the relationship between the incident and backscattered energy of the ion which is given by the Kinematic factor, and of the energy loss of the projectile as it penetrates the target, described by the stopping power of the matrix. These quantities are defined in the following discussion.

A projectile that undergoes nuclear scattering has penetrated through the electron cloud such that there is an interaction potential, V_{inter}, between the projectile ion and the nucleus of the target atom:

$$V_{inter} = \frac{zZe^2}{r} \text{ eV}, \tag{1}$$

with z and Z being the atomic number of the projectile and the target atom, respectively, r is in Å, and e^2 is equal to 14.4 eV-Å. Here r represents the distance of closest approach of the projectile and is characterized by the impact parameter, b, as shown in Figure 5. The impact parameter and the scattering angle are related by [FMP 82]:

$$2mv\sin(\phi/2) = \frac{zZe^2}{vb} 2\cos(\phi/2), \tag{2}$$

to give the differential scattering cross section:

$$\frac{d\sigma(\phi)}{d\Omega} = (zZe^2/4E)^2 \frac{1}{\sin^4(\phi/2)} \quad , \tag{3}$$

which is the well known Rutherford scattering cross section. Here v, E, and m are the projectile velocity, energy, and mass, respectively.

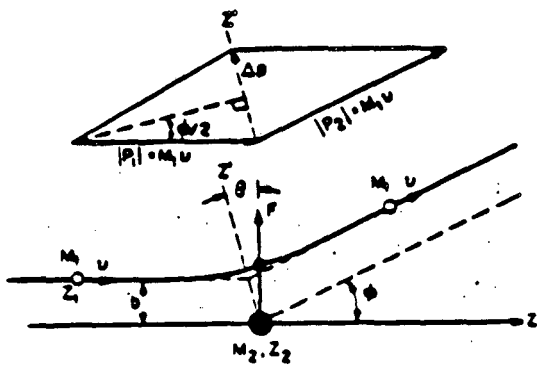

Fig. 5. Momentum diagram and geometry for Rutherford scattering. The magnitude of the momentum change is related to the scattering angle via Eq. 2. (FMP 82).

Ions incident on the target that experience backscattering from the surface are so with an energy less than the initial ion energy:

$$E_{BS} = K_M E_0 \quad , \tag{4}$$

where E_{BS} is the backscattered ion energy, E_0 is the initial ion energy, and K_M is tne Kinematic Factor which relates the energies and is given by:

$$K_M = \frac{((M^2+m^2\sin^2\theta)^{0.5}+m\cos\theta)^2}{(M+m)^2}, \qquad (5)$$

where M is the target mass, m is the projectile mass, and θ is the backscattering angle as defined by Figure 4. Thus, by comparing E_0 to E_{BS} it is possible, using standard tables, to identify the elements of and within a matrix.

As projectiles penetrate the target they lose energy and, likewise, as they traverse the matrix after being backscattered they also lose energy. This energy loss must be accounted for when analyzing a RBS spectrum and is so by applying the stopping power of the matrix to the projectile. The stopping power is an effect of the ion - electron collisions and is well described by Linhards' modification to the Bethe-Bloch formula [LJ 65]:

$$\frac{dE}{dx}(r) = \frac{4\pi z^2 e^4}{mv^2} \quad L_e[(1-\alpha)NZ + \alpha\epsilon(r)], \qquad (6)$$

with $\epsilon(r)$ being the density of electrons at the point (r) through which the particle moves, N is the number of atoms per unit volume, m is the electron mass, v is the ion velocity, and α=~1/2. L_e is given by [FMP 82]:

$$L_e = \frac{2mv^2}{I}, \qquad (7)$$

with I=~10Z in eV and is called the average excitation potential. These equations show that equalivalent amounts of energy are lost in

particle-electron collisions through distant resonant collisions with small momentum transfer and close collisions with large momentum transfer. For compounds the stopping cross sections are additive [BK 05]:

$$\epsilon^{A_mB_n} = m\epsilon^A + n\epsilon^B \tag{8}$$

with $\epsilon^{A_mB_n}$ equal to the stopping cross section of molecule A_mB_n, m and n are the atomic fractions of atoms A and B, and ϵ^A and ϵ^B are the stopping cross sections of atoms A and B of the compound. Thus the energy loss of the projectile becomes:

$$\left(\frac{dE}{dx}\right)^{A_mB_n} = N^{A_mB_n}\,\epsilon^{A_mB_n} \tag{9}$$

where $N^{A_mB_n}$ is the density of the molecule A_mB_n in the solid.

A typical RBS spectrum is shown in Figure 6 for a thin film M_2' on a substrate M_2 with $M_2' > M_2$. The backscattering off of the surface of M_2' and off of M_2 is apparent. The energy of the backscattered particle from the surface of M_2' is E_o multiplied by the Kinematic factor for M_2'. The width of the M_2' film signal is caused by energy loss of the projectile travelling through the film in both the inward and outward directions. Knowledge of the stopping power allows the measurement of the film thickness. The surface edge of M_2 is displaced to the lower energy direction (3 as opposed to 3') as the energy of the projectiles backscattering off of M_2 is less than E_o of the ion since it traveled through the film M_2'. The continuum to the left of the substrate edge is a result of

backscattering from within the substrate (4) and is, again, caused by energy loss of the projectiles.

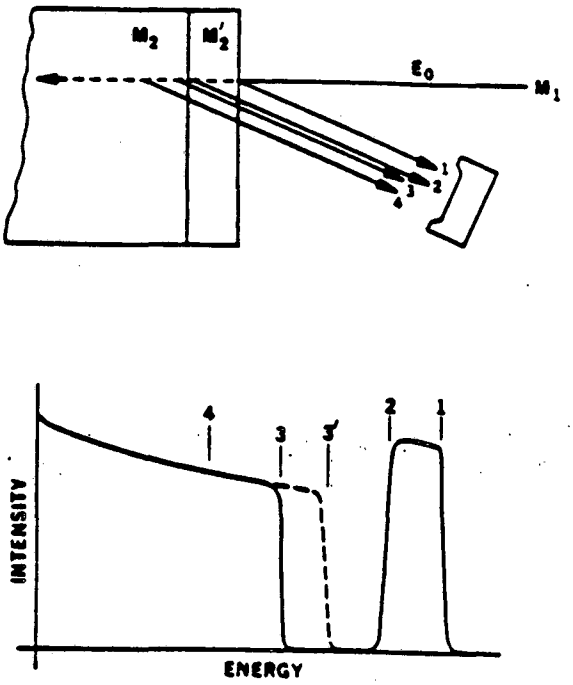

Fig. 6. a)Schematic of backscattering of thin film, mass M_2', on substrate M_2 w/ $M_2' > M_2$.
b) The corresponding energy spectrum. 3' represents the backscattering energy of M_2 w/o the film. (Courtesy KMY 84).

Note that heavier target atoms produce higher energy backscattered ions and show up in the spectrum to the right of lighter elements. Therefore, if an element is lighter than the matrix its' signal will appear on top of the matrix signal. Similarly, elements of similar mass backscatter ions with similar energies and therefore their surface signals will be close together in the spectrum. This leads to important limitations of the RBS technique. Table I summarizes the RBS capabilities.

TABLE I

SUMMARY OF BACKSCATTERING CAPABILITIES

Mass perception	1 amu up to 40 amu 10 amu for heavy elements	
Depth perception	Range	< 1 μm
	Resolution	~ 200 Å
	Accuracy	~ 5
	No external standards required	
Composition Analysis	Atomic ratios or atoms per unit area	
	Accuracy	~ 5% or better
	No external standards required	
Sensitivity	Heavy elements in light matrix	$\geq 10^{18}$ cm^{-2}
	Light elements in heavy matrix	$\geq 10^{-1}$
	Similar masses	poor
	Point defect	$\geq$ 5E20 cm^{-3}
	Line defect	$\geq$ 10 cm/cm^2
Crystal structure	Lattice location Epitaxy	

2.02 Limitations of the RBS Technique

As mentioned, analysis of an RBS spectrum becomes difficult when the foreign and host atom are of similar mass or worse when the foreign atom is lighter than the host atom. The Kinematic factor, as given in Eq. 5, depends in part on the mass of the projectile ion and the target atoms. Mass resolution is good when light projectiles are incident upon targets with an atomic number less than about 30. However, heavier target atoms of similar mass will backscatter the projectiles with similar energies, leading to poor mass resolution. Note, however, that by greatly increasing the mass of the projectile

the difference in K_M between two adjacent elements on the Periodic Table increases. Therefore, for targets of Z > ~30, use of heavy ion projectiles (Heavy Ion RBS, HIRBS) significantly increases mass resolution. This increase in the difference between K_M is shown in Fig. 7 where the change in K_M is plotted against atomic number. The steeper slope for $^{16}O^+$ ions, for example, than for $^4He^+$ incident on targets of Z > ~30 is apparent. Figure 8 shows the increase in mass resolution obtained when bombarding GaAs with $^{16}O^+$ ions rather than $^4He^+$ ions. HIRBS is not suited to analyzing elements within a matrix that are lighter than the projectile ions [KMY 84].

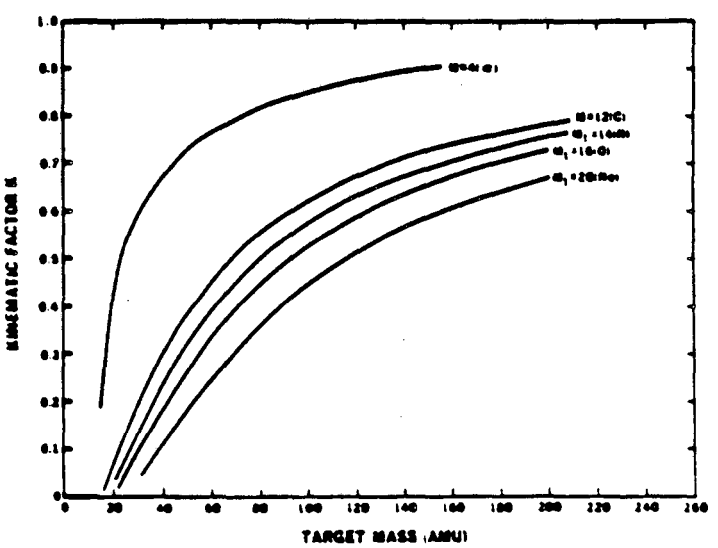

Fig. 7. Kinematic factor, K, for various projectiles plotted vs. target atomic number. (Courtesy KMY 84).

Unfortunately, the case where the foreign atom is lighter than the host atom cannot be overcome by choice of projectile. The signal from

the lighter element is superimposed on the continuum signal of the matrix, as demonstrated by Cr on GaAs in Figure 8, leading to poor detectibility limits. Figure 9 shows a spectrum taken from silicon doped GaAs. Note that no silicon is visible. To overcome this deficiency a technique that does not rely on the differences in mass between elements to obtain information must be employed. Particle Induced X-Ray Emission, which makes use of the characteristic x-rays generated by projectile-target atom collisions, is such a technique.

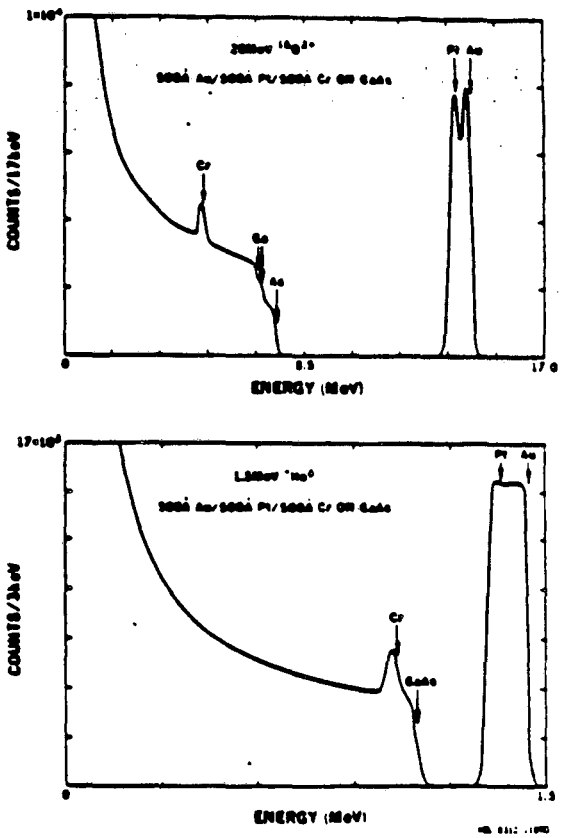

Fig. 8. Backscattering spectra comparing $^{16}O^{+}$ and $^{4}He^{+}$ ions for a layered structure. Shows increase in mass resolution for heavy ions. (Courtesy KMY 84).

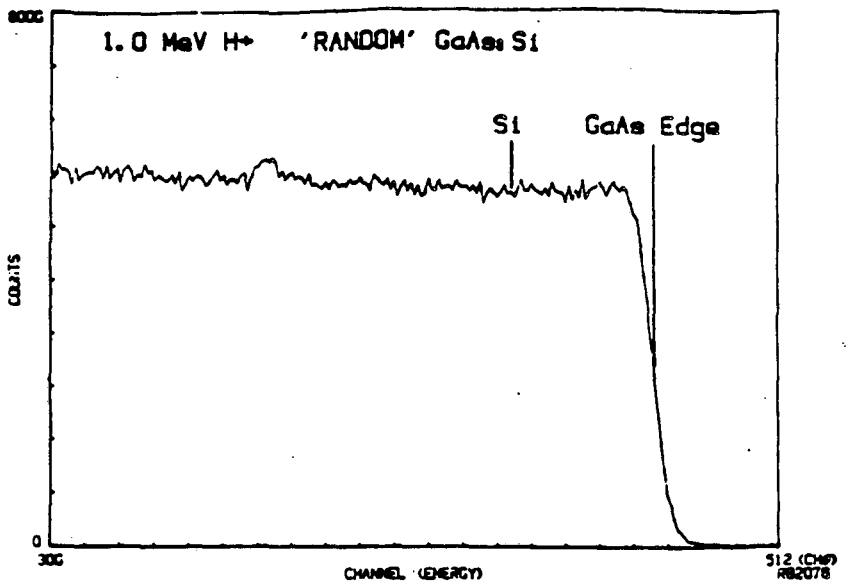

Fig. 9. Backscattering spectrum of 1.0 MeV protons on Si doped GaAs showing a limitation of the RBS technique when the impurity mass is less than that of the matrix. Note no Si peak is visible.

2.1 Particle Induced X-Ray Emission

2.11 General

Particle Induced X-Ray Emission (PIXE) is a characterization technique in which the characteristic x-rays of a sample are produced, sorted, and analyzed to determine the species and concentration of the elements present within a sample. In a manner similar to the RBS technique, the sample is bombarded with energetic charged particles which results in the creation of vacancies in the inner shells of the target atoms. The atom is in an excited state, is energetically unstable, and returns to a stable configuration by filling the inner shell vacancy with an electron from an outer shell. This process

results in the atom emitting x-rays (radiative process) or auger electrons (non-radiative process). Each shell transition for each element posesses a unique x-ray signature which is used to determine the composition of the sample. The x-rays are detected (in most PIXE studies) by a solid state semiconductor detector. The resulting signal is amplified and sent to a multi-channel analyzer. Raw data are then transferred to a computer for more sophisticated operations which allow the concentrations of elements within the sample to be determined.

The yield of x-rays emitted from element i in a thick sample is given by the equation:

$$N_i = I_o \rho_i \frac{\Omega}{4\pi} \epsilon_i \prod_{j=1}^{n} a_{j_i} \omega_i \int_0^{\mathcal{R}} \sigma_i(E(x)) e^{-\alpha x} dx \ , \qquad (10)$$

where N_i is the total number of counts of a particular x-ray from element i, I_o is the total number of protons incident upon the target, ρ_i is the density of element i in atoms - cm^{-3}, $\Omega/4\pi$ is the solid angle subtended by the detector, ϵ_i is the detector efficiency for element i, the product of the a_j accounts for absorption of x-rays from element i from Be windows, air gaps, filters, etc., ω_i is the fluorescent yield of a particular transition in element i, and the integral gives the change in ionization cross section with projectile energy (nence depth) and the absorption of the x-ray by the sample over the dpeth of the range of the particle. Since all terms in the equation can be measured or otherwise determined, the concentration of an element within a matrix can be found. For the case of thin samples the integral reduces to a

constant with negligible absorption. Purely analytic solution to the integral for thick samples (here, a 'thick' sample is one in which the ionization cross section varies appreciable with depth and absorption by the sample is not negligible, ie., the range of the projectile in the sample is less than the sample thickness). Therefore, several researchers have applied various numerical or semi-empirical methods as approximations for the integral [GGK 81], [RW 81], [SM 83], [WR 77].

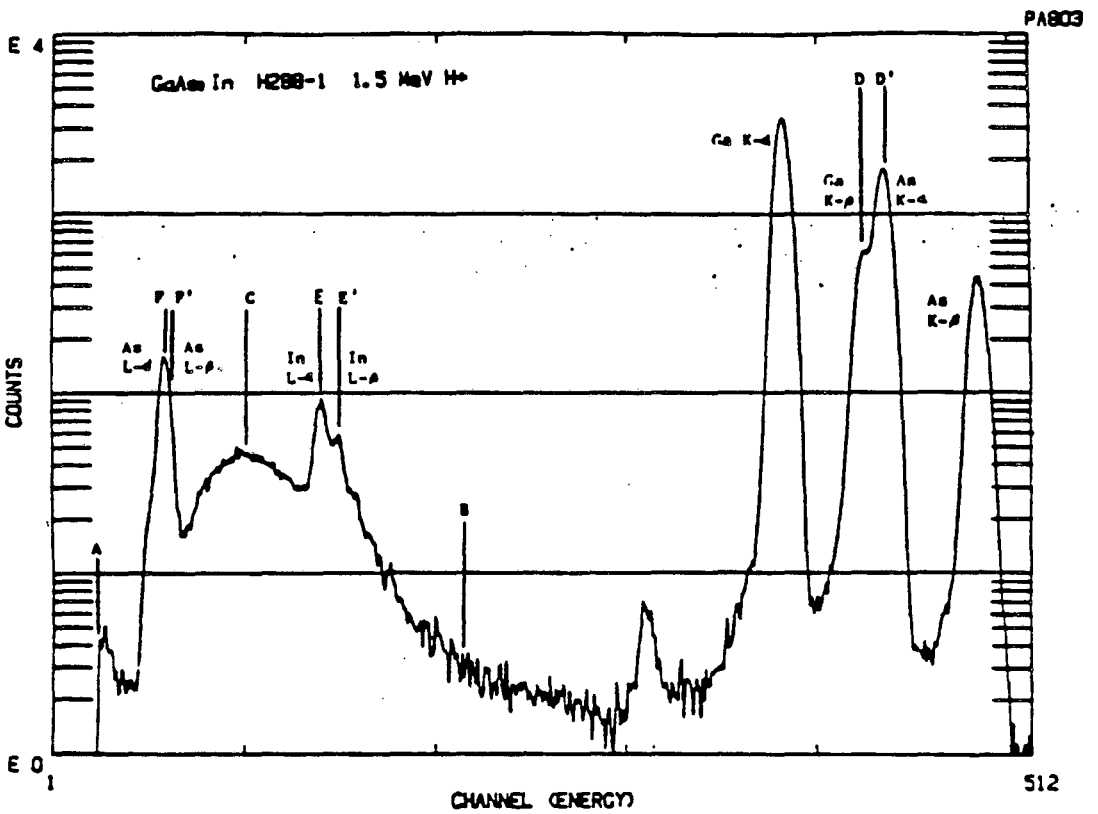

Fig. 10. PIXE spectrum for 1.5 MeV protons on GaAs:In showing the distribution of x-ray peaks.

A typical PIXE spectrum is shown in Figure 10. X-Ray energy increases left to right. The spectrum consists of localized regions of peak counts corresponding to x-ray emission from target elements

superimposed on a continuous background spectrum. Point 'A' marks the minimum x-ray energy detectable by the system. The x-ray energy at this point in this spectrum is ~0.440 eV. Therefore, the system is capable of detecting x-rays from impurities as light as oxygen. Channels to the left of 'A' correspond to x-ray energies that are completely attenuated by chamber and detector windows, air gaps, etc., and as such are not observable. The continuous background spectrum to the left of point 'B' is caused by addition of radiation produced by both projectile and secondary electron bremsstrahlung while to the right of 'B' it is caused by projectile bremsstrahlung only. The decrease in the yield of the spectrum to the left of point 'C' is a result of partial, yet significant, absorption of x-rays of those energies by the sample, windows, etc. Note that most inner shell transitions in a particular element result in both α and β transition emissions. These peaks can be resolved, as shown by points 'E' and 'E'' or, as in the case of points 'D' and 'D'', overlap making separation and fitting more difficult. Depending on the relative transition probabilities and energies involved, the peaks may completely overlap making separation extremely difficult (points 'F' and 'F''). Obviously, each spectrum must be treated on a case by case basis and its' particular shape depends on the elements within the matrix. Of major concern in PIXE analysis is the intensity of the background spectrum as this will ultimately dictate the minimum detectable limit of trace elements within a matrix.

2.12 X-Ray Fluorescence Process

The production of characteristic x-rays of an element by PIXE depends on close-encounter probability events taking place between energetic charged particles and inner shell electrons in which the atomic states are perturbed. This results of this interaction can be understood in terms of the Bohr theory of the atom with elaborations provided by subsequent researchers [DN 73]. A well known component of the Bohr theory is that electrons in atoms are grouped into successive shells about the nucleus with a binding energy that decreases with distance (Fig. 11).

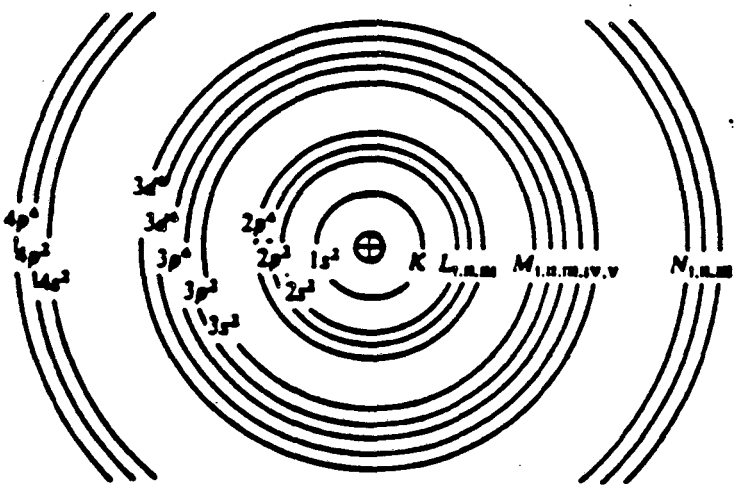

Fig. 11. The shells and subshells of the Bohr atom. (DN 73).

When an ionizing collision takes place between the projectile and a bound electron (ie., the electron is excited from a bound to a continuum state) a vacancy is created in the shell from which the

electron was removed and the atom is energetically unstable. The vacancy is filled by an electron from an outer shell which may result in the emission of the energy gained by the transition in the form of a characteristic x-ray photon (Fig. 12).

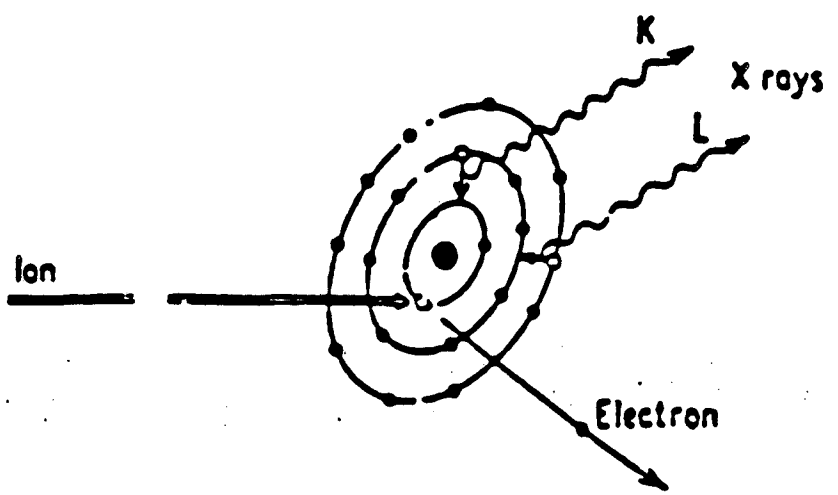

Fig. 12. Ion-electron collision resulting in emission of a characteristic x-ray which forms the basis of the PIXE technique. (FF 74).

Electronic shell transitions are governed by selection rules which are determined by quantum mechanical consideration of the four quantum numbers, n, l, s, j, of the electrons in the atom .

$$\Delta l = \pm 1; \quad \Delta j = -1, 0, 1 , \tag{11}$$

where l is the orbital angular momentum quantum number and j is the total angular momentum number and is equal to $l \pm s$. Δn, the principal quantum number, may take on any value [DN 73]. Figure 13 depicts the transitions between atomic levels for a large atom. Most often used

in PIXE studies are the $K_{\alpha-1}$ and $L_{\alpha-1}$ x-rays as they, being the most probable transitions, are of convenient intensity and energy.

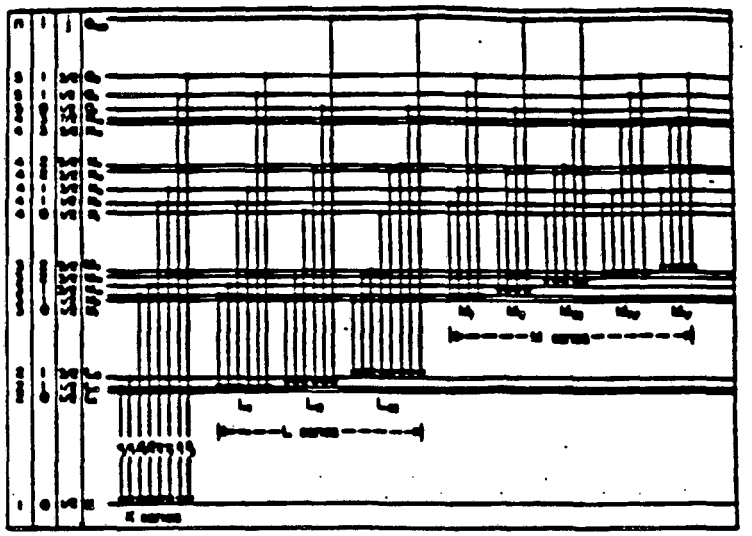

Fig. 13. Energy level diagram and possible electron transitions. (VV73).

The probability of an ionizing collision taking place can be understood within the framework of standard theoretical models. There are three models which have been developed: the Born Plane Wave Approximation (Merzbacher and Lewis, 1958), the Impact Parameter Method (Bang and Hansteen, 1959), and the Binary Encounter Approximation (Garcia, et al, 1973). Although all three models treat the ionizing collision as a coulomb interaction between the incident particle and the electron in a shell of the target atom, there are differences in both details and approach between the models.

The Born Plane Wave Approximation (BPWA) describes the initial and inelastically scattered particle as plane waves. The ionizing event is described by a weak perturbation resulting from a coulomb

interaction between the incident particle and a bound electron. The initial and final states of the atom are therefore described by a transition from the bound state of the electron to one of a continuum wave function with the states of all other electrons remaining unchanged. Transitions from bound states of the electron to unoccupied orbitals are negligible [ML 58], [GJ 73]. Therefore, the expression for the cross section is written as a differential form in terms of the momentum transferred, $\hbar\cdot\vec{q}$, for ionization into a given final state, [JG 73, p. 112]. The total cross section is obtained by integrating this expression over all allowable kinetic energies and directions of ejected electrons (ie., over all momentum transfers compatible with the production of a final state and summed over all possible final states). Further approximations include the addition of parameters which allow for the initial states to be described by hydrogenic wave functions with effective charge Z_s. The parameters are:

$$\Theta_s = n_s^2 u_s / Z_s^2, \qquad \eta = Z_s^{-2}(hv/e^2)^2 , \tag{12}$$

where n_s is the principal quantum number and u_s the binding energy (atomic units) of the sth shell. Thus Θ_s is proportional to the ratio of the true binding energy to that predicted by a hydrogenic wave function ($\varepsilon = Z^2/2n^2$ for the sth shell) and η_s is proportional to the ratio of the incident projectile energy to ε. By using these parameters the expression for the total cross section can then be conveniently written as:

$$\sigma_s = (8\pi z^2 a_0^2 / Z_s^4 n_s) f_s(\theta_s, \eta_s) \ , \tag{13}$$

with a_0 being the Bohr radius and f_s the result of the integration of the initial expression for the momentum transfer for ionization into a particular final state. The significance of the parameters θ_s and η_s is that it allows for the Z and n dependence of the ionization cross section to be understood in a straightforward manner; scaling between different shells and atoms is greatly simplified.

The BPWA model in this form suffers from the limitation that it is only valid for energies of incident particles greater than the binding energy of the electron in a shell. It can not account for adiabatic adjustment of the electron to the presence of an incident particle which energy is on the order of the binding energy of the electron. When the incident particle energy is as such, the electron can adjust to the particle's presence adiabatically without being removed from the shell thus causing a vacancy [JG 73]. The result is an ionization probability at lower incident energies that is different than the probability predicted by the model. The valid range of the BPWA model is then given by [MM 65]:

$$zZe^2/hv \ll 1 \ , \tag{14}$$

where z and Z are the charge of the projectile and the target, respectively, and v is the relative velocity. This indicates that, for proton vacancy production in K shells of moderate size atoms, that

the proton energy divided by the K shell binding energy must be greater than 24($E_p/u_K > 24$) in order for the model to correctly predict the observed results. This situation inspired Bang and Hansteen to modify this model by introducing impact parameters to the particle trajectories.

The Impact Parameter Method by Bang and Hansteen builds upon the BPWA model. Particle deflections resulting from nuclear scattering are taken into account which extends the valid energy range of the BPWA model. Also considered is the decrease in the kinetic energy of the projectile which becomes important when its' energy approaches that of the binding energy of the electron. However, this does not describe adiabatic adjustment by the electron; it more accurately represents the energy of the ionizing particle as it passes through the target. Without the particle deflection corrections this model is the same as the BPWA model [JJ 76], [JG 73].

The Binary Encounter Approximation [JG 73] assumes a different approach to the problem and because of the ease with which scaling is accomplished and its' valid energy range, it is the model which most PIXE experimentalists use today. The electrons in respective shells are treated as <u>free</u> particles (not bound as in the BPWA) with a velocity associated with the momentum of the bound state in which they actually are. The ionizing collision is treated as a direct energy exchange between the incident particle and the electron. (Note that the BPWA model assumed a weak perturbation description between the incident particle and a bound electron). Therefore, the collision takes place between an incident particle, momentum $\vec{k}_1$, and a free electron, momentum $\vec{k}_2$. The expression for the cross section is

summed over all momentum exchanges between the incident particle and the electron compatible with an energy exchange between the two. This sum is then integrated over all allowed energy exchanges which, by nature of the model, is weighted by the distribution of electron momentum associated with the bound states.

The BEA model is based on the fact that the exact quantum mechanical expression for the cross section for the collision of two free charged particles is identical to the classical result [JG 73]. Therefore, with the exception of the determination of the distribution of the initial bound electron momenta, all steps of the collision can be carried out classically. Therefore the expression for the ionization cross section becomes [JG 73]:

$$\sigma_I(v_1) = N_i \int \sigma_i(v_1, v_2) f(v_2)\, dv_2 \,, \tag{15}$$

with:

$$\sigma_i = \int \frac{d\sigma}{d\Delta E}\, d\Delta E \,, \tag{16}$$

with $\sigma_I(v_1)$ the ionization cross section resulting from collision by a particle with velocity v_1, N_i is the number of equivalent electrons with binding energy u, and $f(v_2)$ is the momentum (speed) distribution of the bound electrons. The integration of Eq. 16 can be carried out in closed form (JG 73, p. 114).

A useful and interesting result of this approach is that the cross section obeys a scaling law which depends only on the charge and energy of the incident projectile and on the binding energy of the

electron in a shell of a particular element. Application of hydrogenic wave functions to Eq. 15 leads to :

$$u^2\sigma_I = z_1^2 f[E_1/\lambda u, \lambda] , \tag{17}$$

where z_1 and λ are the charge and mass (electron mass units) of the projectile and u is the binding energy of the electron. Thus universal plots can be obtained ie., a plot of $u^2\sigma_I/(z_1)^2$ versus $E_1/\lambda u$ will give the same result for all target atoms.

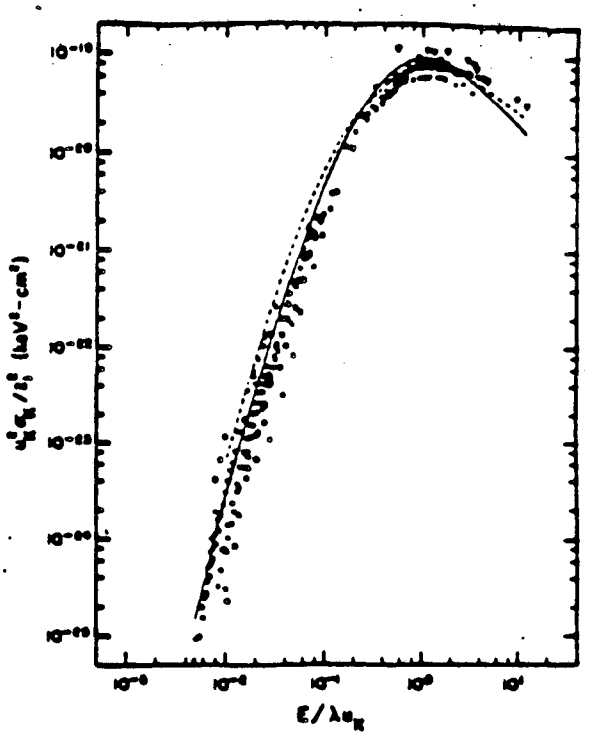

Fig. 14. Universal plot (BEA coordinates) of K-shell ionization cross sections. Solid curve is BEA, dotted curve is BPWA, dots are experimental measurements. Note improved agreement of BEA w/ experiment at lower projectile energies. (GJ 73).

Cross sections for specific projectile energy and species/element combinations can be obtained from the plot by substituting the appropriate values into the expressions on the ordinate and abcsissa of the plot. Herein lies the value of the BEA model. Figure 14 compares the results of the BPWA and the BEA models to experimental results. Note the improved agreement of the BEA with experiment over the agreement between the BPWA and experiment in the lower energy region of the curve. This corresponds to projectile energies (500-1000 keV) and binding energies (1.5-10 keV) most used in PIXE studies of semiconductors and as such is more accurate than the other approximations.

As mentioned previously, not all vacancies created result in the production of characteristic x-rays. The atom may adjust to a stable configuration by either emission of a photon or by emission of auger electrons. The probability that the filling of the vacancy will be accompanied by an emission of x-rays is described by a parameter known as the fluorescent yield, ω. It is defined as [DN 73]:

$$\omega_i = \frac{X_i}{(X_i + A_i)}, \tag{18}$$

where ω_i is the fluorescent yield for the ith transition, X_i and A_i are the x-ray and auger yields for the transition, respectively. Auger transition probabilities are almost independent of atomic number, while flourescent yields are approximately proportional to Z^4 [DN 73]. Bambynek, et al, [BW 72] has determined the fluorescent yield of the various shell transitions for the elements. Therefore, the x-ray production cross section is related to the ionization cross

sections by this parameter:

$$\sigma_p = \omega\sigma_i \ , \tag{19}$$

2.13 Sensitivity

Of concern with any analytical measurement technique is the limit of concentration of trace elements that can be detected. Sensitivity of the PIXE technique is limited by the intensity of background radiation resulting from various processes and by the characteristics of the particular detector and associated instrumentation.

2.13.1 Background Radiation

Background radiation ultimately determines the sensitivity of the PIXE technique, regardless of the type of detector used for measuring the x-rays. However, by understanding the processes which lead to this effect its' importance can be diminished through proper control of experimental parameters. There are three sources of background radiation: 1) secondary electron bremsstrahlung, 2) projectile bremsstrahlung, and 3) high energy gamma ray radiation. The effect of each of these can be reduced by control of projectile species and energy.

Secondary electron bremsstrahlung (Fig. 15a) is the most important type of background radiation and becomes a problem when characteristic x-ray energies lie below the maximum energy transferred to an electron by the projectile. Inherent in the PIXE process is the removal of

electrons from bound states into an energy continuum. Once in this continuum state the electron is free to undergo changes in trajectory as it traverses interatomic space via deflections caused by the electric field of the matrix atoms.

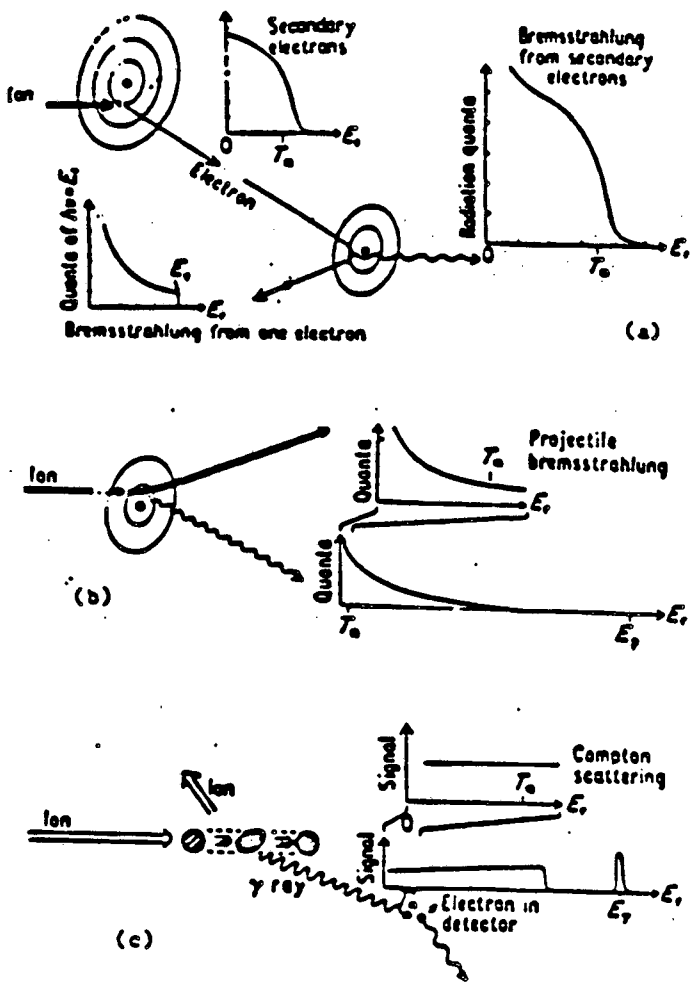

Fig. 15. Schematic of background radiation production processes and the associated spectra. a) secondary electron bremsstrahlung, b) projectile bremsstrahlung, c) high energy gamma ray. (FF 74).

Furthermore, the electrons will experience decceleration as they suffer direct collisions with other atoms in the solid. Thus, secondary electron bremsstrahlung is a two step process which results in the emission of a continuum of radiation. The first process results in the emission of radiation ranging in energy from that of the electrons and below while radiation from the second process is below that of the (initial) maximum energy of the freed electron.

The maximum energy that an an electron may radiate is related to the maximum energy that the electron is able to aquire from the ionizing collision with the projectile by [FF 74]:

$$E_{max} = \frac{4mE_p}{M} , \tag{20}$$

where m is the electron mass, M is the projectile mass, and Ep is the projectile energy. Following the treatment given by Folkmann, et al. [FF 74, p. 490], the probability that an electron ejected with kinetic energy E_δ will produce a bremsstrahlung photon of energy between E_r and E_r+dE_r (assuming the electron remains in the sample) is given by:

$$dY(E_\delta, E_r) = \int_{E_r}^{E_\delta} d\sigma_r(E_e,E_r)\frac{dE_e}{S_M(E_e)A_M M} , \tag{21}$$

with $d\sigma_r/dE_r(E_e,E_r)$ the bremsstrahlung cross section for an electron of energy E_e and S_M the stopping power of the matrix of atoms of atomic number A_M. This expression reflects the two step nature of the process as the bremsstrahlung cross section accounts for

the deflections of the electron while the quotient describes the decceleration via collisions. Combining this expression with the expression for the cross section for the production of secondary electrons gives the effective cross section for the production of secondary electron bremsstrahlung:

$$d\sigma^{b}(E_r) = \int_{E_r}^{\infty} dY(E_\delta, E_r) \frac{d\sigma_e}{dE_e}(E_\delta) dE_\delta, \tag{22}$$

where $d\sigma_e/dE_e(E_e)$ is the cross section for the production of secondary electrons and can be calculated by either the BPWA or the BEA method. Calculation of this cross section predicts a rapid decrease in the intensity of bremsstrahlung for electron energies greater than E_{max} (Fig. 16).

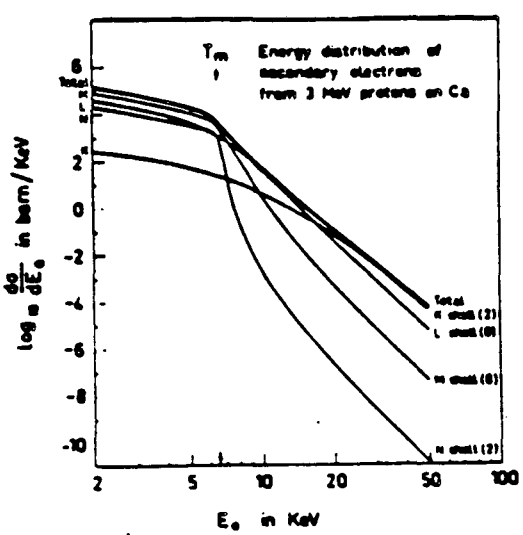

Fig. 16. BEA calculation of the energy distribution of electrons ejected from impact with protons. T_m is the maximum energy transferred to the electron in the collision. $T_m = E_{max}$ of Eq. 2. (FF 74).

An important result [FF 74] is that the secondary electron cross section scales with the projectile parameters z (atomic number), a (mass), and E (energy) as given by:

$$\frac{d\sigma_e(za,E_p)}{dE_e}(E_e) = z^2 \frac{d\sigma_e(\text{proton}, E/a)}{dE_e}, \qquad (23)$$

Therefore, within certain limits, by reducing projectile energy the intensity of and region of the spectrum in which this is the dominate background can be reduced. Use of projectiles of lower mass does not, however, result in diminished contribution to the background as both x-ray production and secondary bremsstrahlung cross sections scale as z^2. Hence, the ratio between the yields of the two processes does not depend on projectile mass. Therefore, for light elements (x-ray energy less than E_{max}) all projectiles will give the same sensitivity. X-rays from heavier elements (x-ray energy > E_{max}) do not experience background from secondary electron bremsstrahlung and as such the sensitivity can be optimized through choice of projectile.

Incident projectile bremsstrahlung (Fig. 15b) is similar to secondary electron bremsstrahlung insofar as it is a result of the deceleration of charged particles. The projectile, as do knock-on electrons, experiences deceleration as it passes through the sample. Again, radiation is emitted. The intensity of this radiation, however, is fairly constant over the entire energy range of the spectrum as compared to that of secondary electron bremsstrahlung. The cross section for projectile bremsstrahlung is given by:

$$\frac{d\sigma}{dE} = \frac{Cz^2Z^2}{EE_e}\left(\frac{z}{a} - \frac{Z}{A}\right)^2, \tag{24}$$

where C is a slowly varying factor [FF 74], E is the projectile energy, E_e is the secondary electron energy, and Z, A, z, a are the charge and mass of the target atoms and projectile ions, respectively. This equation indicates that by increasing projectile energy and/or increasing the charge to mass ratio of the projectile the contribution to the background radiation spectrum from projectile bremsstrahlung can be reduced to zero. Increasing projectile energy would worsen the effect of secondary electron bremsstrahlung as described previously and the use of heavy ions results in higher sample temperatures and increased background from gamma ray emission. Furthermore, reduction of secondary electron bremsstrahlung via lowering of the projectile energy is counterbalanced by an increase in projectile bremsstrahlung. Figure 17 shows the contribution to background from secondary electron and projectile bremsstrahlung. Since the electron bremsstrahlung is dominant, projectile energy can be adjusted so that the sum of the radiation from the two sources is a minimum. Figure 10 shows the combination of secondary electron and projectile bremsstrsahlung in a typical PIXE spectrum. Therefore, lower projectile energies (within the limits of practical x-ray yields) and low mass projectiles such as protons are the prefered choice for PIXE.

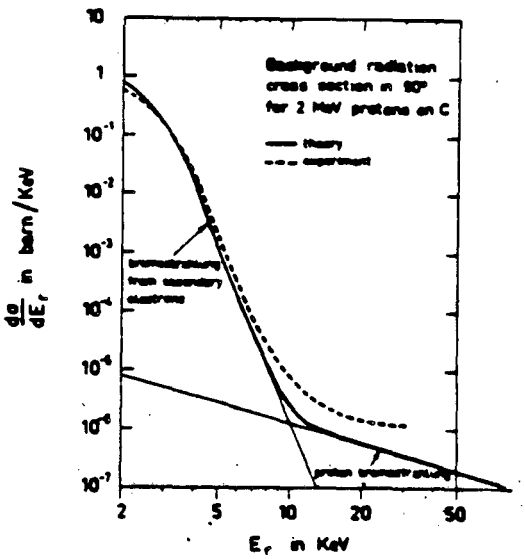

Fig. 17. Experimental and theoretical background radiation cross section for a thin sample. (FF 74).

High energy background radiation caused by gamma ray emission (Fig. 15c) is a problem at high projectile energies and/or large projectile masses [JJ 76]. High energy projectiles have a higher probability of penetrating inside the Coulomb barrier caused by the electrostatic repulsion between the nucleus and the projectile, interact with the nucleus of target atoms, and cause the emission of gamma rays. Some of the gamma rays interact with the atoms in the detector via Compton scattering. This causes a high energy background signal to be present in the spectrum. Background from γ-ray emmission becomes dominate when proton energies are in the range of 3-5 MeV and for target atoms of Z greater than 30. Therefore, projectile energies should be as low as possible for minimum background. Again, this

background radiation can be reduced by lowering projectile mass and energy and by shielding the detector from direct δ-radiation from the target chamber [JJ 76].

2.13.2 Absorption

Absorption of characteristic x-rays by the sample and by windows in the scattering chamber and detector must be accounted for when doing PIXE analysis. Absorption can be a severe problem which will affect the sensitivity when impurity concentrations in the sample are low, the x-ray production cross section of a particular element is low leading to low x-ray yield, or when energy of the characteristic x-ray of an impurity lies just above and close to the absorption edge of the sample. Thin samples usually do not experience a significant absorption problem since the induced x-rays do not have to travel through a large amount of absorbing media. Absorption in thick samples such as bulk GaAs, however, must be accounted for in computations of impurity concentrations. Absorption of x-rays is given by the equation:

$$I = I_0 \exp^{-\alpha x}, \qquad (25)$$

where Io is the initial x-ray intensity, α is the mass absorption coefficient of the medium through which the x-rays are passing, x is the thickness of the medium, and I is the final x-ray intensity. For compounds the mass absorption coefficient is given by Bragg's Rule [CB·78]:

$$\alpha_{cpd} = w_1\alpha_1 + w_2\alpha_2 , \tag{26}$$

where α_{cpd} is the absorption coefficient of the compound, w_1 and w_2 are the weight fractions of elements 1 and 2 of the compound, respectively, and α_1 and α_2 are the absorption coefficients of elements 1 and 2, respectively. The absorption of characteristic x-rays by the sample enters into the general PIXE equation (Eq. 10) in the integral of the energy dependent x-ray production cross section for thick samples. For thin samples the absorption is usually negligible.

2.13.3 Sensitivity

As stated, the overall sensitivity of the PIXE technique is determined by the background radiation level, absorption of characteristic x-rays by the matrix, and detector and instrumentation characteristics. Here sensitivity is defined as the minimum detectable concentration of trace elements in a matrix.

In order for an element to be detected its' x-ray peaks must rise above the background (Fig. 17) in a statistically significant manner [GJ 73]:

$$N_p > 3(N_b)^{1/2}, \tag{27}$$

where N_p is the number of counts in the peak and N_b is the number of counts in the background. The x-ray yield is determined largely by the production cross section. The BPWA and the BEA both predict

decreasing cross section with atomic number (Fig. 18).

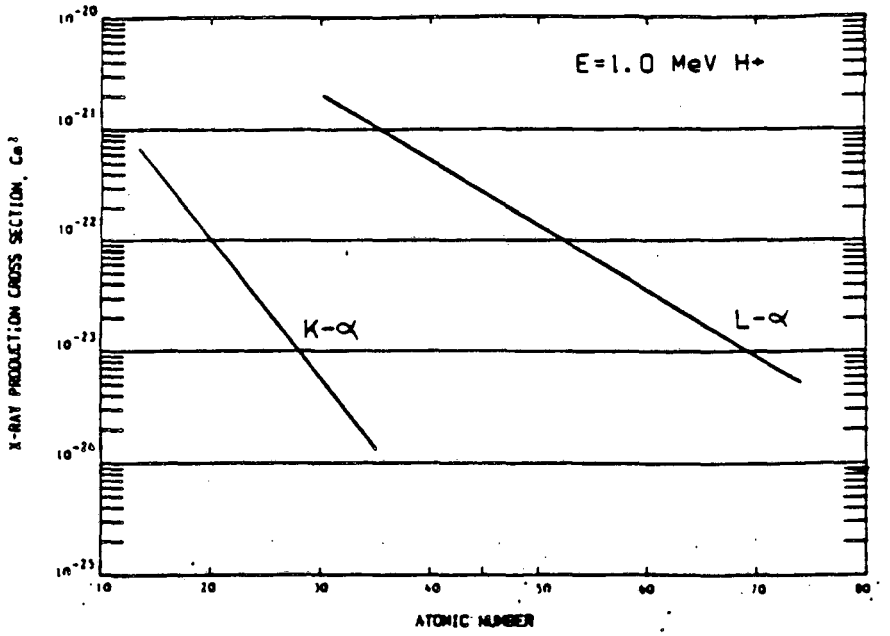

a)

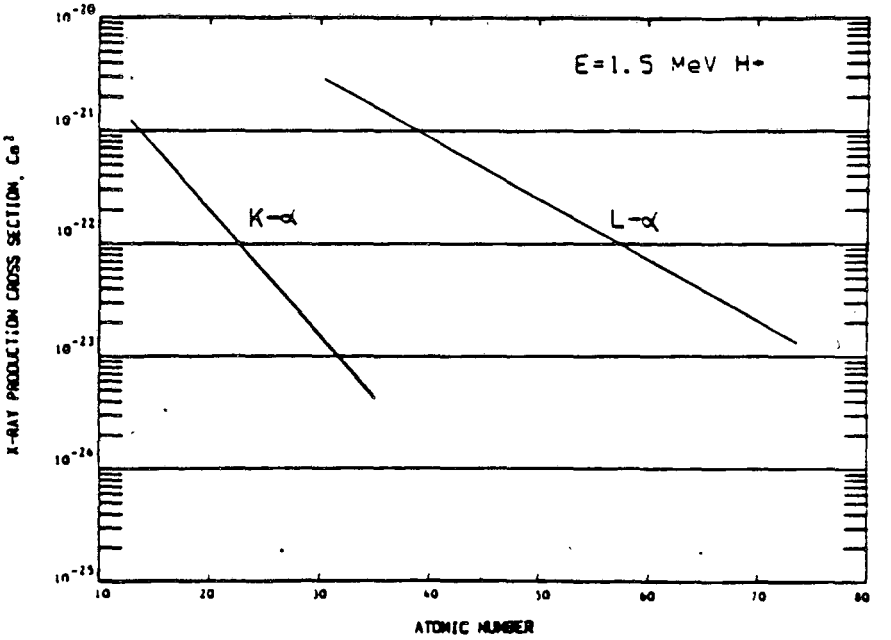

b)

Fig. 18. Variation of K- and L- shell x-ray production cross sections with atomic number. a) E_0=1.0 MeV H^+, b) E_0=1.5 MeV H^+. Results are calculated from Eqs. 35 and 36 using the data in Table II.

At Z = 40 the K-α x-ray production cross section is too small for use in trace element analysis (ie., the resulting intensity is too low). However, the intensity of the L-α x-rays is such that they can be used. In this manner a minimum detectable limit that is fairly constant over nearly the entire periodic table can be realized [JJ 76]. It has been shown [JJ 76] that for thin films sensitivity scales as:

$$\Delta E^{1/2}(\Omega jt)^{-1/2}, \tag{28}$$

where ΔE is the detector resolution, j the collected charge, the solid angle, and t the target thickness. Using typical values (ΔE=165 eV, Ω =0.003x4π, j=10 μC, and t=0.1 mg/cm^2), Eq. 28 gives a minimum detectable concentration profile as shown in Figure 19.

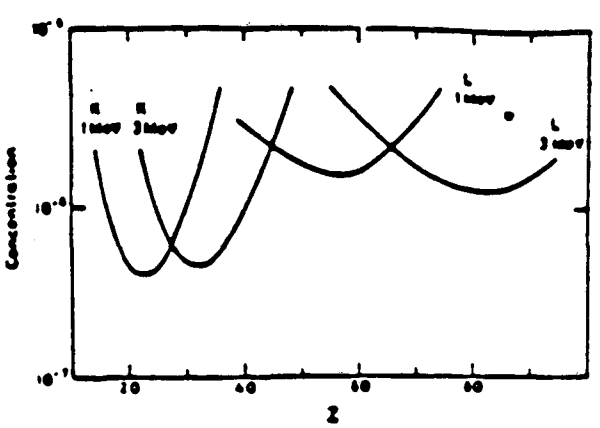

Fig. 19. Minimum detectable limit of concentration of trace elements as a function of atomic number for 1 and 3 MeV protons. Experimental parameters are as defined in the text. (JJ 76).

This is a general shape and is to be expected for most matrices. The decrease in sensitivity for lighter elements arises from a decrease in the fluorescent yield while the decrease for the heavier elements is caused by the reduction in x-ray production cross section with the background remaining constant.

By applying the principals of background reduction discussed in the preceeding subsection it is possible to adjust the minimum point of the detectability limit curves for the particular trace element of interest. Figure 20 shows the detectability limits in C as a function of Z for protons, α particles, and ^{16}O ions.

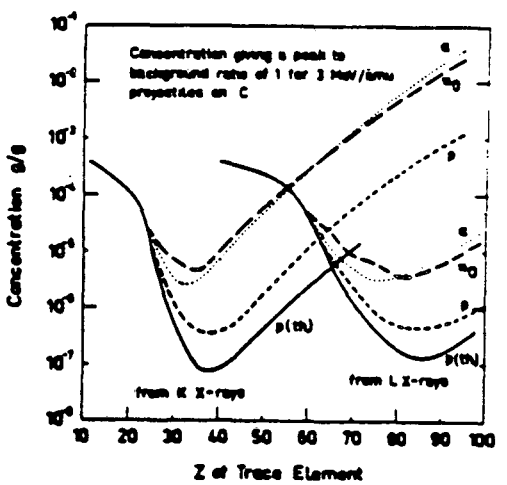

Fig. 20. Minimum detectable limit as a function of atomic number for protons, alpha-particles, and heavy ions. All energies are 3 MeV/amu. (FF 74).

The solid line is the calculated limit accounting for projectile and secondary electron bremsstrahlung. The dotted lines are the experimental values. Experimental values exceed the calculated values

as a result of γ-ray emission. When attempting to lower the background it must be remembered that, for a particular Z, a reduction of projectile energy results in a lower cross section for x-ray production and, therefore, lower x-ray yield. Increasing the solid angle of the detector via collimation may help offset the decline in x-ray yield with a decrease in projectile energy. The practical aspects of the time required to produce an x-ray spectrum must be considered when attempting to achieve background reduction. Furthermore, as projectile energies are decreased, the PIXE technique becomes more and more a near-surface analytical tool, a factor which may or may not be of importance. Ideally, the projectile should be light enough to avoid high γ-ray emission but not so light as to cause serious projectile bremsstrahlung and the energy such that the x-ray energy of interest is above the maximum energy transferred to secondary electrons but not so as to diminish x-ray yield below practical limits. In general, a spectrum produced with higher energy particles will exhibit poorer signal to background ratios in the region below E_{max} as a result of increased secondary electron bremsstrahlung, while lower energies above E_{max} will show a decrease in background from γ-ray emission but an increase from projectile bremsstrahlung. Therefore, for purposes of general PIXE analysis, protons of 1-1.5 MeV appear to be the optimum choice.

Absorption will affect the sensitivity of a system analyzed by PIXE through attenuation of x-rays produced within a thick sample. The mass absorption coefficient of a matrix is a property of the elements of which it is comprised. Therefore, given the appropriate x-ray yield and backround radiation characteristics, it can be used to

predict the intensity of x-rays that will be detectable at the surface of a thick sample. X-rays of elements which lie below absorption edges of the matrix will not be as strongly attenuated as those which lie above those edges. This therefore has an important effect on sensitivity of PIXE analysis and will markedly effect the smooth shape of the curve shown in Figure 19. Figure 21 shows x-ray intensity at the surface vs depth for two elements in GaAs. X-Rays from light elements will be strongly absorbed by detector windows and any existing air gaps in the experimental set up. Other than using as thin as windows as possible (or a windowless detector system, if feasible) and flushing air gaps with He, there is not much that can be done to reduce these limits on sensitivity.

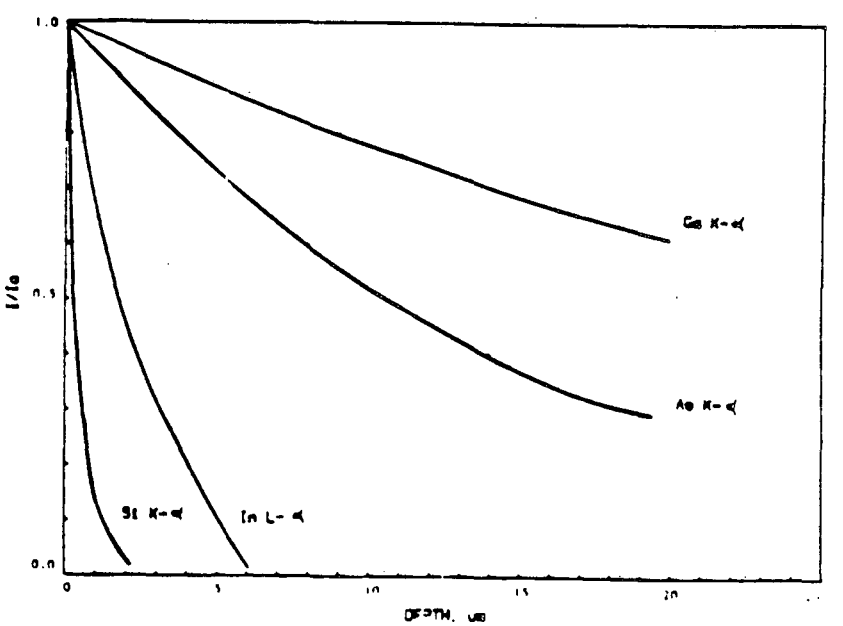

Fig. 21. Intensity of x-rays reaching the surface of GaAs as a function of depth for Ga, As, and Si K-α and In L-α x-rays. Results calculated using Eq. 25.

The limits imposed on sensitivity by the detector and other experimental effects include [FF 74]:

1) Detector energy resolution (full width at half maximum (FWHM))
2) Low energy tails from characteristic x-ray peaks
3) Limited counting rate of the detector
4) Heating and charging of the sample

Parameters 1) and 3), are optimized by the manufacturer of the detector and its amplifiers and pile-up rejection system. Small tuning adjustments can be made to the signal levels which the detector processes as an event; filters and collimators can be used to decrease the counting rate. The effects of 2) are a result of insufficient charge collection in solid state detectors which show up as a low energy counting rate. Collimating the x-rays to strike only the active area of the detector or use of a guard ring detector reduces the significance of this problem. Heating of the sample is not usually a problem in semiconductor studies as for typical values of current density the sample temperature is below 100°C [HM 81]. Charging of thick samples can be eliminated by attachment of the sample to a conducting base via conductive paint and/or by placement of a shielding ring held at the proper voltage for electron suppression around the sample. Without shielding, electrons released from the sample may be accelerated by electric fields in the chamber, strike chamber walls, and produce bremsstrahlung. Chaudhri and Crawford [CC 81] employ a thin film in front of the sample as a source of electrons to eliminate positive charging of the target.

There are no general expressions that can be used to determine what the sensitivity of PIXE will be for a given system. Therefore, sensitivity for each particle-matrix combination must be individually calculated and measured experimentally. The examples shown are for thin films. In the case of thick films, the increase in projectile bremsstrahlung resulting from the projectile losing energy as it penetrates the target will add about a factor of ten to the values in Figure 19 [FF 74]. Observing the trends in Figure 20, another factor of ten for mid-Z targets such as GaAs is to be expected (resulting mainly from absorption).

A purpose of this study was to experimentally measure the minimum detectable limit of trace elements in bulk (thick) GaAs.

2.14 Semi-Empirical Approximations

Extremely important to thick target analysis by PIXE is the choice of method used to evaluate the integral in Eq. 10. This integral accounts for the energy loss of the projectile as it penetrates the sample, the associated decrease in the x-ray production cross section, and for absorption of characteristic x-rays by the sample over the range of the projectile. Ultimately, then, this is used to determine the concentration of impurities present and the overall sensitivity of the system. Therefore, an important part of this project was to devise a semi-empirical method based on the properties of the target under projectile bombardment to approximate the ion-solid interaction responsible for the production of x-rays.

The resistance to penetration of a target by energetic charged particles is expressed in terms of the stopping power of the matrix. Anderson and Ziegler [AZ 77] have presented a nearly complete compilation of experimental energy-loss data for hydrogen in the elements over the range of 10 keV < (E/amu) < 20 MeV. The energy loss process at low energies is composed of two parts: electronic energy loss (via ionization and excitation) and elastic energy loss to the screened nuclei (nuclear stopping). For hydrogen the nuclear stopping is usually small (~.01-.02 of the total stopping power at 10 keV) [AZ 77]. The electronic contibution to stopping is then given by [LS 61]:

$$S_e = z^{1/6} 8\pi e^2 a_o \frac{zZ}{(z^{2/3}+Z^{2/3})^{3/2}} \times \frac{v}{v_o} , \qquad (29)$$

where z and Z are the atomic numbers of the projectile and target, respectively, v is the projectile velocity, e the electronic charge, and a_o and v_o the Bohr radius of the hydrogen atom and the Bohr velocity. Note that this stopping is proportional to $z^{1/6}$ and to the projectile velocity.

Stopping at higher energies is well described by the Bethe-formula:

$$S = \frac{4\pi z^2 Z^2}{mv^2} [\ln(\frac{2mv^2}{I}) + \ln(\frac{1}{1-\beta^2})^2] - \beta - \frac{C}{Z} , \qquad (30)$$

with m the electron mass, z and Z the projectile and target mass, respectively, $\beta = v/c$ where c is the velocity of light, and C/Z are the shell corrections. I is the mean excitation parameter and is

approximated using Thomas-Fermi arguments by Bloch's rule [AZ 77]:

$$I = I_0 Z \ , \tag{31}$$

where I_0 is ~10 eV.

The conribution of Anderson and Ziegler was to formulate expressions for the intermediate energy range of proton bombardment; For proton energies of 1-10 keV:

$$S = A_1 E^{1/2}, \tag{32}$$

For proton energies of 10-999 keV:

$$(S_{TOT})^{-1} = (S_{LOW})^{-1} + (S_{HIGH})^{-1}, \tag{33a}$$

$$S_{LOW} = A_2 E^{0.45}, \tag{33b}$$

$$S_{HIGH} = (A_3/E)\ln[1+(A_4/E)+(A_5 E)] \ , \tag{33c}$$

For proton energies from 1-100 MeV:

$$S = (A_6/\beta^2)[\ln(\frac{A_7\beta^2}{1-\beta^2}) - \beta^2 - \sum_{i=0}^{4} A_{i+8}(\ln E)^i] \ , \tag{34}$$

where the constants A-1 through A-12 are tabulated in the reference. All equations are in eV/10^{15} atoms/cm^2.

As mentioned, a key result of the BEA theory is the scaling of ionization cross section with projectile energy as a function of the atomic number of the projectile and the binding energy of the electrons in the shell of the target atom in question. Thus universal plots are obtained. This result was applied to the approximation for the integral in Eq. 10. Listed in the appendix of the paper by Garcia [JG 73] are the values of the points on the universal plots of scaled

cross section versus projectile energy. The curve was fit by the method of least squares to obtain a polynomial expression for the variation of ionization cross section with energy for the K and L shells. A polynomial of degree 2 of the form:

$$\log(u^2\sigma_i/z^2) = b_0 + b_1\log(E/\lambda u) + b_2(\log(E/\lambda u))^2, \quad (35)$$

gave the best fit over the range of interest ($E/\lambda u = 10^{-2}$ to 10^{-1}). The expression for the binding energy of L-shells used was that which was suggested by Johansson and Johansson [JJ 76]:

$$u_L = 1/4(u_{L_1} + u_{L_2} + 2u_{L_3}) . \quad (36)$$

Once the ion energy for a particular projectile/matrix system is known, the value of the ionization cross section can be calculated using the polynomial expression for the shell in question. Table II lists the fitting parameters.

TABLE II

UNIVERSAL CROSS SECTION FITTING PARAMETERS

SHELL	b_0	b_1	b_2
K	-18.9678	0.4111	-0.9568
L	-18.1829	0.7795	-0.8325

The expressions for the stopping power (Eqs. 32-34) and the polynomial fits (Eq. 35) were incorporated into a computer program to

calculate the energy at specified depth intervals over the range of the particle in the target as determined from the range plots published in the reference [AZ 77]. Thus, the energy versus depth profile of protons with E_0 = 1.0 and 1.5 MeV in GaAs (Fig. 22) was calculated.

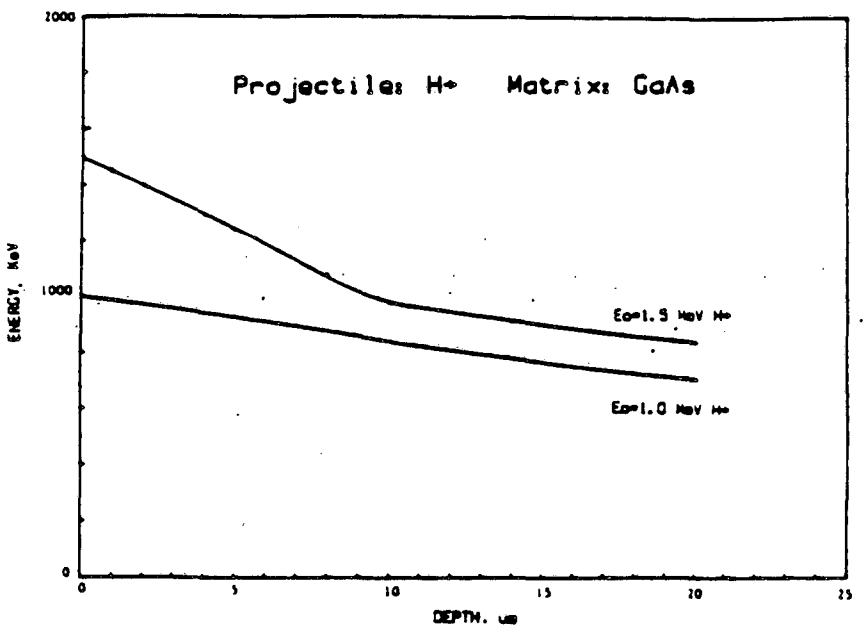

Fig. 22. Proton energy vs. depth in GaAs for E_0=1.0 and 1.5 MeV. Curves are calculated using Eqs. 32, 33, 34.

The constants (A-1 - A-12) used were the averages of each for Ga and As. The atomic density of GaAs was used to convert eV/10^{15} atoms/cm^2 to eV/μm. The energy calculated at each depth interval was used to calculate the x-ray production cross section of the element of interest (Fig. 23).

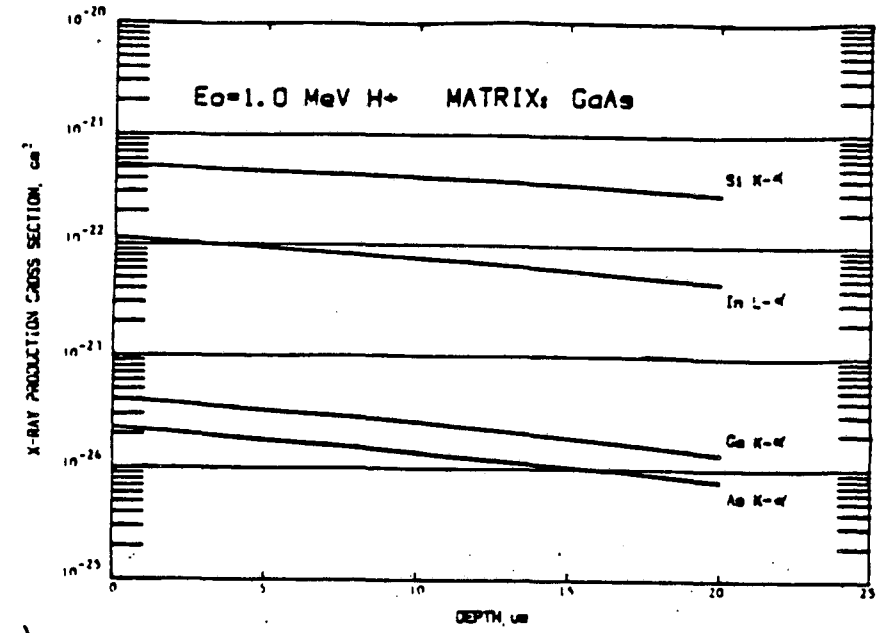

a)

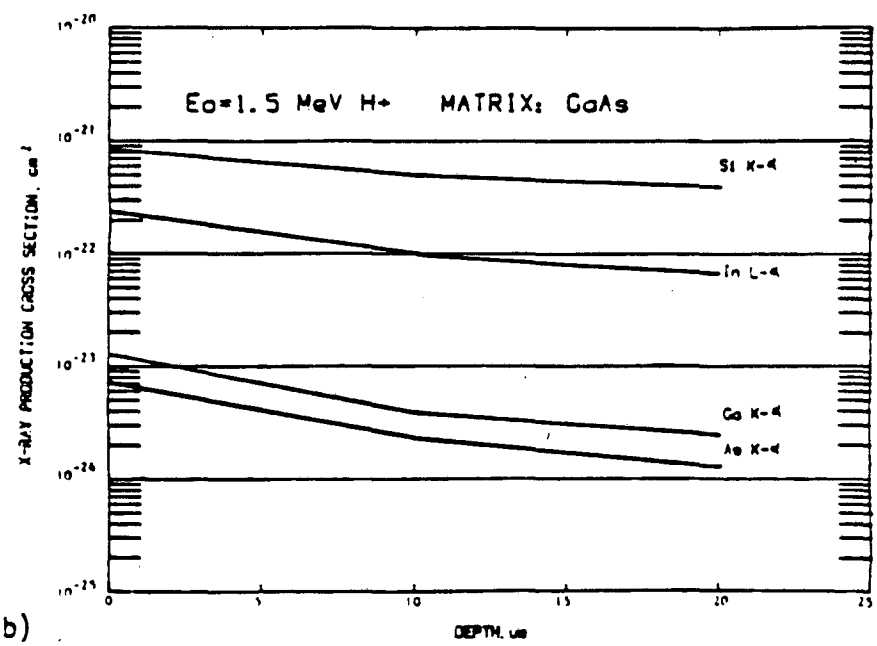

b)

Fig. 23. Variation of x-ray production cross section vs depth in GaAs for Ga, As, and Si K-α and In L-α x-rays for a) E_0=1.0 MeV protons and b) E_0=1.5 MeV protons. Results are calculated using Eqs. 32-36 and the data in Table II.

The absorption from each depth (of the form of Eq. 25) was included in the calculation so tnat the integral in Eq. 10 was replaced by a summation:

$$N_i = I_0 \rho_i \frac{\Omega}{4\pi} \epsilon_i \prod_{j=1}^{n} a_j \omega_i \Delta x \sum_{k=0}^{R} \sigma_{i_k}(E(x)) e^{-\alpha x}, \qquad (37)$$

where the interval Δx was chosen to be very small (~nm) and R is the range of the projectile. The program was written so as to allow the constants A-1 through A-12 for any target material to be input to the program for calculation.

2.15 Data Analysis

The removal of background radiation, peakfitting, and concentration calculation were accomplished using established techniques and standard statistical methods. Each experiment included the measurement of background radiation by analyzing an undoped sample of GaAs. The counts over the intervals A-A' and B-B' on eacn side of the dopant peak (Fig. 24) were determined for both the undoped and doped samples. The ratio of sample to standard counts was computed. The ratio multiplied by the counts (in a single channel) in the standard was subtracted, channel by channel, from the corresponding channel in the sample spectrum. The error in this process is given by:

$$\sigma_p = (\sigma^2_{sample} + R^2 \sigma^2_{std})^{1/2}, \qquad (38)$$

where σ_p is the standard deviation of the counts in the peak after

background removal, R is the ratio of counts in the sample spectrum to counts in the standard spectrum over the intervals A-A' and B-B', and σ^2 is the variance in counts for the sample and the standard over the interval A'-B. The peaks in the background-removed sample spectrum were fitted to a Gaussian distribution using a linear least-squares fit to the derivative of the portion of the spectrum containing the peak. The concentration of the dopant was then found by substitution into Eq. 37 and solving for ρ_i. The geometry and detector efficiency were found by measurement using a Pd thin film standard of known thickness.

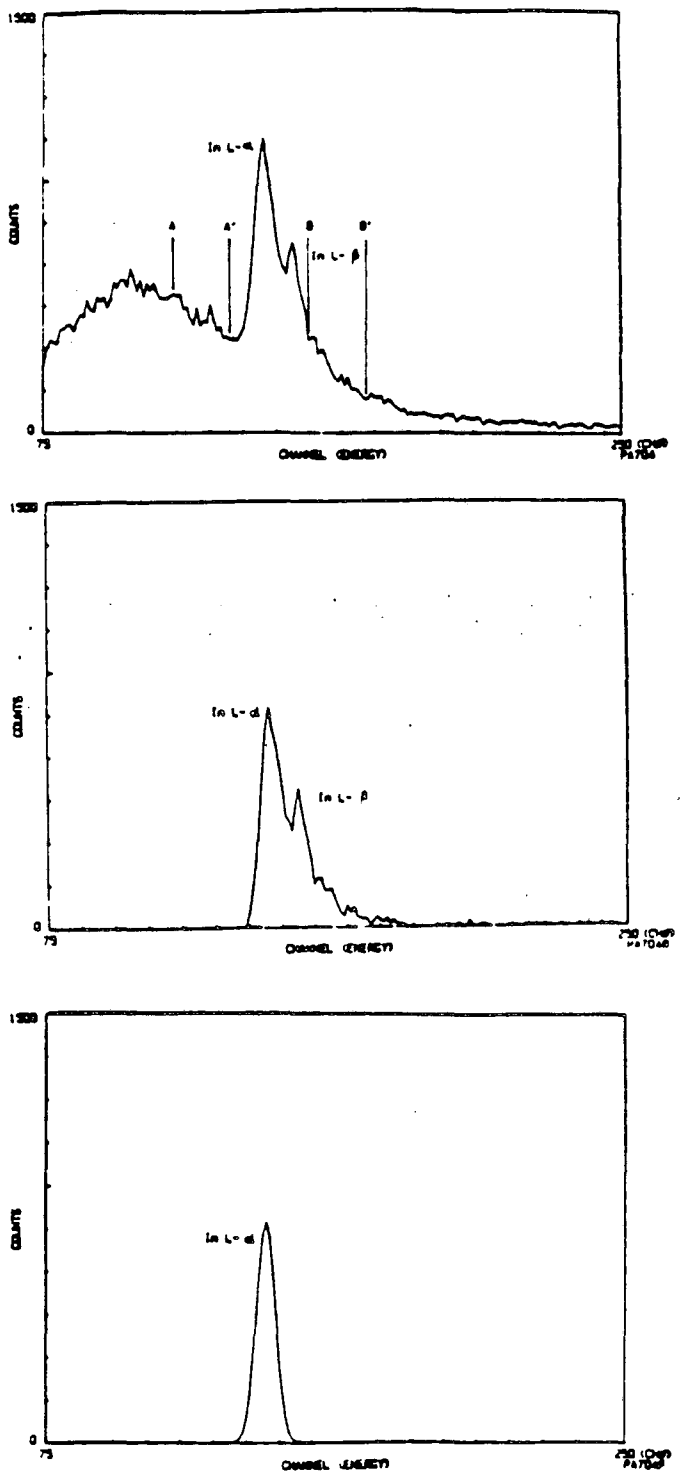

Fig. 24. Results of background removal and peak fitting procedures. a) Raw spectrum, b) characteristic x-ray peak after background removal and, c) final fitted peak.

2.20 Channeling

2.21 General

Crystalline solids can be viewed as rows of atoms that are arranged in a regular, periodic order in space. A fraction of a beam of energetic ions incident upon a crystal in which the atomic rows are oriented in a random direction to the beam experience large angle scattering, or backscattering. As the angle between the beam and a major crystal axis approaches zero the influence of the crystal lattice on the trajectory of the ions becomes noticable. The backscattered particle yield decreases significantly as the ions are guided by small angle scattering along the rows of atoms. This is attributed to the presence of large "holes", or channels, along major crystallographic directions through which projectiles pass without experiencing large angle scattering , hence the term "channeling". This process and the resulting RBS spectra are illustrated schematically in Figure 25.

Crystals with diamond and, in the case of gallium arsenide, the zinc-blend structure crystals posses large channels in the <100>, <110>, and <111> directions. Figure 26 shows a gallium arsenide crystal oriented in a random direction and the resulting planar projections of the major crystallographic directions.

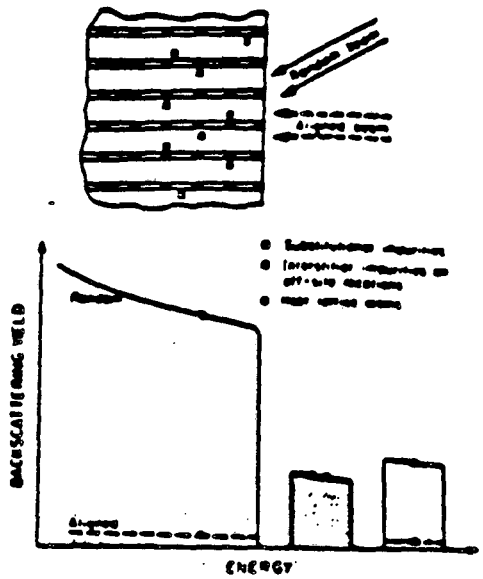

Fig. 25. Comparison of backscattered spectrum for random and axially aligned directions. Substitutional impurity yield decreases with that of the host crystal while the yield of the interstitial impurity does not. (Courtesy EH MSE 223).

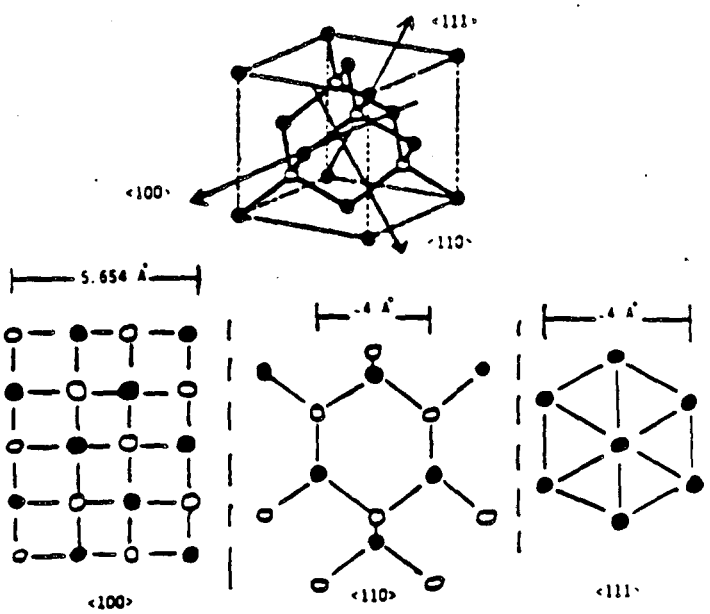

Fig. 26. a) ZnS structure of GaAs. Ga atoms are represented by the darkened circles, As by open. b) Projections of the major axial directions in GaAs.

The Thomas-Fermi screening distance predicts the distance of closest approach of the projectile ion to the row of crystal atoms that constitute the channel wall. This parameter descibes the distance from the positive ion core where the Coulomb potential is 1/e of the value of the bare Coulomb potential as a result of screening of the positive ion core by the surrounding electron cloud. Positively charged projectiles are able to approach the ion cores to this distance before being repulsed, or scattered, back into the channel by the effects of Coulomb repulsion of like charges. The value of the Thomas-Fermi screening distance is given by [AF 77, GD 74]:

$$a = \frac{0.4685}{(z^{1/2} + Z^{1/2})^{2/3}} \text{ Å}, \tag{39}$$

where z is the atomic number of the projectile and Z is the atomic number of the target. The value of the Thomas-Fermi screening distance in gallium arsenide appears in Table III.

Atoms of a crystal vibrate about their equilibrium lattice positions and as such affect the trajectory of the channeled particles. The one dimensional rms vibrational amplitude estimated from the Debeye approximation [BM 55] is given by:

$$u_1 = 12.1\left[\frac{(\phi(x)}{x} + 1/4)(M_2\Theta)^{-1}\right]^{1/2} \text{ Å}, \tag{40}$$

where Θ is the Debeye temperature, $x = \Theta/T$ (T is temperature of the crystal), and $\phi(x)$ is the Debeye function. Values for the Debeye function are given in Figure 27, the value of the Debeye temperature for GaAs in Table III.

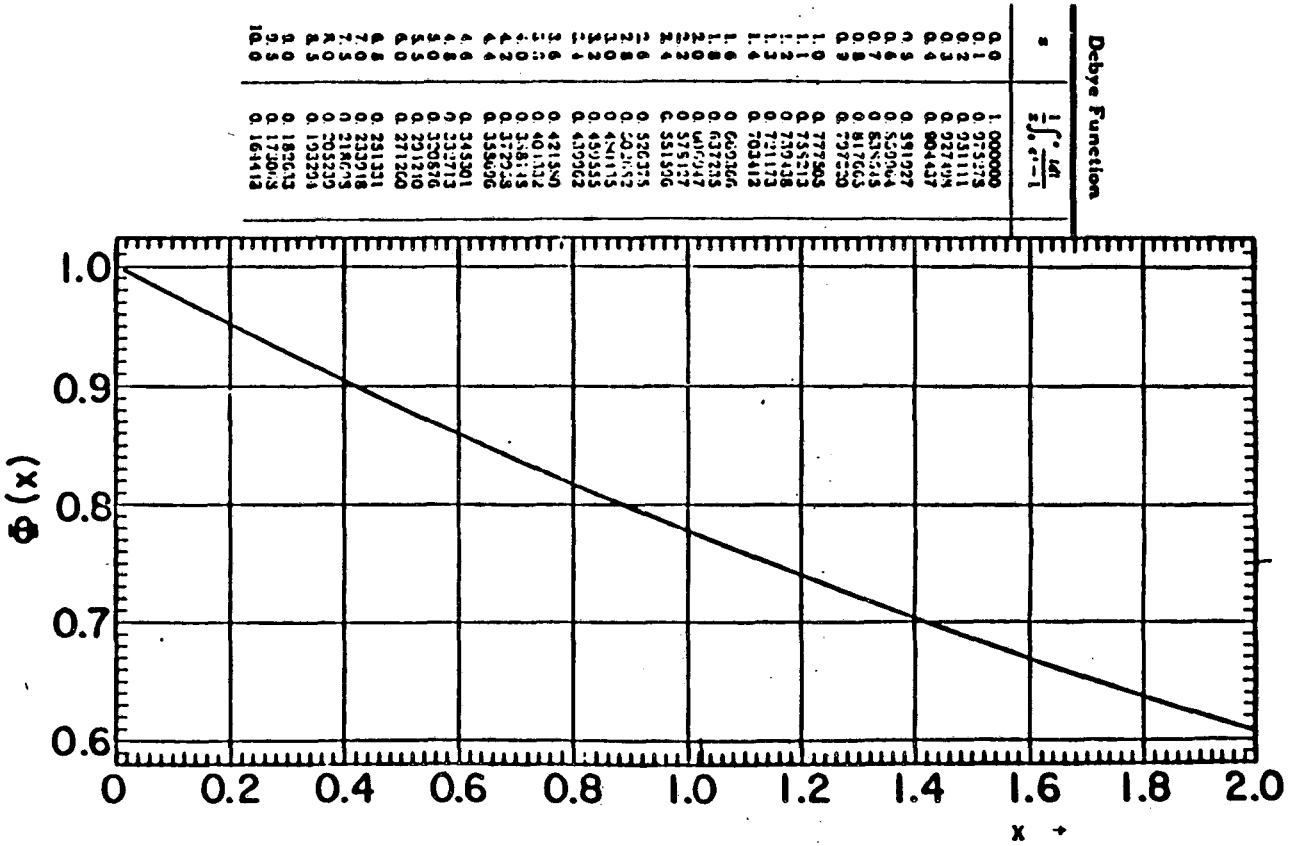

Fig. 27. Graph of the Debeye function, $\phi(x)$, vs. x. (AF 77).

2.22 Surface Interactions

A useful model which is helpful in understanding the onset of channeling behavior is the static, two atom crystal model. The channeling process begins at the surface where the crystal atoms guide the incident ions into the channels. Those that are not channeled are backscattered and give rise to the surface peak that is present in channeled RBS spectra (Fig. 28). The uniform flux of the beam is initially perturbed by scattering from the surface layer of atoms; those ions which are not backscattered but are guided by small angle scattering into the channel shield the atom (atoms in real crystals) behind the surface atom leading to the formation of the shadow cone. When the channeling phenomenon takes place, projectiles do not follow trajectories which take them inside the radius of the shadow cone and therefore do not interact with the second atom.

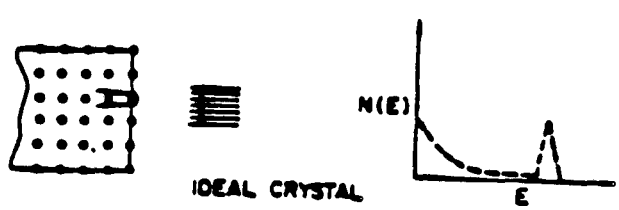

Fig. 28. Schematic of the channeling process showing origin of the surface peak in a RBS spectrum. Particles interacting with the surface atoms are responsible for this feature. (FMP 82).

In order for axial channeling to occur, the radius of the shadow cone must be greater than the impact parameter for large angle (backscattering) scattering. As a first approximation [FMP 82] classical Coulomb scattering applied to a two atom system can be used to describe the initial path of the incident ion. For a surface atom with impact parameter r_1 the angle of scattering is given by:

$$\phi = \frac{zZe^2}{Er_1}, \tag{41}$$

where z and Z are the atomic numbers of the projectile and target, respectively, E is the energy of the incident projectile, and e^2 is the electronic charge and is equal to 14.4 eV-Å . The impact parameter at the second atom in the row seperated by distance d is (Fig. 29):

$$r_2 = r_1 + \frac{zZe^2 d}{Er_1} \text{ Å}, \tag{42}$$

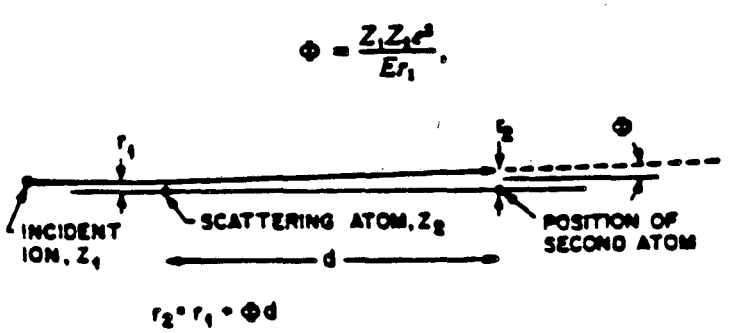

Fig. 29. Schematic of small angle scattering of the incident ion off of the surface atom leading to the formation of the shadow cone. (FMP 82).

The minimum Coulomb shadow cone radius, r_{2min}, is then given by [FMP 82]:

$$r_{2min} = R_c = 2(zZe^2d/E)^{1/2}\ \text{Å}\ , \tag{43}$$

and is shown graphically in Figure 30 for <111> GaAs. Large angle scattering occurs at impact parameters of $\sim 10^{-12}$ cm and shadow cone radii are of the order of $\sim 10^{-9}$ cm. Therefore, the second atom (in a row in real crystals) only experiences ions with impact parameters greater than the shadow cone radius and as such is shielded from nuclear collisions (Fig. 31). Hence, the channeling phenomenon in this static, two atom crystal will be observed.

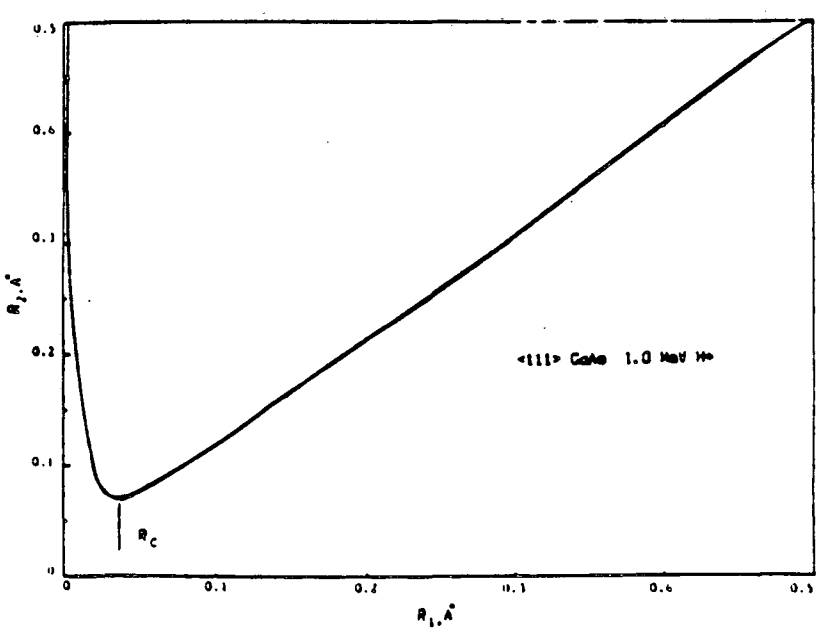

Fig. 30. Plot of R_2 vs. R_1 for <111> GaAs showing R_2 min of the shadow cone. Curve calculated using Eqs. 42 and 43.

Actual atoms in a crystal lattice vibrate as a result of thermal energy about their equilibrium positions. The root mean square vibrational amplitude in a plane normal to the beam is given by [GD 74]:

$$u_{rms} = 2^{1/2} u_1 \ , \tag{44}$$

where u_1 is the one dimensional rms vibrational amplitude of Eq. 40. These vibrational amplitudes are on the order of the shadow cone radius so will be of significance in determining the close-encounter probability (large angle backscattering probability) of incident ions with the second atom (and further atoms in real crystals) in the row. If the ratio of u_{rms}/R_c is less than 1, the second atom will be shielded. If this ratio is greater than or equal to 1, there will be substantial interaction between the second atom and the ions of the beam [FMP 82], (Fig. 31). In order to estimate the close-encounter probability of the beam with the second atom, a useful approximation to the flux distribution at the second atom in the Coulomb approximation has been devised [FKS 77]:

$$f(r) = \begin{cases} 0 & r < R_c \\ 1 + \frac{R_c^{\,2}}{2} \frac{\delta(r-R_c)}{r} \ , & r > R_c \end{cases} \ , \tag{45}$$

where r is the distance from the equilibrium position of the second atom. The flux and position distribution (Fig. 32) show that there

For Number Sequence Only

are no projectiles in the shadow cone.

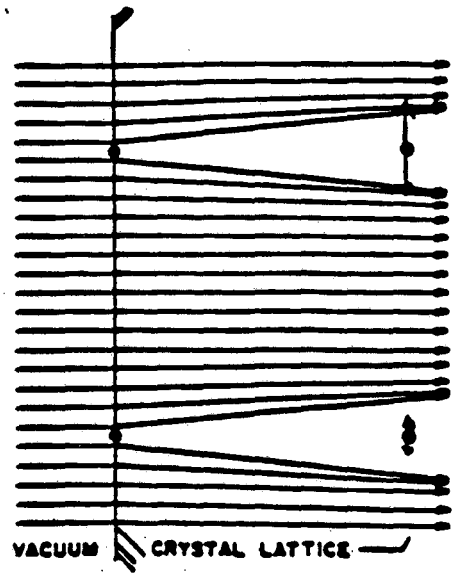

Fig. 31. Schematic of flux distribution about the shadow cone. Upper situation shows $u_{rms}/R_M > 1$, lower shows $u_{rms}/R_M < 1$. (FMP 82, in part).

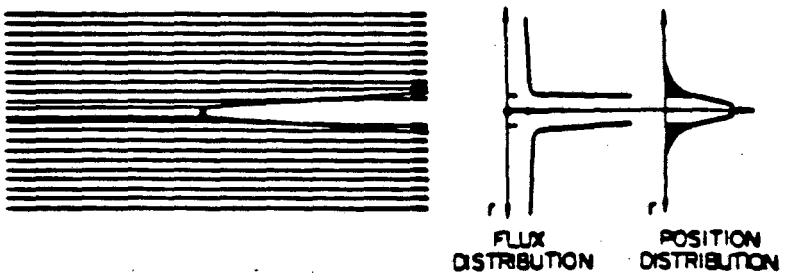

Fig. 32. Schematic of two-atom shadow cone and the associated flux and particle position distributions of the beam. (FMP 82).

Thermal motion of the second atom at position r governs the position distribution of tne particles in the flux and is given by the Gaussian [MA 62]:

$$P(r) = \frac{1}{\pi\rho^2} e^{-r^2/\rho^2} \quad , \tag{46}$$

where ρ is the two dimensional rms vibrational amplitude, u_{rms}, and r is the distance of the second atom from its' equilibrium position. Figure 32 shows the overlap of the flux and position distributions which gives the contribution to the backscattered yield from the second atom:

$$P_2 = \int_0^\infty f(r)P(r)2\pi r dr \tag{47}$$

which upon integration yields [FKS 77]:

$$P_2 = e^{-(R_c^2/(2\rho^2)} [1 + \frac{R_c^2}{2\rho^2}] \tag{48}$$

The first term (equation multiplied) describes the probability that the two atoms have a relative displacement greater than R_c which allows interaction between the beam and the second atom. The second term represents the scattering from the enhanced flux at R_c. The value of this two-atom approximation lies in the prediction that close-encounter processes are a function of one parameter, ρ/R_c [FKS 77].

The fact that the impact parameters influencing the flux distribution in this model are large compared to the actual radius of the inner electron orbits of the crystal atoms, and, when compared to experimental results, indicates that the bare Coulomb approximation is by itself not sufficient to describe the behavior of the beam. Therefore, Moliere [GM 47 and FMP 82] has developed a numerical approximation for screening of the nucleus by the surrounding electrons based on the Thomas-Fermi model. This treatment relates the screened shadow cone radius to the radius predicted by the bare Coulomb model via the Thomas-Fermi screeneing distance. The Moliere approximation is given by:

$$V(r) = \frac{zZe^2}{r}[0.1e^{-6r/a} + 0.35e^{-0.3r/a} + 0.55e^{-1.2r/a}], \quad (49)$$

where r is the distance from the nucleus in spherical coordinates and a is the Thomas-Fermi screening distance. Figure 33 [SFS 78] shows the relationship between the screened and unscreened shadow cone radii. R_c is given in Eq. 43.

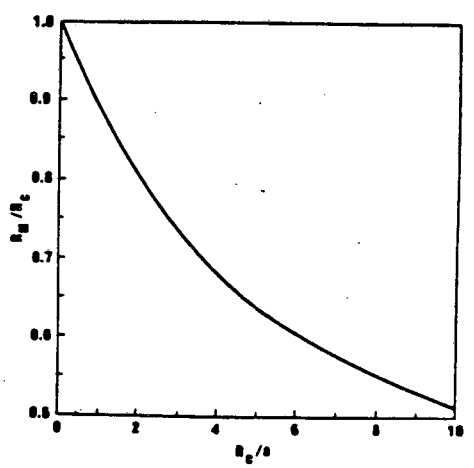

Fig. 33. Universal curve showing the ration of the shadow cone radius for bare Coulomb and screened Moliere' potential as a function of reduced Coulomb potential shadow units. (SI 78).

2.23 Channeling Within the Bulk

2.23.1 The Continuum Model

Channeling within the bulk of the crystal is most often described by the Continuum Model proposed by Lindhard [LJ 65] with elaborations by Gemmell [GD 74] and others. The basis for the Continuum Model is that, under certain conditions, the channeling effect for projectiles with a mass greater than or equal to that of a proton can be described by classical mechanics. When projectile energies are high (on the order of a few MeV) and/or the angles of deflection are small (the channeling condition) the individual ion-atom collisions must be treated within the framework of quantum mechanics. However, Lindhard showed that classical mechanics can be applied to a theory of channeling if the potential arising from the individual atoms of the row is considered to be uniform and constant along the length of the row, hence a continuum potential. The individual, binary, ion-atom collisions are then replaced by a series of very small angle deflections of the ion off of the potential wall continuum. Each very small angle deflection, $\Delta\phi$, is smaller than the total small angle, ϕ, through which the projectile trajectory is altered, or $\Delta\phi \ll \phi$ (Fig. 34). The model then describes the geometric conditions which must be satisfied for channeling to occur.

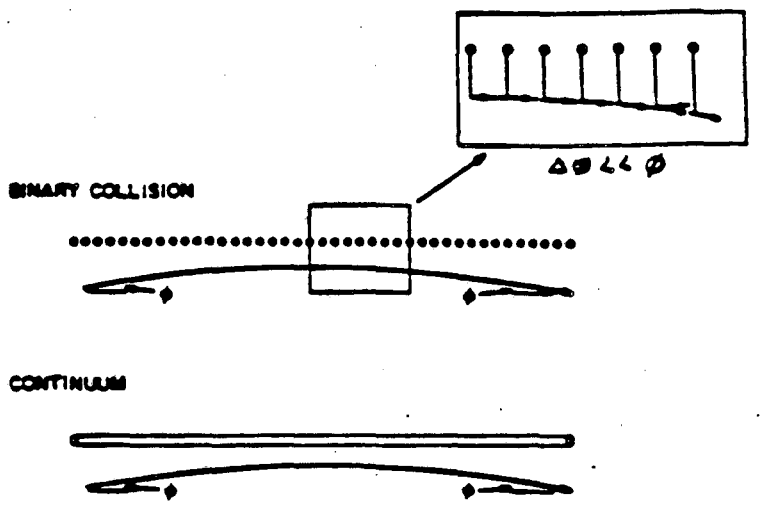

Fig. 34. Continuum Model approximation for an atomic row. Shows correlated sequence of small angle scattering from individual atoms replaced by a single continuum potential. (FMP 82).

The Continuum Model is applicable to both axial and planar channeling cases. There are, however, differences in the details of the expressions for comparable quantities between the two. Axial channeling will be highlighted here. If r is the distance from an isolated atom row, d is the interatomic distance, and the geometry is as defined in Fig. 35, the continuum potential, $V_{RS}(r)$, at r from a static row of atoms is given by [GD 74]:

$$V_{RS}(r) = \frac{1}{d} \int_{-\infty}^{\infty} V[(r^2 + x^2)^{1/2}]\, dx, \qquad (50)$$

where V can be described by an expression of the form of Eq. 49 ie.; a

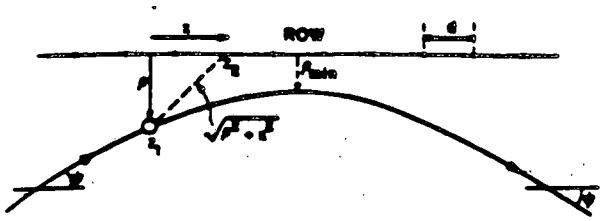

Fig. 35. Geometry of the collision of a channeled particle with an idealized static atomic row. (GD 74).

classical Coulomb potential modified by a Thomas-Fermi type screening function. However, a "standard potential" most often used (as opposed to the Moliere potential) for its precision in analytic treatment of channeling parameters is [FMP 82]:

$$V(r) = zZe^2\left[\frac{1}{r} - \frac{1}{(r^2 + C^2a^2)^{1/2}}\right], \tag{51}$$

where a is the screening distance, C^2 is equal to about 3, and r is the distance from the atomic row. This then gives the axial continuum potential as:

$$U_a(r) = \frac{zZe^2}{d} \ln\left[\left(\frac{Ca}{r}\right)^2 + 1\right], \tag{52}$$

The motion of axially channeled particles is quite complex. Therefore, even with the simplification of the static-continuum potential a theoretical description is difficult. A further simplification is that the channeled particles interact only with isolated rows of atoms; the influence of other rows is neglectd. Gemmell points out [GD 74] that, in the case of the major crystallographic directions, this approximation is valid as the distances between the rows are large and, as such, the potential decreases rapidly with distance. The total energy inside the crystal is the sum of the kinetic and potential energies [FMP 82]:

$$E_{TOT} = \frac{p_x^2 + p_y^2 + p_z^2}{2M} + U(r), \tag{53}$$

where p_i is the momentum in the ith direction, M is the projectile mass, and U(r) is the potential energy. The total energy and the projectile energy in the forward direction, p_z^2/M, are constant over the dimensions of the particle deflection so that the remaining term, $(p_x^2 + p_y^2)/2M$, is the expression for the transverse energy, E_T. This energy is also constant and the incident and exit angles of the channeled projectile are conserved leading to the conclusion that, in order for axial channeling to take place (within the constraints of the above simplifications), E_T must also be conserved:

$$E_T = E\phi^2 + U(r), \tag{54}$$

where $E\phi^2 = (p_x^2 + p_y^2)/2M$.

In an actual crystal the potential along an atomic row is not a continuum but is periodic with the periodicity of the lattice. As the projectile approaches the atomic row this periodicity influences the trajectory by affecting the scattering angle of the individual particles of the beam. There is therefore a maximum incident angle corresponding to a minimum distance of approach of the ion to the row of atoms for which the Continuum Model is valid. Particles with an angle greater than this maximum angle posses too great of a transverse component of energy (E_T) and are able to penetrate inside the Thomas-Fermi screening distance. These particles will experience large angle scattering. The maximum, or critical, angle is related to the distance of closest approach by:

$$\psi_c = [\frac{U(r_{min})}{E}]^{1/2} , \tag{55}$$

where ψ_c is the critical angle, E is the projectile energy, and r_{min} is the distance of closest approach (Fig. 36).

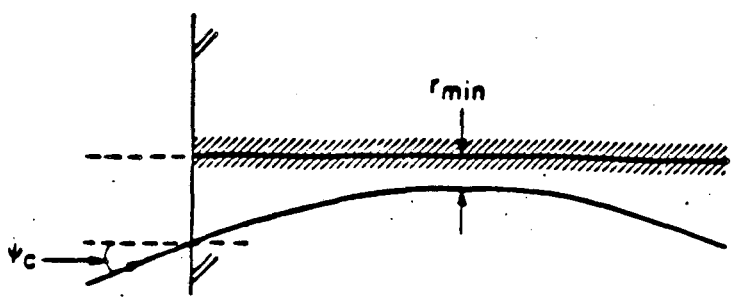

Fig. 36. Schematic of channeling trajectory showing minimum distance of approach for which the Continuum Model is valid. r_{min} can be approximated by u_{rms}. (FMP 82).

This then, sets a limit on r_{min} on the order of u_{rms}, the transverse rms thermal vibrational amplitude as defined by Eqs. 40 and 44. Approximating r_{min} by u_{rms} the critical angle for channeling is then given by [FMP 82]:

$$\psi_c(u_{rms}) = \frac{\psi_1}{(2)^{1/2}} \ln [(\frac{Ca}{u_{rms}})^2 + 1]^{1/2}, \tag{56}$$

with ψ_1, the maximum angle of approach in the basic continuum approximation, given by [GD 74]:

$$\Psi_1 = (2zZe^2/dE)^{1/2}, \tag{57}$$

This is the limit of validity of the Contimnuum Model for axial channeling in the high energy condition (ie., $\Psi < \Psi_1$) when $\Psi_1 < a/d$. The limit for the low energy regime ($\Psi_1 > a/d$) is:

$$\Psi < \Psi_2 = [Ca_1/d(2)^{1/2}]^{1/2}, \tag{58}$$

When a beam is aligned with a crystal axis the backscattered yield does not drop to zero. This is caused by a fraction of the particles in the beam having an initial transverse energy above the critical value for channeling. The expression derived by Lindhard for the minimum yield just below the surface of the crystal is:

$$\chi_{min}(\rho) = Nd\pi u_{rms}^2 + Nd\pi a^2 + \chi_3, \tag{59}$$

with u_{rms} as in Eq. 44, a is the Thomas-Fermi screening distance, d is the distance between atoms in the row, N is the atomic concentration, and χ_3 is the contribution from any amorphous or impurity layers. Since, in the small angle Coulomb approximation given by Eq. 41, the scattering angle of the projectile off of the first atom is proportional to 1/E, the minimum yield increases for decreasing energy. A particle will not be channeled unless $\phi < \Psi_1$ or [FMP 82]:

$$r_1 < (zZe^2d/2E)^{1/2}, \tag{60}$$

Therefore, at large values of zZ/E r_1 will be greater than u_{rms} and hence, will determine χ_{min}. Table III lists values of r_1 and u_{rms} for GaAs.

2.23.2 Calculation of Channeling Dips

The preceeding discussion has highlighted the theoretical foundation for understanding the channeling phenomenon. However, calculation of the yield versus beam/axis angle from first principles of the theory to accurately predict the observed shape of the channeling dip in closed form is formidable at best. Therefore, Monte Carlo computer simulations, pioneered by Barrett [BJ 71], of ion scattering in crystals gives the best predictions of the observed angular yield scans about an axis. The results of these simulations have been put into convenient equations that require no sophisticated computations.

The computer simulations are the sum total of many binary scattering events influencing the trajectories of the individual ions of a beam. Figure 37 depicts such a sequence of events. The atom positions in the lattice are chosen at random from a Gaussian distribution of the random displacement of the atoms from their equilibrium sites as a result of thermal vibrations. The thermal displacement is calculated from Debeye theory and is of the form of Eqs. 40 and 44. The motion of the projectiles through the crystal is treated classically, as provided by the theory of the Continuum Model. The starting point of the ion trajectories at the crystal surface are chosen at random. Finally, the interaction between the ion and the potential of the atom rows is modeled using Molieres'

approximation to the Thomas-Fermi function as in Eq. 49.

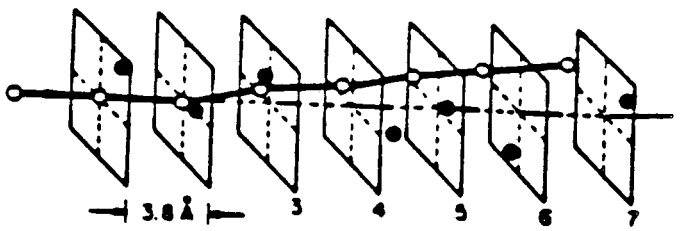

Fig. 37. Monte Carlo computer simulation of the sequence of binary events involved in the channeling process. Open circles represent the incident ion, darkened circles are the lattice atoms. Dotted lines show the extent of thermal vibration amplitude for the lattice atoms. (FMP 82).

The Monte Carlo simulation predicts the correct shape of the experimentally measure channeling dip (Fig. 38). Figure 39 shows the predicted intensity of the shoulder of the curve as a function of depth in the crystal. Anderson [AJ 67] has applied numerical integration to the probability distribution equations of the model to predict the shape of the channeling dips (Fig. 40). Also, Anderson calculated the shape of the shoulder as a function of crystal temeprature. Figure 41 shows this result. The broadening of the shoulder with increase in temperature is a result of increased ampitude of thermal vibration of the crystal atoms.

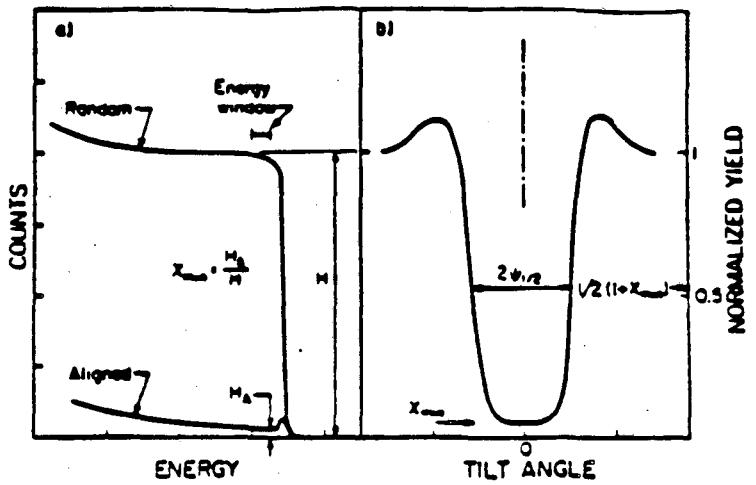

Fig. 38. Random and channeled backscattering spectra and the associated angular dip curve. Dip curve shows the characteristic shape and the definitions of the critical half-angle, 1/2, and minimum yield, min. (AF 77).

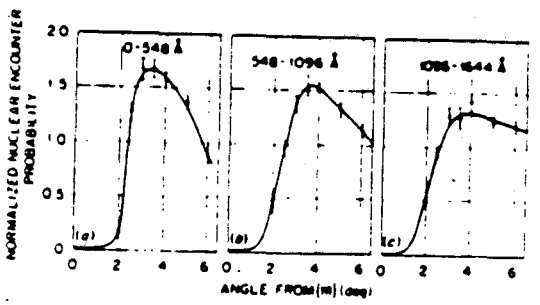

Fig. 39. Monte Carlo simulation result showing the depth dependence of dip curve shoulder width for 400 keV protons on <111> W. Crystal temperature is 298 K. (BJ 73).

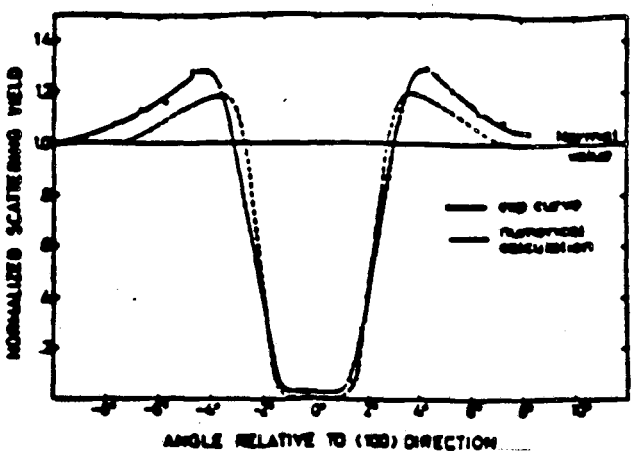

Fig. 40. Comparison of experimental and numerical integration results by Anderson for the calculation of the shape of channeling dips. 480 keV protons on <100> W at 309 K. (GD 74).

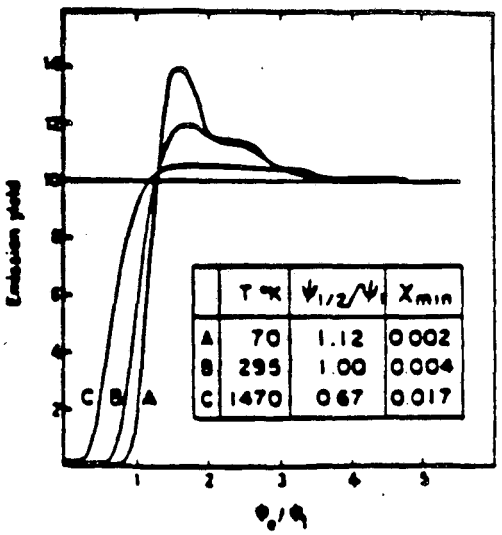

Fig. 41 Calculation of the width of the dip curve shoulder as a function of crystal temperature by Anderson showing increase in width from the increase in the amplitude of thermal vibration. (GD 74).

The axial half-angle is a measure of the maximum angle between the crystal axis and projectile beam that will allow the incident particles to remain channeled and as such is the width of the channeling dip. As the angle between the projectile beam and the channel axis is increased from zero (beam and crystal axis aligned), a greater fraction of incident particles posses enough transverse energy to penetrate inside the Thomas-Fermi screening distance of the atoms of the crystal channel, experience large angle scattering, and contribute to the backscattered yield. The axial half angle is measured at the point where the backscattered yield is halfway between random and minimum (aligned) yields (Fig. 38). Beam/axis angles greater than the axial half-angle will result in the dechanneling of projectile ions, an increase in backscattered yield to random yield values, and a loss of channeling behavior. In his simulation, Barrett considered the effect of the thermal vibration amplitude on the axial half-angle and arrived at an expression that provides good agreement between predicted and experimentally measured results. For light projectile ions or heavy ions of very high energy the expression for the angular half-angle is:

$$\Psi_{1/2} = 0.8\, F_{RS}(\xi)\Psi_1 \,, \tag{61}$$

where $F_{RS}(\xi)$ is the square root of adimensional string potential as predicted by Molier's screening function, ξ is $1.2u_1/a$, and Ψ_1 is given by:

$$\psi_1 = 0.307(z\ Z\ /Ed)^{1/2} \quad \text{(degrees)}, \tag{62}$$

where z and Z are the atomic numbers of the projectile and the target atoms, respectively, E is the projectile energy, and d is the atomic spacing along the axial direction in angstroms. Values for $F_{RS}(\xi)$ and ξ are found in Fig. 42.

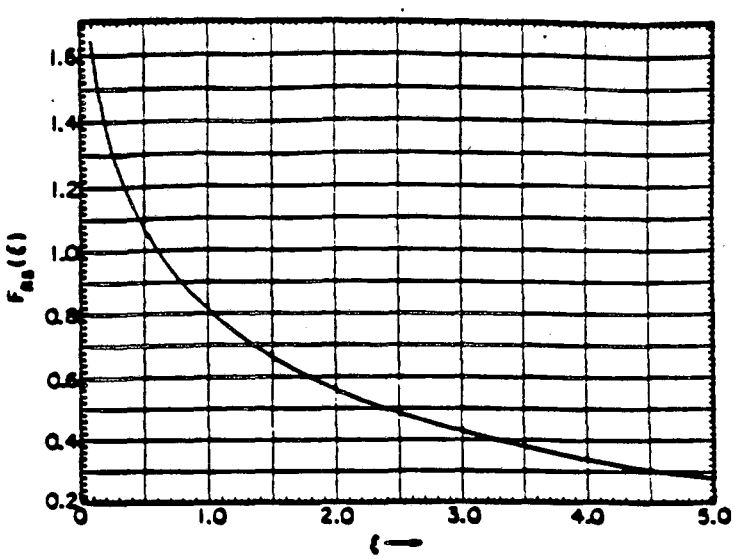

Fig. 42. Square root of adimensional string potential using Moliere's screening function. (AF 77).

The minimum yield is experimentally determined as shown in Fig. 38. The expression derived by Lindhard for the minimum yield (Eq. 59) is subject to the limitations of the validity of the Continuum Model as described in Eqs. 57 and 58. Predicted minimum

yields are below experimental yields. Therefore, Barret [BJ 71], using Gaussian approximations to the distribution of the beam directions to simulate experimental situations and fitting the results of his calculations, arrived at an expression which better predicts experimental yields:

$$\chi_{min} = 18.8\ Ndu_1^{\ 2}(1 + \eta^{-2})^{1/2}, \tag{61}$$

where $\eta = 126u_1/\psi_{1/2}$ with $\psi_{1/2}$ in degrees. At high energy when $\psi_{1/2} << u_1/d$ Eq. 61 can be reduced to:

$$\chi_{min} = 18.8Ndu_1^{\ 2}, \tag{62}$$

2.23.3 Distribution of Channeled Particles

The computer simulations have also been applied to describe the particle distributions within the channel [BJ 71]. The quantity of interest is the wavelength of the particle trajectory that gives rise to the periodic variation in the spatial density of the particle flux within the channel. This phenomenon is the basis of the description of channeling and its' applications.

A charged particle in a channel is confined by equipotential contours. As the ions penetrating the crystal proceed beyond the depth of the shadow cone they undergo a correlated sequence of scattering events. This is illustrated schematically in Fig. 43. The oscillatory motion of the projectile trajectories is damped with depth as a result of the mixing of and the irregularities introduced by the

vibrating atoms to the them.

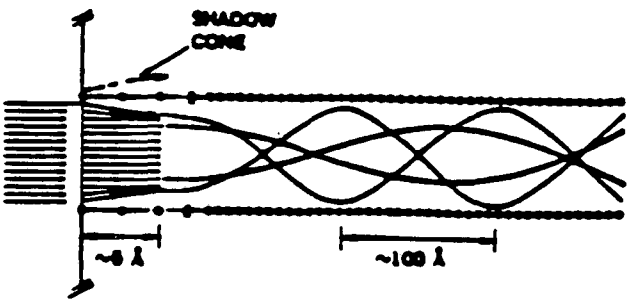

Fig. 43. Schematic of projectile trajectory assumed after the depth of the shadow cone. (FMP 82).

The wavelength of projectile trajectories is on the order of a few to several hundred angstroms and represents the fluctuation in the close-encounter probability with depth. Deep inside the bulk crystal (~10's of μm for axial channeling [BJ 71]) this probability distribution relaxes toward the random value as an approximately exponential function of depth. Strong oscillatory behavoir occurs only in the first 1000-2000 Å . Results of simulations of trajectories are shown in Fig. 44. Planar channels show a smoother damped oscillatory motion through the crystal than axial channels since motion transverse to the channel is one dimensional in the planar case and two dimensional in axial channeling.

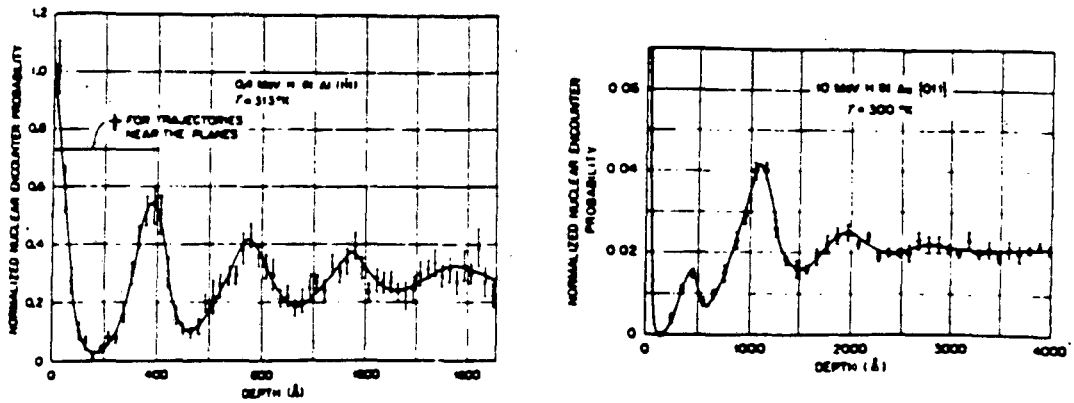

Fig. 44. Close-encounter probability as a function of depth as calculated by Barrett's Monte Carlo simulation for a) planar and b) axial channeling. (BJ 73).

Knowledge of the spatial distribution of particles within the channel is important when applying channeling to finding the location of impurities within the crystal. Fig. 45 shows the equipotential contours of <110> silicon.

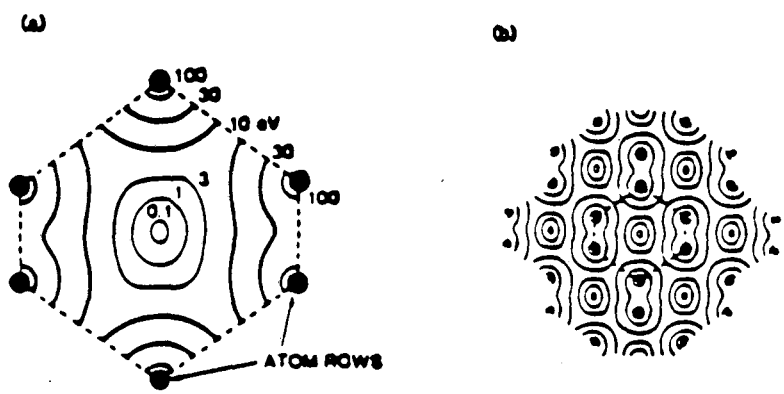

Fig. 45. a) Equipotential contours of the axial continuum potential for He on <110> Si. b) Contours for an array of channels. (FMP 82).

The values of the equipotential contours indicate the areas which a particle with less than that value of transverse energy will be confined. Note that at low transverse energies a particle will be confined by the rows of a given channel while at higher transverse energies the particle is free to move between channels formed by a set of rows (Fig. 45b). The probability of finding a particle of transverse energy at a point r is given by [FMP 82]:

$$P(E_T,r) = \begin{cases} \frac{1}{A(E_T)}, & E_T \geq U_{TOT}(r) \\ 0 & E_T < U_{TOT}(r) \end{cases}, \qquad (63)$$

where $A(E_T)$ is the area bounded by an equipotential contour, and U_{TOT} defines a contour. Using this equation it is possible to define accessible areas of the channel and to determine the flux distribution. These areas are defined by the equipotential contours, E_T is determined by the position r from a row with which a particle entered the channel; for incidence parallel to a row $E_T = U(r_{in})$. The spatial flux distribution, schematically shown in Fig. 46, is the sum of all particles in the channel. Thus, integrating the particle flux over the area of the channel yields [GD 74]:

$$F(r) = \ln\frac{A_T}{A_1(r)}, \qquad (64)$$

where A_T is the total area of the channel and $A_1(r)$ is the area bounded by a contour. This predicts flux peaking in the center of the channel as shown in Fig. 46.

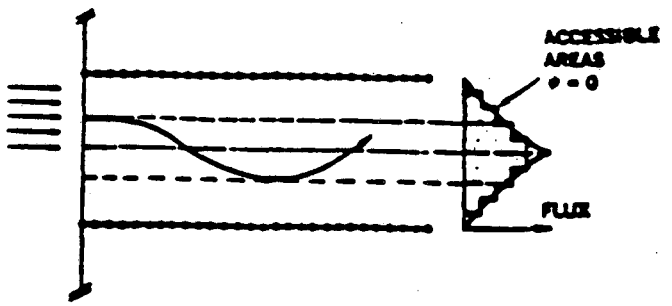

Fig. 46. Schematic showing origin of central flux peak as a result of Fig. 45 equipotentials for channeled particles. (FMP 82).

Thus, an interstitial impurity will display a higher yield in the channeled condition than in a random orientation (Fig. 47). The flux distribution at r close to the atomic rows is useful in estimating the scattering from substitutional impurities. A more realistic description of the flux distribution accounts for the angular divergence of the beam. E_T then is as defined in Eq. 54. The effect is an increase in the population of the higher energy contours and a broadening of the flux distribution in the channel [FMP 82].

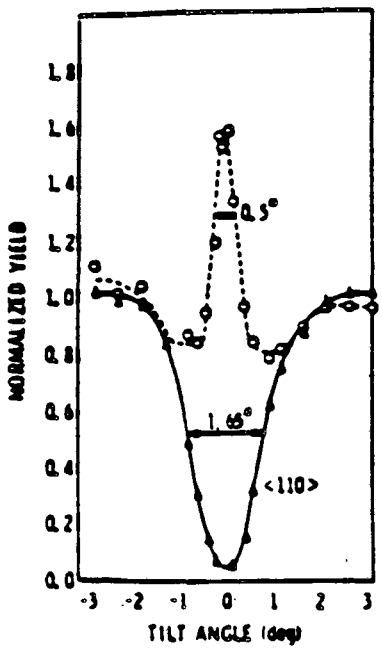

Fig. 47. Dip curve showing effect of flux peaking of Fig. 46 on the yield of interstitial (open circles) and substitutional (darkened triangles) impurities in a host (solid line) crystal. (FMP 82).

2.24 Monitoring Channeling with X-Rays

The question of the feasibility of channeling using the ion-induced characteristic x-rays of host and foreign atoms of a crystal can be resolved by consideration of the impact parameters involved. In order to channel using ion-induced x-rays, the impact parameter for vacancy production must be less than the ratio of u_{rms}/R_M where u_{rms} is the two dimensional rms vibrational amplitude (Eqs. 40 and 44) and R_M is the screened shadow cone radius (Eq. 49 and Fig. 43). The impact parameters involved in Rutherford scattering are typically of the order of $\sim 10^{-13}$ to $\sim 10^{-11}$ cm while

those for characteristic x-ray production are of the order of $\sim 10^{-11}$ to $\sim 10^{-9}$ cm. It is then possible that the impact parameter for x-ray production will be on the order of the minimum distance of approach to the channel walls, r_{min}, which, in most cases, is well approximated by u_{rms}. Therefore, whether a particular crystal/impurity system demonstrates the channeling phenomenon or not depends on the charge and mass of the projectile and target atoms and the temperature of the crystal.

Accurate knowledge of the impact parameter for x-ray production for the shell of interest is required to predict the x-ray channeling behavior of a projectile/crystal system. Based on Bohr's adiabacity criterion, Gemmell has provided a simple expression to predict the maximum impact parameter that will create a shell vacancy [GD 74]:

$$b_{max} = \frac{hv}{\Delta E} \ \mathring{A}, \tag{65}$$

where v is the particle velocity and ΔE is the binding energy of the shell of interest. If b_{max} is much less than r_{min} the x-ray angular scan should show the same variation of yield as the backscattered particle yield. If, however, b_{max} is on the order of r_{min} the expected channeling dip would be shallower and narrower than the RBS dip curve, or perhaps non-existant. Several workers [PST 69, BF 75, PP 78, AJ 81, BP 82, BP 83, PB 83, HT 86] have shown that light ion channeling in III-V compounds using characteristic x-rays results in an x-ray dip curve that follows the RBS dip curve quite well.

It is important when analyzing PIXE/RBS channeling spectra to understand the relationship between the two dip curves. The condition for channeling with ion-induced x-rays has been established in the preceeding discussion . With vacancy production impact parameters much less than r_{min} (for K-shells b ~0.005 - 0.010 Å), a projectile must penetrate well inside the Thomas-Fermi screening distance (both r_{min} and a are on the order of ~0.1 Å) in order to cause x-ray production. These particles are from the dechanneled component of the beam and, as such, experience backscattering. Therefore, the x-ray yield curve relates to the backscattered yield curve via the dechanneled fraction of the beam. Again, this assumption is only valid for $b_{max} << r_{min}$. Eq. 10 for the x-ray yield will then be modified under channeling conditions to:

$$N_i = I_0 \rho_i \frac{\Omega}{4\pi} \epsilon_i \prod_{j=1}^{n} a_{j_i} \omega_i \sum_{x}^{d} \sigma_i(E(x))\lambda(x)e^{-\alpha x}dx, \quad (66)$$

where $\lambda(x)$ is the dechanneled beam fraction as a function of depth, x, and all other terms are as previously defined. Note the limits on the integral. When analyzing RBS and PIXE spectra over a specific depth interval the yield of the dechanneled beam must be from the same depth from which the x-rays originated. Since x-ray spectra represent the integrated yield over the range of the projectile it is not possible to directly measure the x-ray production over a depth interval but only to infer it from the dechanneled fraction of the beam. An effect of this is that χ_{min} for an x-ray dip curve will not be as low as a RBS dip curve for which χ_{min} was determined over a small interval just beneath the surface peak.

Experimental aspects of x-ray channeling include the choice of projectile and energy. In PIXE studies of III-V semiconductors which have been doped with impurities of Z~14-16 K-α x-rays are used and, being of low energy compared to matrix absorption characteristics, are strongly absorbed. Therefore, x-ray yield must be as high as possible. K-shell electrons can be considered, for practical purposes, to be at (or near) the position of the nucleus requiring close penetration by the projectile. From a qualitative point of view, for a given particle velocity protons will penetrate closer to the nucleus than helium ions and thereby excite more K- x-rays. Furthermore, based on the BEA model, the production cross section for protons will be about 30 times greater than that for alpha particles at the same velocity. The production cross section for α-particles can be increased by increasing projectile energy but high energy helium ions have background production characteristics which make this an unacceptable alternative. Therefore, protons of as low of energy for the depth and impurities of interest are the best choice.

2.25 Lattice Location of Impurities

2.25.1 General

It is of importance in semiconductor studies to be able to evaluate lattice disorder, the epitaxial nature of thin films, and the lattice location of dopants and impurities after crystal growth and implantation processes. The channeling technique, whether by backscattered particles or by x-rays, is well suited to perform these studies.

Based on the prior discussion of the nature of the variation of the potential between atomic rows and the corresponding flux distribution within the channel, it is readily seen how the channeling technique is used to determine the preferred site of foreign atoms in a host crystal. With reference to Figs. 45 and 46, most particles are confined to the center of the channel and do not contribute to the backscattered yield. Those with enough transverse energy to penetrate inside the Thomas-Fermi screening distance are backscattered off of the atoms of the row. Therefore, foreign atoms on substitutional sites will display a RBS or PIXE spectrum as those of the host atoms. Contrarily, those atoms occupying interstitial sites will experience an increase in flux over the random orientation and will show in the dip curve a yield higher than random at a position corresponding to its' distance into the channel. By triangulation (ie., by directing the analyzing beam along the <100>, <110>, and <111> directions) the specific interstitial site can be determined. This process is shown schematically in Fig. 25 for one direction, the resulting dip curve in Fig. 47.

2.25.2 Determination of Specific Sublattice Site

In a diatomic crystal such as a III-V semiconductor, a dopant or impurity atom may or may not show a preference for one particular sublattice site over the other. If a preferred site exists, it plays an important role in determining the electrical properties of the crystal, ie., if the crystal is n- or p-type. Particle technique confirmation of Hall Effect or other methods of determining carrier

type is important as the preferred site may or may not depend on concentration or crystal growth or implantation processes. That is to say, at low concentration the dopant may prefer one site but at a certain level may begin to occupy the other, thus influencing the electrical properties, or in the case of intended isovalent doping, the dislocation density of the crystal. Therefore, a technique which can be used to observe sublattice site preference has been developed.

Research groups have shown [BF 75, AJ 81, BP 83, HT 86] that it is possible to determine the specific sublattice site of a foreign element in a diatomic crystal which posseses the ZnS structure. In order for this technique to be applicable, the crystal must posses strings of atoms of one type with unequal spacing between the strings in a direction normal to the beam. The <100> direction has mono-atomic strings but they are of equal spacing. The <110> direction meets the above criteria. With reference to Fig. 48, a beam incident along the $[\bar{1}\bar{1}0]$ direction will dechannel off of each of the two types of atoms with equal regularity. However, if the crystal is tilted in the $(1\bar{1}0)$ plane, first toward the [111] then toward the $[\bar{1}\bar{1}\bar{1}]$ directions, one mono-atomic string will shadow the other depending on the incidence. This is shown as $+\theta$ and $-\theta$ in the figure. The effect on the dip curve will be that the shoulder regions will show an asymmetry in the x-ray yield for each element of the compound. For incidence $+\theta$ the x-ray yield for the atoms in the row that are being shadowed will be less than for the opposite incidence, $-\theta$. The asymmetry in the yield is reversed for the other atom of the compound at the same incidences ie., for $+\theta$ the As K-α yield will be higher than the Ga K-α yield while for $-\theta$ the Ga K-α yield will exceed

that of the As K-α (Fig. 48).

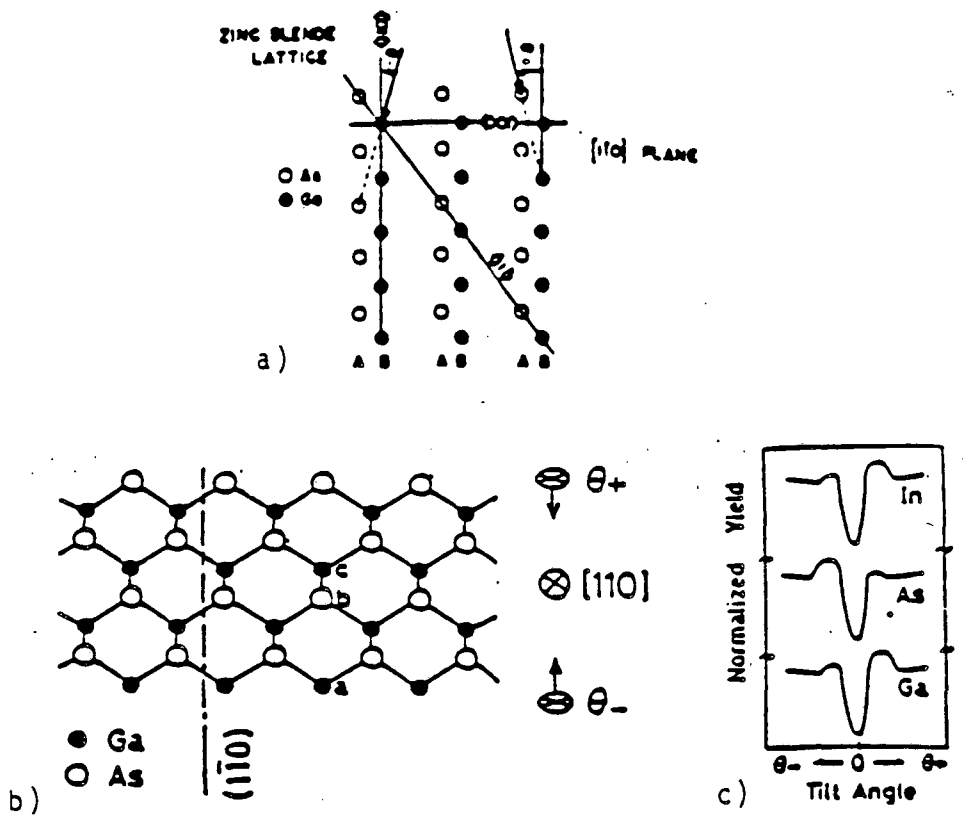

Fig. 48. a) Arrangement of atoms in the (1$\bar{1}$0) plane of GaAs showing shadowing of mono-atomic strings for incidences of + and -θ. (BP 83). b) Same atom distribution as in (a) but normal to the beam showing unequal distances $\overline{ab}$ and $\overline{bc}$. (HT 86). c) Representation of dip curves for the case where In occupies the Ga sub-lattice site. (HT 86).

An impurity occupying a preferred site will posses the same asymmetry in the x-ray yield with angular variation as the yield from the atoms of the host site. This is illustrated schematically in Fig. 48c.

The experimentalist is actually able to preferentially impart a greater fraction of the beam with an increase in transverse energy in a specific direction. Thus, a higher fraction of the total dechanneled beam will dechannel off of a specific mono-atomic string, yielding the asymmetry of the channeling dip. This asymmetry effect is expected to occur only for x-rays generated in the first ~1000 Å because, as a result of mixing of trajectories, the ions lose the initial conditions [HT 86] (ie., statistical equilibrium of the channeling beam is established [BP 83]). Therefore, when the integrated yield of x-rays of the matrix is considered, the asymmetry effect will be small. It is possible, however, that for foreign atoms implanted near the surface or in cases where dopant x-ray absorption is significant (leading to a "effective" surface layer) that the asymmetry effect for the dopant will be much more pronounced as only a small fraction of the beam will be dechanneling in random directions in the depth interval of significance.

By employing this technique, researchers have studied the site preference for several elements introduced to GaAs by growth and implantation techniques. It has been shown, for example, that in LEC grown GaAs:In that In occupies the Ga sublattice site until a concentration of ~7E19 atoms/cm^3 is reached when In begins to assume As sites [HT 86]. Also, under the implant and annealing conditions specified in the reference, S implanted into GaAs shows a preference for the As site while no asymmetry effect was observed for implanted Si [BP 83].

As with any technique, there are advantages and disadvantages associated with this method. Since an entire axial scan is required

to observe this effect, ultra-precise axial orientation as a beginning point is not absolutely required. This is advantageous as this condition is not easily obtained. However, insofar as an entire axial scan is required, the time to conduct the experiment, particularly at low beam currents necessary to minimize damage, is quite long. A complete scan usually takes several hours to accomplish AFTER the desired channel is located. The sample can be moved so as not to disrupt the orientation to maintain a fresh surface and reduce damage which will spoil the asymmetry effect. Lowering of projectile energy to minimize x-rays from deep within the sample (hence, increasing the observed asymmetry effect) may be applicable in some situations.

It occurred to the author that it is interesting to consider the possibility that, based on the results of the theoretical treatment of channeling given, there may be a similar asymmetry effect that can be observed in ZnS crystals. Owing to the lack of inversion symmetry and the diatomic nature of such structures, a particle incident along [111] encounters the atomic planes in an order opposite to when the incidence is $[\bar{1}\bar{1}\bar{1}]$ (note Fig. 48). A question raised during the course of this study concerned the effect of the order in which the atomic species are encountered by the projectile on the energy of backscattered particles and on the x-ray yields from each of the atoms of the compound. One wonders if the order in which the atomic species are encountered will cause a difference which manifests itself as a noticable change in either the energy of the backscattered particles and/or the characteristic x-ray yields for opposite incidences. If such an asymmetry is observed, it may or may not be applicable to the determination of the preferred sublattice site.

Evaluation of this situation requires consideration of the spacing of atoms along <111> directions. In diamond and diamond-type structures there are two distances which seperate the atoms along <111>. The greater distance is three times the smaller distance. Hence, two atoms seperated by the smaller distance can be thought of as a set with each set being seperated by three times the intra-set distance, or, the inter-set distance is three times the intra-set distance. When a compound of atoms A and B which crystallizes in the ZnS structure is aligned along [111], each atom B of a set is shielded by a corresponding atom A. For incidence $[\bar{1}\bar{1}\bar{1}]$ the shielding situation is reversed. In GaAs the intra-set distance between an As atom and a Ga atom is 2.448 Å, the inter-set distance is then 7.345 Å. This situation for incidences of [111] and $[\bar{1}\bar{1}\bar{1}]$ can be seen in Fig. 48a. Therefore, a beam of particles aligned along <111> may preferentially interact with the lead atoms of the set yielding a type of orientational asymmetry effect.

One would expect that, in light of the formation of the shadow cone, the energy of the backscattered particles off of the surface will be characteristic of the mass of the atom of the lead plane, thus contributing to an asymmetry in the surface peaks of the RBS spectra for the two orientations. Effects in the bulk of the crystal, however, are not so clear-cut. Since the spacing between the atoms varies, there will be a value of the continuum potential (from the model by Lindhard) for each spacing which will serve as to provide the particles with two initial trajectories leading to enhanced mixing. Any difference in behavior, then, will only be observable in the region <1000 Å as with the prior technique. Because of the enhanced

trajectory mixing, it may even be as much as 1/2 to 1/3 the depth as the standard method. The specific potentials and expected flux distributions must be analyzed for a crystal before predictions can be made.

Study of the relevant crystal parameters which influence channeling in <111> GaAs may provide insight into any observable orientation-dependent effects and will serve to enhance the understanding of the channeling phenomenon. A check of the ratio of u_{rms}/R_M for Ga and As (Eqs. 39, 40, 43, 44) over the distance between the atoms of a set verifies that the radius of the shadow cone (~0.1 Å) is indeed much greater than the impact parameter (Eq. 65) for K- x-ray production (~0.01 Å) so that the atoms of the row will be shielded by the surface atom and the channeling phenomenon will indeed take place. Therefore, incident projectiles with a transverse energy too great to be channeled will be backscattered off of the surface atoms with an energy characteristic of the collision (Eq. 4). It is expected, then, that the energy of the backscattered particles from orientation $[\bar{1}\bar{1}\bar{1}]$ to be characteristic of, say, Ga and as such the surface peak will be displaced to the lower energy channels of the RBS spectrum relative to the As surface peak from orientation [111]. Based on the mass resolution (Fig. 7) of protons on mid-Z elements it is expected that higher energy, heavier ions must be employed to observe this difference.

An asymmetry effect arising from the ions in the bulk depends on the nature of the continuum potential, the beam flux distribution, and the trajectories of the projectiles within the channel. Applying the equation for the continuum potential for a vibrating row of atoms

listed in the Appendix of reference [BJ 71]:

$$V_{rv}(0) = \frac{2zZe^2}{d} \sum_i \frac{1}{2}\alpha_i e^{\nu_i} \; E_1(\nu_i), \tag{67}$$

gives the potential between atoms of a set (intra-set) as ~370 eV and between sets (inter-set) as ~120 eV. In the equation i ranges from 1 to 3, α_i=(0.1, 0.55, 0.35), β_i=(6.0, 1.2, 0.3), $\nu_i = 1/2\beta_i^2\mu^2$, $\mu = u_1/a$, and $E_1(\nu_i)$ is the exponetial integral given by:

$$E_1(x) = \int_x^\infty y^{-1} e^{-y} dy, \tag{68}$$

and is solved using an expression from standard mathematical tables:

$$\int_x^\infty \frac{e^{-y}}{y} dy = -\gamma - \ln x + \int_0^x \frac{1 - e^{-u}}{u} du, \tag{69}$$

where γ is the standard constant equal to ~0.5772156649. This expression is expected to give good results when x is small. Since there are two values of the continuum potential that may be encountered by the channeled projectiles, there are two initial trajectories (trajectories assumed after the shadow cone) that may be assumed. For projectiles entering the channel near the channel wall and encountering the ~370 eV potential, this amount of potential energy is converted into kinetic energy (conservation of transverse energy, E_T) causing the projectile to scatter with a trajectory that makes an angle of 1.10° with the row. Given the geometry of the <111>

channel in GaAs, the projectile will then travel a distance of ~125 Å before encountering the potential wall on the other side of the channel. The wavelength of the particle trajectory is therefore ~250 Å. Likewise, a particle encountering the ~120 eV potential wall will be scattered with a trajectory that makes an angle of ~0.628° with the row and will travel ~220 Å before experiencing scattering from the other side of the channel giving an overall trajectory wavelength of ~440 Å. Since, in one dimension, there is three times as much distance along the <111> channel with a continuum potential of ~120 eV, it would be expected that, all things being equal, that three times as many projectiles will have a trajectory wavelength of ~440 Å. A plot of close-encounter probability as shown in Fig. 44 will then consist of two waves of wavelength and amplitude characteristic of the trajectories involved damping to a statistical average value at a depth of ~1000 - ~2000 Å. Since the ~370 eV and ~120 eV projectiles penetrate the row to a distance from the center of ~0.280 Å and ~0.430 Å, respectively, they do not contribute to the yield of either the backscattered particles or the x-rays and as such are not responsible for orientational dependent effects (Fig 49).

Fig. 45 shows the equipotentials encountered by helium ions incident on <110> Si. Fig. 50 shows a similar situation for protons incident upon <111> GaAs. The potentials were calculated using Eq. 51 considering nearest-neighbors only and as such is intended only to be a guide for illustrative purposes. The figure is for an As plane. A Ga plane would have values, particularly far away from the ion cores, differing only by a few eV. The 20 eV points alternating with the 5 eV regions are a result of the ABCABC stacking sequence and

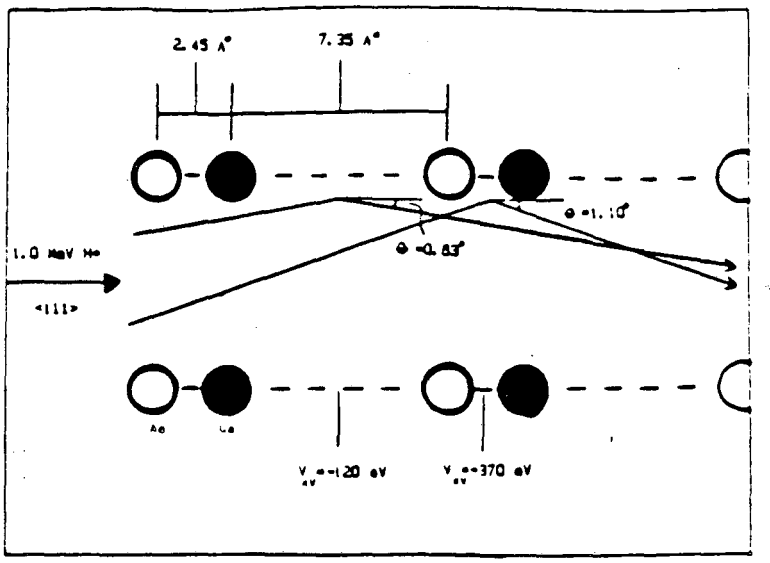

Fig. 49. Schematic of the two projectile trajectories assumed in <111> GaAs as a result of unequal atom spacing along the row which alters the continuum potential. Shows the mixing of the trajectories.

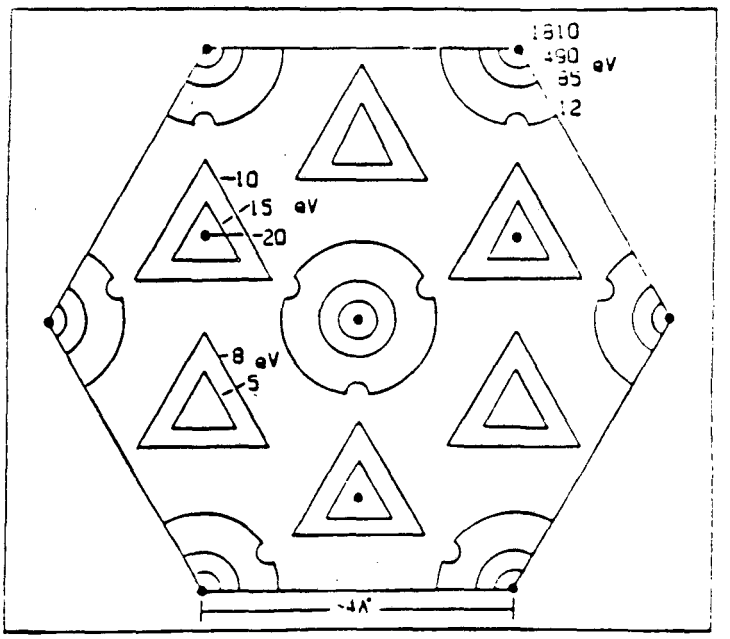

Fig. 50. Equipotential contours for (111) As plane of GaAs for H+ projectiles. Calculated using nearest neighbors only.

inter-locking fcc lattice structure of the crystal. They arise from the presence of the nearby Ga plane. As previously described, particles with a value of E_T less than the energy of a contour will be confined to that contour along its' path. Therefore, based on the flux distribution discussed in the section on channeling theory, most particles will follow a path which is defined by the low energy (~8 and ~5 eV) contours. Particles with high values of E_T will oscillate over wider transverse dimensions, namely, the width of the channel. These particles have a greater probability of scattering off of a vibrating atom of the row and have the trajectory altered such that on its' next encounter with an atom (it must encounter an atom for that is the potential contour in which it is contained) it is able to penetrate to such a depth that it suffers scattering through a larger angle than the original one. The transverse energy, E_T, of the particle is increased, increasing the likelinood of further encounters with vibrating atoms. In this manner the trajectory of the particle is successively altered such that finally it posseses a value of E_T great enough for it to have an impact parameter on the order of those required for vacancy production or backscattering events (Fig. 51). A preference for finally dechanneling off of one atom or another, based on the geometry of the trajectories and the <111> rows of GaAs will determine if an orientational dependence will be observed.

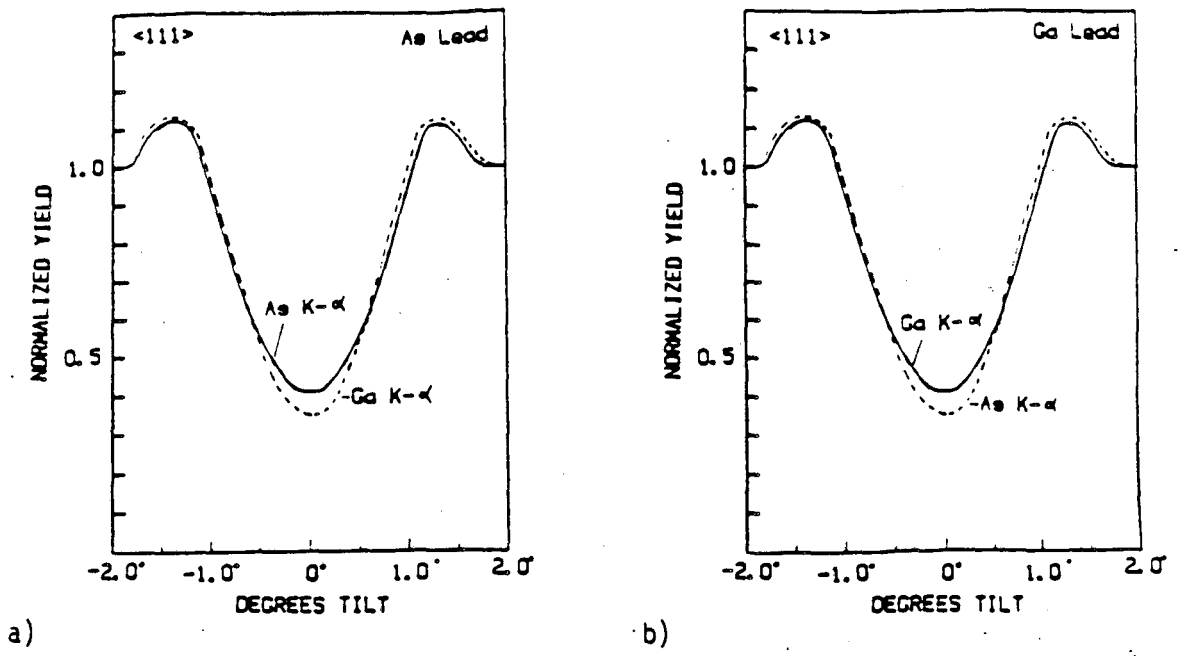

Fig. 51. Schematic of asymmetric dip curves for opposite incidence in 111 and 111 GaAs for a) As plane lead and b) Ga plane lead.

It is impossible from an isolated one projectile, two row model to predict a preference for the dechanneling of projectiles in aligned <111> GaAs. A Monte Carlo type computer simulation is required to sort out any statistical trends in a many bodied scattering sequence problem such as this. Therefore, it suffices to say that since the projectiles with high values of E_T are guided by the potentials of the atoms themselves, they may follow trajectories that cause a statistically significant number of them to preferentially interact with the lead atom of a set. In other words, the projectile is contained by contours of high potential energy, a condition that exists only near the atoms themselves. Therefore, the scattered projectile encounters the high potential of the leading atom before

the trailing atom and may, over the angles and distances of the problem, be scattered off of the leading atom. Again, only a many-bodied simulation of the Monte Carlo type could predict the statistical outcome of the problem. Any experimentally observed asymmetry effects are expected to be small.

In order for this technique to be useful in specific site determination experiments, the impact parameter for x-ray production of the foreign atom must be on the order of those of the host atoms. If this method did indeed show an orientational dependence of x-ray and/or backscattered particle yields, the resulting asymmetry would appear in the bottom of the axial dip curve about the 0° position (Fig. 51). Herein lies the major disadvantage of this technique; the beam and crystal axis must be very well aligned to 0°. From the point of view of the optics of the problem, since the projectiles emanate from a source at an infinite distance, for all practical purposes, from the target planes, a small degeree of mis-alignment will be sufficient to begin to expose the atoms of the row being blocked, particularly when the atoms posses similar ionization cross sections. Small increment angular scans about 0° using a high quality goniometer would insure the best alignment possible. Advantages of this technique include far less scan and data analysis times and less target damage.

TABLE III

GaAs CRYSTAL CHANNELING PARAMETERS

Atom	a, Å	Θ_D^*, K	u_{rms}^*, Å	$R_{M_{<111>}}$, Å	b_{max_K}, Å
Ga	0.134	300	0.112	0.930	0.0133
As	0.131	300	0.112	0.925	0.0116

*For the compound GaAs, [KC 76].

III. EXPERIMENTAL

3.0 Experimental Equipment

3.01 Scattering Chamber

A scattering chamber that is both versatile and efficient is required to perform PIXE/RBS experiments. The system should provide a homogenous beam of sufficient intensity, low background, tight tolerances on the beam/target/detector(s) geometry, adequate vacuum, and a goniometer on which the target is mounted for channeling studies. Providing flexibility to allow for various future configurations is also important. A chamber that met the above requirements was constructed and incorporated onto a beam line of the 2.5 MeV Van de Graaff accelerator at LBL.

The particular requirements for the scattering chamber needed for this study included the ability to perform routine PIXE and RBS studies, channeling experiments, and portability as the chamber would be used at the Van de Graaff accelerator and, on occasion, at the 88-in. cyclotron, also at LBL. The scattering chamber constructed is a compact unit consisting of a stainless steel shell with aluminum flanges and platter, or baseplate, on which collimators, detectors, electronics, etc., are mounted. A stainless steel receptacle for the x-ray detector was silver soldered in a hole in the chamber wall bored at 30° to the beam axis. This serves to place the detector as close as possible to the target without interfering with goniometer movement. A 2 mil Be window sealing a hole in the end of the receptacle separates the interior of the chamber from the external

atmosphere. This protects the 1 mil Be detector window from undergoing excursions from atmospheric pressure to vacuum and back each time the chamber is opened and closed. The air gap between the chamber and detector Be windows is 3 mm which is insured by an insulating plastic ring inside the receptacle. Flange seals are conventional O-ring-in-groove as are the feedthroughs for electrical access located on the downstream beam-stop flange. A quartz window on which a thin layer of phosphorous has been evaporated is located on the beam-stop flange to facilitate alignment of the beam line when the chamber is moved. Spacers made from FR-4 [LLNL Spec. LED 21895] were machined with Varian gasket detail [VAC 2099] and placed between the chamber and the beam line, pump, etc. to provide electrical insulation. In keeping with the compact design requirement, the goniometer mounting hole was bored off the cylindrical axis of the chamber to provide more space on the baseplate for detector, collimator, filter, etc. placement. Current integration is carried out on the target itself and, as such, the goniometer is also insulated from the chamber.

As much flexibility as possible with a compact chamber was provided for detector and collimator placement. Beam collimation inside the chamber is accomplished via an adjustable collimator holder that is attached directly to the beam line. Adjustment is provided by three adjusting screws which also serve to lock the collimator in place when the desired position is achieved. Collimator plates with various aperature sizes machined from tantalum stock can easily be changed without upsetting the alignment. Space for additional collimators in front of the target is available. This holder can be

removed and replaced by an annular surface barrier detector (for RBS studies) which has its' own collimator through the center. Sets of mounting holes radially spaced every 5 degrees about the target allow for flexibility in choosing the backscattering angle for RBS measurements using a standard detector with ample space for detector collimators. The RBS detector and collimator are mounted on sliding tracks with the option to cool the detector included. X-ray collimation is accomplished via the fitting of collimator plates into a recess in the end of the detector receptacle and securing them with a screw-down ring holder. Again, ample space between the target and the detector for other collimators, filters, etc. is provided. The x-ray collimator and holder is replaced by a solid cover with an O-ring seal to protect the chamber window from atmospheric pressure excursions when the chamber is being used for RBS experiments only. Electron suppression is facilitated by a suppression shield placed upstream of the target biased at -45 V. The shield is insulated by a lucite stand and is easily removable for target access.

The entire chamber assembly is secured to a lightweight, portable frame for ease of movement. The goniometer is mounted on the underside of the chamber and is completely contained within the frame. Adjustable feet take up the differences in beam line height that may be encountered. Mechanical rougning and diffusion pumps mounted on a portable carts provides the necessary vacuum. The chamber is attached to the Van de Graaff beam line via a flexible connection upstream of which, located in a valve body, is a collimator holder similar to the one in the chamber. This arrangement allows for easy change of the upstream collimator aperature size without

upsetting alignment. Figs. 52 a and b show the details of the arrangement. In the present configuration chamber vacuum ranges from 10^{-6} to 10^{-7} torr and beam divergence is $\leq 0.30^{\circ}$ with up to 45 nA of 1.5 MeV protons (spot size 1 mm) on target.

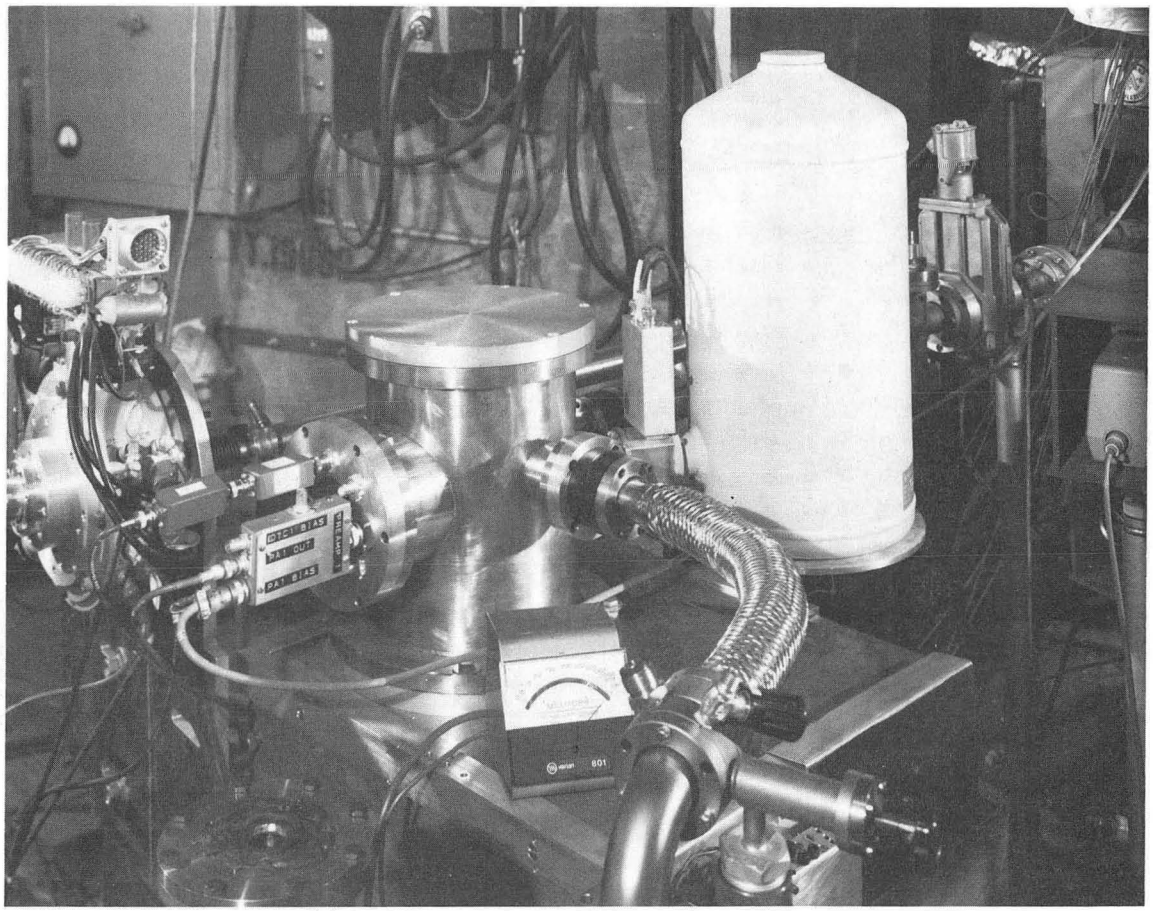

CBB 868-6111

Fig. 52. a) External view of PIXE/RBS sc attering chamber.

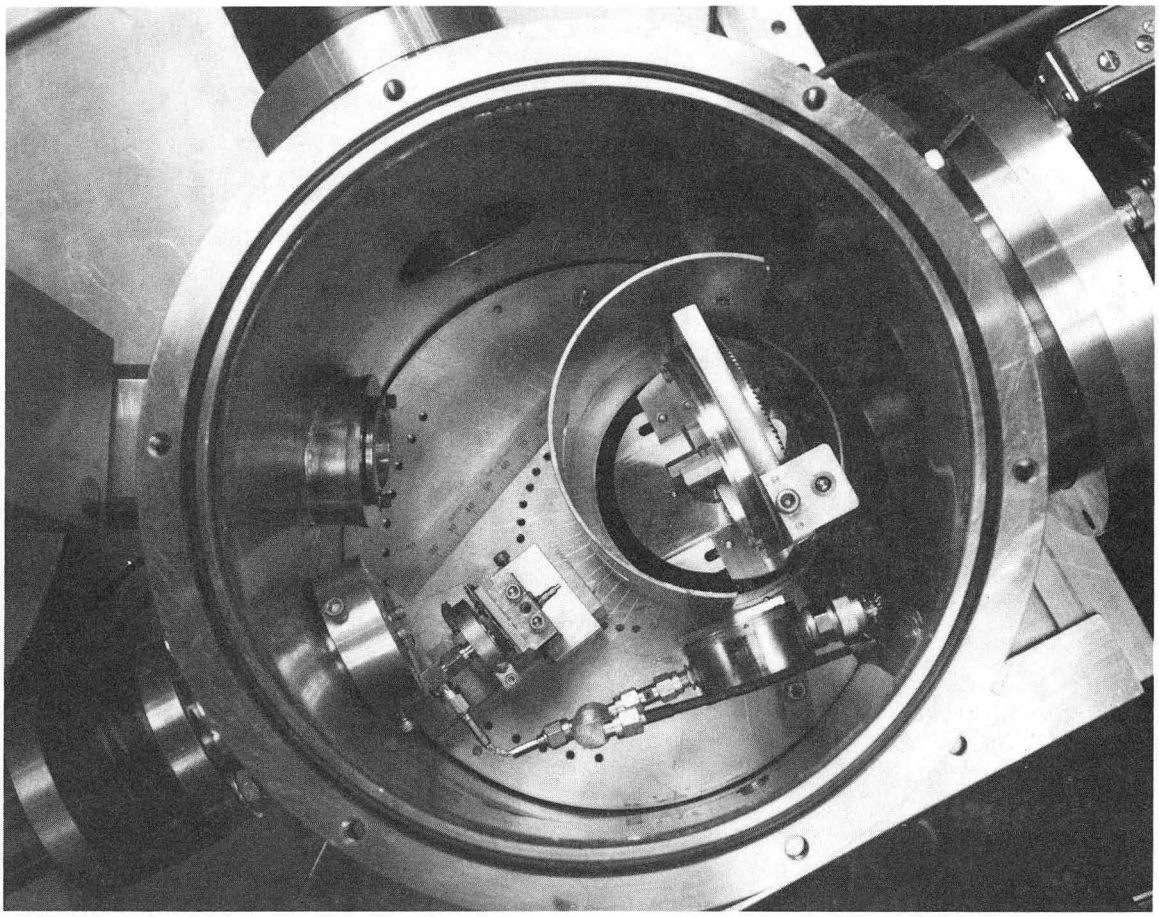

CBB 868-6113

Fig. 52. b) Close-up of internal arrangement of target goniometer, detectors, and electronics.

3.02 Detectors and Electronics

Both backscattered particle and x-ray detection can be accomplished with either gas filled proportional counters or solid state semiconductor detectors. For most cases the advantages of high counting rates and good energy resolution make semiconductor detectors the the detector of choice.

A solid state surface barrier detector for backscattered particles is a semiconductor diode of either the p-n or Schottky barrier type, operated in the reverse bias mode. Backscattered particles passing through the depletion region excite a number of electron-hole pairs which are separated by the electric field. The carriers are swept to their respective contacts by the electric field internal to the junction. The number of electron-hole pairs generated is proportional to the energy of the ionizing particle. Thus, the current generated by this process, or the charge collected on the contacts, is a measure of the energy of the particle which collides with the detector. The current pulses are amplified and sent to a pulse height analyzer (PHA), or multichannel analyzer (MCA), for sorting and then on to a computer for more sophisticated data analysis (Fig. 54).

Solid state surface barrier detectors are constructed from n- or p-type silicon with thin metal layers which serve as contacts evaporated onto the surfaces. A thin gold layer (~40 $\mu g/cm^2$) forms the front rectifying contact while a similar thickness of aluminum evaporated onto the rear forms the ohmic contact (Fig. 53). A Tennelec Model PD-100-100-16-139-1; CS was used in this project. The energy resolution of the detector is typically on the order of a few 10's of keV. Radiation induced damage limits the lifetime of these detectors as vacancy-interstitial complexes or other defects can act as carrier trapping sites which diminishes the energy resolution of the detector. Kin Man Yu [KMY 84] has evaluated detector degradation for both alpha- and heavy-ion (^{16}O) particles. Detector damage was found to be insignificant for 1.5 to 2.0 MeV ^{4}He ions while the lifetime (as defined by 40 reduction in energy resolution) when

20 MeV ^{16}O ions were used was about 50 hours of operation. A typical run time for a sample is about 10 minutes; since a tremendous amount of data can be collected in 50 hours, this is a minor disadvantage when compared to the advantages of using a detector of this type.

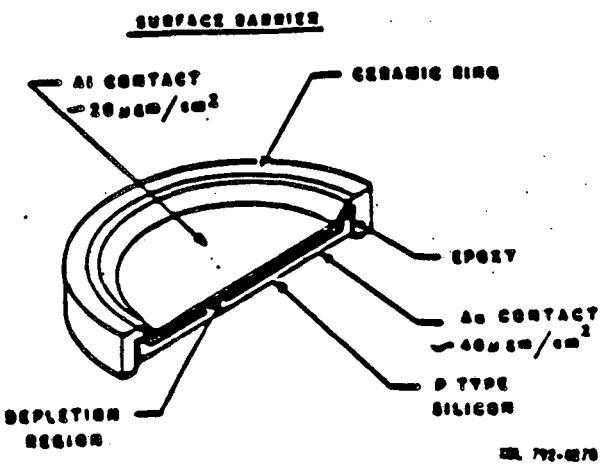

Fig. 53. Cut-away view of surface barrier detector. (Courtesy KMY 84).

X-ray detection can be accomplished with either a solid state detector or a Bragg spectrometer employing a proportional counter. Solid state detectors are known as energy-dispersive detectors while Bragg spectrometers (or x-ray crystal or grating spectromters) are wavelength-dispersive. Crystal spectrometers employ Bragg's Law to separate the x-rays to be detected by the well known rule:

$$n\lambda = 2d\sin\theta, \qquad (67)$$

where λ is the wavelength of the radiation, d is the spacing between the lattice planes of the crystal spectrometer, and θ is the angle between the incident radiation and the crystal planes. The crystal spectrometer is scanned through an angle corresponding to a particular region of interest or through all angles for which Bragg's rule will be satisfied for the particular system. This type of detector offers superior energy resolution (on the order of tens of eV) because, for a given planar spacing, the Bragg equation is satisfied for one wavelength for each angle θ. However, the internal efficiency of these detectors is quite low requiring an intense x-ray source for efficient data collection. Furthermore, the simultaneous detection of a wide range of x-ray energies from a sample is not possible as Bragg's rule is only satisfied for a given x-ray at a particular angle. Also, it is likely that it will not be possible to satisfy Bragg's rule for every impurity in a sample with a single choice of diffraction crystal necessitating changing crystals during an experiment. These types of detectors, then, are best suited for situations where a narrow, known range of x-ray energies is being studied, the element of interest is present in sufficiently high concentration to generate an intense source of x-rays, and the ultimate in energy resolution is required. Such studies include chemical state investigations of compounds.

Solid state detectors are the choice for most semiconductor studies. As surface barrier detectors, semiconductor detectors for x-ray detection are formed by application of a reverse bias across a p-n junction. Ionizing radiation creates electron-hole pairs which are separated by the electric field. The electrons and holes are

collected at their respective contacts with the resulting current pulse amplified and sent to the MCA. Such detectors possess high detection efficiency, accept x-rays from large solid angles, and therefore do not require high intensity sources. This is a great advantage when performing trace element analysis because the detectable concentration is ultimately limited by the intensity of the background. Therefore, for a given background intensity, these detectors are capable of detecting x-rays from impurities that are in lower concentration (resulting in a less intense source) than possible with the Bragg spectrometer employing a gas filled proportional counter. Furthermore, a wide range of x-ray energies can be detected simultaneously, making these detectors attractive for bulk semiconductor analysis.

Semiconductor detectors for x-ray detection are constructed of p-type silicon which has been carefully compensated with Li, donor [CF 75] to achieve intrinsic conducting behavior. In order to prevent Li redistribution and to reduce noise, these detectors and the associated FET of the first stage of the pre-amplifier are encased in an evacuated enclosure sealed by a thin (~1 mil) Be window. The leakage current arising from thermally generated carriers in the depletion region, at 77 K, is held to about 10^{-15} A [JG 73]. The detector itself is about 3-5 mm thick and 0.5-1 mm in diameter. Charge collection efficiency is increased and internal background is reduced by employing a guard-ring which defines the boundaries of the central detector via parallel electric field lines [JG 73]. The detector and first stage FET are followed by pulse shaping amplifiers which in turn are followed by instruments analogous to those used for

RBS studies with a surface barrier detector (Fig. 54).

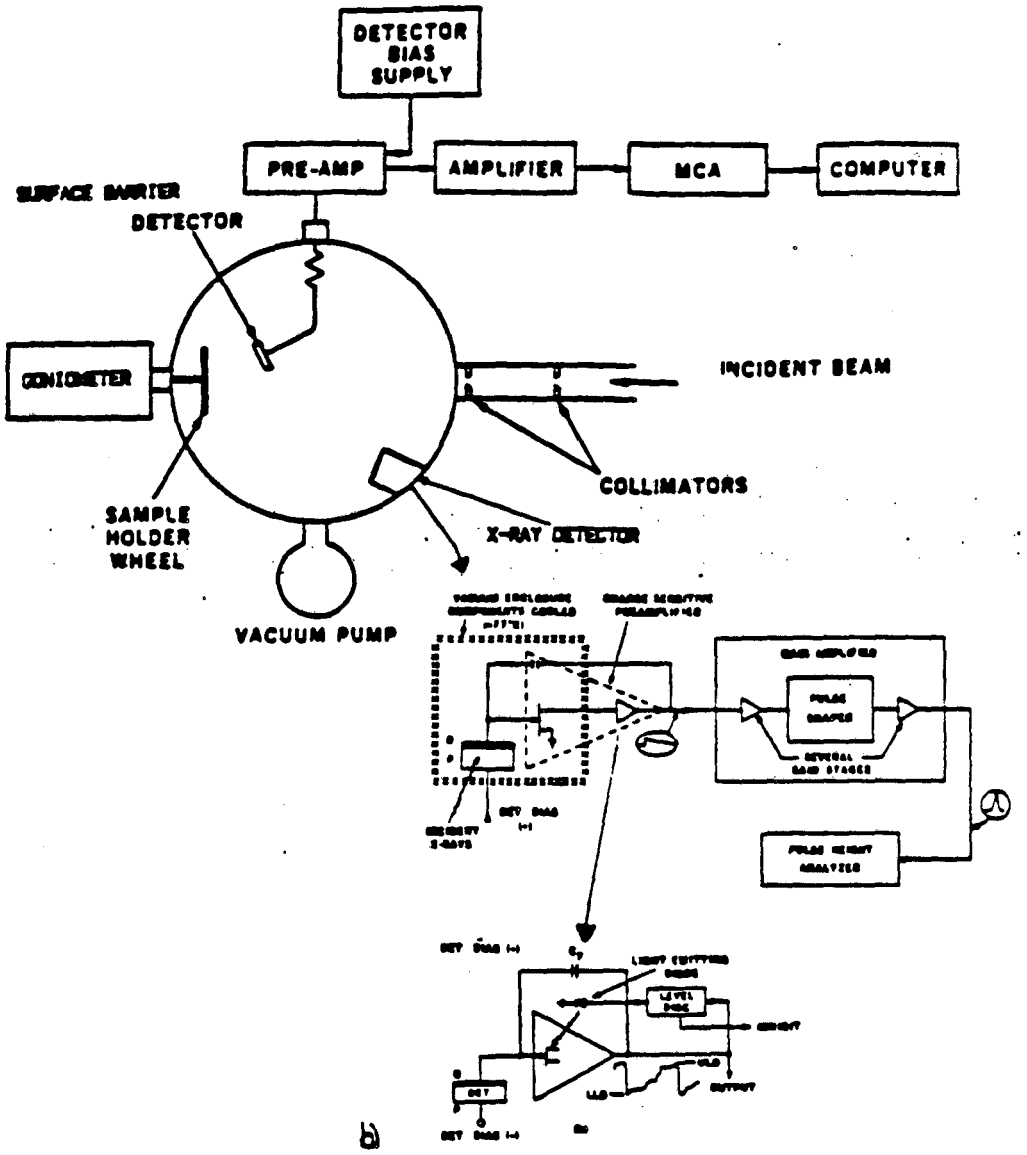

Fig. 54. Schematic of detector placement in the chamber, electronics, and details of the pulsed-light feedback circuit of the Si:Li x-ray detector. (Courtesy JG 73).

The detector system used in this study was a commercially available Kevex unit with an active area of 80 mm^2 and a depletion depth of 3 mm.

The energy resolution is limited by statistical fluctuations in the charge-production process within the detector and by electronic noise from fluctuations in leakage currents in the detector and in currents in the amplifiers. Below 5 keV electronic noise is the dominant source while at higher energies charge-production statistics dominate [JG 73]. The detector contribution to resolution is limited by charge production statistics:

$$\Delta E_{FWHM} = 2.35(FE\epsilon)^{1/2}, \tag{68}$$

where ΔE_{FWHM} is the contribution to the full width of a x-ray peak at half maximum resolution, E is the energy of the incoming photons, ϵ is the average energy required to produce an electron-hole pair, and F is the Fano factor which accounts for the statistics of energy loss of the photoelectron to the electron-hole pair production and to lattice vibrations. For silicon at 77 K F is ~0.12 and ϵ is ~3.8 eV. Electronic noise arising from Johnson noise in the FET channel and shot noise of the reverse current in the detector is processed together with the signal by the pulse shaping circuitry of the main amplifier. Typical energy resolution of a detector of this type is 150-180 eV.

An attractive feature of these detectors is the high counting rate performance. The counting rate is ultimately limited by the charge collection time. Usually, pulse procesing used to obtain optimum

signal to noise ratios limits the count rate of the detector. The pre-amplifier for modern detectors consists of an operational amplifier with an integrating pulsed-light feedback capacitor as shown in Fig. 54. Incoming current pulses from the detector are integrated by the feedback capacitor producing voltage steps at the output. When the output level reaches a value set by the output-level discriminator, the light-emitting diode is turned on. This LED is coupled to the drain-to-gate diode of the FET which produces a current into the gate circuit that discharges the capacitor. This results in more rapid capacitor discharge (reduced "reset" time) than a conventional charge-sensitive preamplifier employing a leakage resistor across the capacitor, low noise, and a detector system that is capable of higher counting rates. The pulse is then shaped by the shaping circuitry of the main amplifier. The pulse processing circuit only processes one pulse at a time before sending it to the PHA. A second pulse arriving before the preceeding pulse is completely processed by the circuit is rejected by the pile-up rejector. This pile-up is further reduced by shaping the incoming pulses to a Gaussian form. The symmetric shape about the center and narrow total width helps to reduce pile-up at nigh counting rates. As counting rates increase, the pile-up circuit rejects a greater fraction of the incoming pulses. The output rate, then, increases with input rate until a peak is reached where the output rate begins to fall off with increase in input rate [JG 73]. Knowledge of the pile-up characteristics of the detector system employed is important in PIXE analysis.

It is very important when performing analysis of PIXE spectra to account for the dead time of the detector and the electronics. Disregard of the dead time of the detector for the observed output rate will result in attempting to determine the concentration of elements in a matrix from fewer counts (lower x-ray intensity) than were actually produced. The dead time characteristics can be determined by placing a x-ray source in front of the x-ray detector at various distances and/or with various diameter collimators in place to achieve a wide range of counting rates and monitoring the input and output rates. A plot of the output rate vs the input rate gives the percentage of incoming pulses that were not processed because of pile-up and were therefore rejected.

$$I_o = fI_i , \tag{69}$$

where I_o is the output count rate, I_i the input count rate, and f is the proportionality factor between the two. This relationship is valid over the range in which the output rate increases linearly with input rate and before the output rate falls off as a result of pile-up. The input count rate is monitored during PIXE experiments. The output count rate is present in the final spectrum. The factor f is then used to adjust the final number of counts of a characteristic x-ray peak to the actual number of counts generated during the experiment.

IV. RESULTS AND DISCUSSION

4.0 General

The goals of the project were to construct a scattering chamber capable of performing routine and channeled PIXE and RBS experiments which was efficient, compact, and portable, to establish the procedure for measurement of dopant concentrations in bulk GaAs crystals, to experimentally determine the minimum detectable limits of trace elements in bulk GaAs, and to demonstrate and establish the channeled PIXE technique for future use. All goals of the project were achieved.

There was much preparatory work done before actual PIXE experiments were (or, actually, could be) begun. A data base of the relevant properties of most of the elements of the periodic chart was assembled. Key to the success of the project was the thick-film approximation to the integral of Eq. 10 which modeled the energy loss of the protons as they penetrate the GaAs and the associated depth dependence of the x-ray production cross section and absorption of the characteristic x-rays. Details of the modeling are discussed in Section 2.14. The x-ray production cross sections calculated from the model agree within $\sim\leq$ 10% with those published by other researchers [JJ 76]. Disagreement greater than 10% is attributed to the choice of value for the fluorescence yield, ω, which is multiplied by the ionization cross section to give the production cross section. Published values for the fluorescence yield of the elements vary over quite a wide range resulting in occasional discrepancies depending on

the value of ω chosen. A summary of the parameters for the various elements appear in Appendix II.

During the initial phase in which data was assembled and the thick-film approximation was devised, the software to remove background radiation from the spectra, fit raw peaks to Gaussian distributions, and perform statistical treatment of the data was written (details in Section 2.15). Also, standards by which to test and calibrate the process were made and chamber design and construction was begun.

4.10. Concentration Measurements

It is important in crystal growth research to be able to quickly and easily compare the concentration of dopants that are incorporated into the solid crystal from the melt to that which is calculated from the segregation coefficient of the dopant in the melt. The initial effort was focused on understanding the experimental processes and procedures and their connection to the theoretical description of the PIXE technique. Measurement of concentration of a variety of dopants in GaAs and comparision to the concentrations predicted from calculations from the melt was accomplished.

The same basic experimental arrangement to include instrumentation was used for all concentration and channeling measurements (Figs. 54 and 55). Protons of 1.0 and 1.5 MeV were supplied by the 2.5 MeV Van de Graaff accelerator facility at LBL. A Si:Li drifted semiconductor detector with a resolution of 150 eV FWHM was employed throughout the experiments. Detector dead (determined as described in Section 3.02)

time was ~33% and approximate corrections were made to all data. The particle beam size varied from 1 to 3mm. Detector solid angle was $7.04\text{-}7.75\times10^{-5}$ sr. Total accumulated charge varied from 5 to 30 μC, depending on the statistics required for a particular sample. In all experiments the Pd thin film and undoped GaAs standards were included to facilitate geometry-detector efficiency measurements and background removal, respectively. Typical chamber vacuum was 10^{-6} torr. Pulse height data were accumulated in a Davidson 512/1024 channel analyzer and stored on computer (floppy) disks for subsequent analysis. All samples were of LEC grown GaAs crystals obtained via courtesy of Dr. Grant Elliot of the Opto-Electronics Division of Hewlett-Packard.

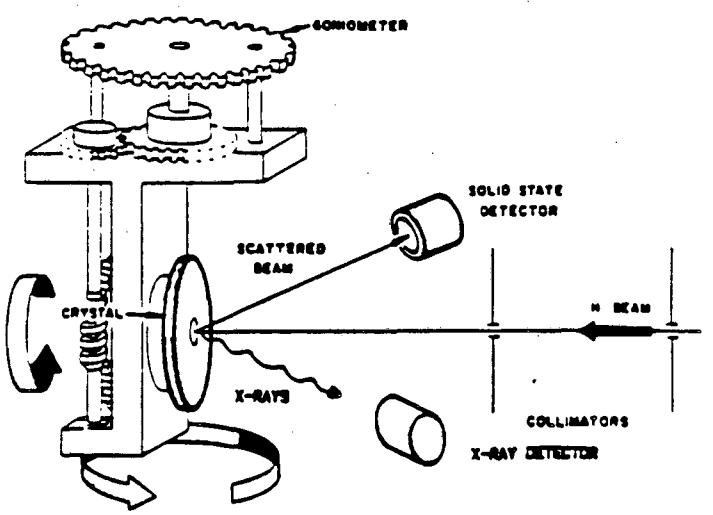

Fig. 55. Schematic of target goniometer and detector geometry for channeling experiments. (FMP 82, in part).

An advantage of the PIXE technique is the ease of sample preparation. The calibration standards consisted of thin films of Pd evaporated onto polished, undoped GaAs samples. Several standards were made, each with a different film thickness; the film thickness ranged from a nominal 50 Å to 1000 Å. Pd was chosen for its' availability, ease of evaporation of thin films, and nearness to the x-ray characteristics (to include detector efficiency) of indium, the dopant in GaAs to be studied first. Film thickness was determined to an accuracy of ~5% by the RBS technique. The purpose of varying the film thickness was, by knowing the number of atoms contributing to the x-ray yield, to check the accuracy of the thick-film approximation to the energy (depth) dependent cross section and absorption integral of Eq. 10 as replaced in Eq. 37. Furthermore, these standards served as a measurement of the product of the experimental geometry and detector efficiency throughout all experiments. Pd L-α x-rays were used in all cases. Doped GaAs samples were taken from wafers of LEC crystals, cut to dimensions of $\leq$ 1 cm^2, and lapped and polished to ~20 mil thick. Samples were mounted to an aluminum sample wheel with conductive silver paint. GaAs:In samples were taken from two different crystals. Indium doped samples were chosen for their high concentration (10^{19} to 10^{20} atoms/cm^3) which was expected to provide a distinctive peak above the background (important for early characterization of the experimental and data analysis procedures) and for the importance of indium doping in GaAs crystal growth technology as discussed in the Introduction. One crystal was doped with three times as much indium as the other, offering an excellent opportunity in which to verify the thick-film approximation, experimental

standards, and data accumulation and analysis techniques. Individual samples were cut from different areas of each wafer so as to provide a check of the ability to measure fluctuation in dopant concentration throughout the crystal.

Measurement of the experimental geometry by the yield of the Pd L-α x-rays coupled with the thick-film approximation (inserted into Eq. 37) gave a concentration of 2.35E22 atoms Ga/cm^3 in a crystal of GaAs. This value is 6.6% greater than the 2.21E22 atoms Ga/cm^3 present in a crystal with perfect stoichiometry, which is reasonably accurate. Therefore, it was concluded that both the calibration standards and the thick-film approximation were adequately describing the situation existing in the samples.

Experiments were done to investigate the effects of changes in collimation and in ion energy on the signal to noise ratio in the spectra. X-ray collimators consisting of 60 mil thick Al discs with aperatures of various sizes were prepared. The aperatures were machined to a fine edge to reduce scattering. Thin (~10 mil) mylar backing collimators with aperatures ~0.2 mm smaller than the corresponding Al collimator were prepared. The purpose of the mylar was to absorb fluorescent Al x-rays induced in the collimator and to reduce the intensity of low energy background radiation x-rays reaching the detector.

A series of spectra were taken of In doped samples at 1.0 and 1.5 MeV both with and without the mylar backing in place behind the collimator. It was found that the filter, in the region of the spectrum in which secondary electron bremsstrahlung is the dominate component of the background, improved the signal to noise (S/N) ratio

by about 10 at 1.5 MeV. This is the result of a reduction in the number of counts of low energy background radiation reaching the detector. For elements with x-rays of an energy less than E_{max} (defined in Eq. 20) a slight trend in the concentration calculated from the data accumulated with the filter in place toward values higher (than those without the filter) by a few percent was observed. This reflects the decrease in uncertainty when removing the background spectrum because of the improved counting statistics. For higher x-ray energies the mylar had no effect as the x-rays were able to penetrate to the detector.

Where secondary electron bremsstrahlung is dominant, a much more dramatic improvement in the S/N ratio is realized when proton energies are reduced from 1.5 to 1.0 MeV. The overall reduction of background yield was 50-70%. For sample H288 the S/N ratio at 1.5 MeV was about 3 while at 1.0 MeV it improved to about 7 as a result of the decrease in secondary electron bremsstrahlung (Fig. 56). Concentrations measured at 1.0 MeV with the filter are higher than those measured at 1.5 MeV without the filter by as much as 25-30%. In counting processes such as used in PIXE spectrometry the values obtained from the spectra with the best S/N ratio should be the closest to the true value. Therefore, the concentrations reported are those measured at 1.0 MeV H^+ with the mylar filter in place.

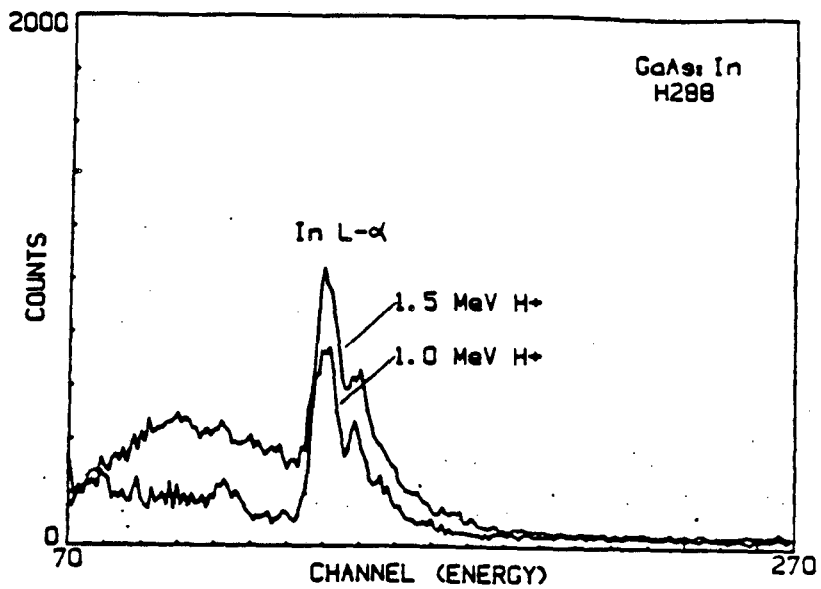

Fig. 56. Spectra of H288 for 1.0 and 1.5 MeV protons showing the reduced background from secondary electron bremsstrahlung and the increase in the S/N ratio for the 1.0 MeV case.

An increase in projectile bremsstranlung of ~25% was observed when the proton energy was decreased to 1.0 MeV. This is in accordance with the theory developed in the treatment of background radiation production processes. The yield of Ga K-α and As K-α x-rays in this region of the spectrum was so much greater than the increase in bremsstrahlung that no significant difference in the S/N ratio was observed. However, this seems to indicate that elements whose x-rays are greater than E_{max} will have lower detectable limits at 1.5 MeV than 1.0 MeV. Background from gamma rays will become important as proton energies are increased further since higher energy protons are

more likely to penetrate inside the Coulomb barrier of the nucleus. Therefore, protons of 1.0 to 1.5 MeV is the best chioce for this type of analysis.

The results of the concentration measurements were both in good agreement with the concentrations calculated from the melt and reproducible from experiment to experiment. The ratio of the concentration of indium in sample H276 to that measured in sample H288 was found to be 1:3, as expected. H276 was found to contain a nominal 3.75E19 atoms In/cm^3 and H288 a nominal 1.15E20 atoms In/cm^3 as measured at a proton energy of 1.0 MeV and with the mylar filter in place. In both cases the results are in good agreement with those predicted from calculation from the melt. The reported concentrations have an uncertainty of ±5 associated with them. It should be noted that such agreement between the ratio of dopant concentrations is expected to be valid only when samples are taken from similar sections of two crystals grown under comparable conditions. This is because the concentration of dopants incorporated into a crystal changes with length. Details and the measured concentrations of dopants in all of the samples are provided in Appendix I. Fig 57 shows the raw spectra from sample H276 and H288. When measurements were performed under conditions of identical geometry and beam energy, the results were reproducible as accurately as 5% with variations of closer to about 10 as the norm.

The results show that within the statistics of the measured values of concentration and the reproducibility that concentration profiles of dopants incorporated into a crystal can be mapped. Variations of greater than ~8-10% will be detectable. For most measurements the

beam spot size was 1 mm in diameter or ~0.80 mm^2. Therefore, the technique will be sensitive to fluctuations in concentration of ~10% in 1 mm. Haga, et al [HT 86], have reported measurements of the variation in In concentration in both radial and longitudinal directions in LEC GaAs.

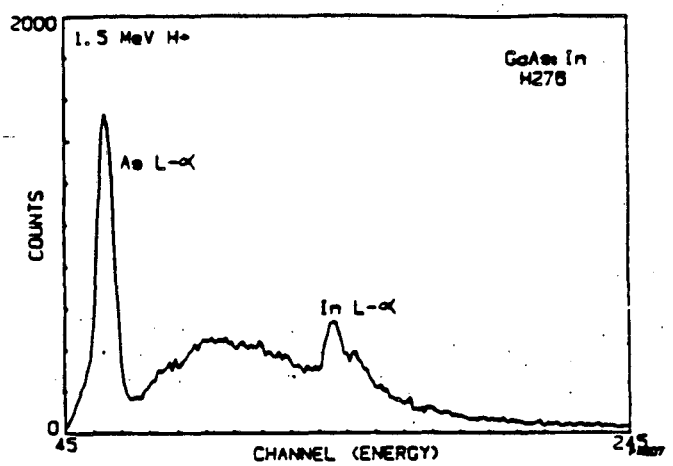

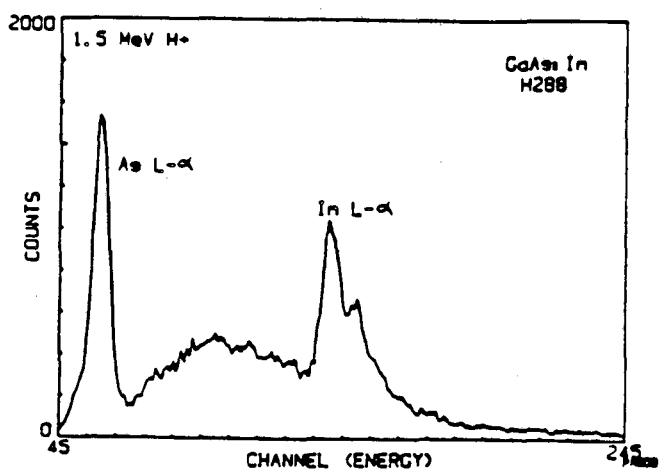

Fig. 57. X-ray spectra for H276 and H288 GaAs:In showing increase in yield of the In L-α peak for H288.

For Number Sequence Only

4.20 Minimum Detectable Limit

The minimum detectable limit of a technique will determine its' usefulness in identifying the source and concentration of trace elements as applied to the growth of high purity GaAs crystals. Using the geometry and techniques developed in the concentration measurement phase, undoped samples of GaAs were irradiated with 1.0 and 1.5 MeV protons. The characteristic x-ray peaks of Ga and As were used as an energy calibration scale to predict the channel where the characteristic x-rays of the elements of the periodic chart would lie. The gross number of counts of the background was determined by centering the FWHM over the position in the spectrum where an x-ray of such an energy would lie and finding the counts underneath that interval. The rule for a peak to be statistically significant was applied to the counts which in turn was used to find the minimum detectable concentration of the elements in bulk GaAs.

The results of the minimum detectable limit (MDL) measurements are shown in Fig. 58 for 1.0 and 1.5 MeV protons, respectively. A factor of about 2 decrease in the MDL is seen for 1.0 MeV protons as opposed to 1.5 MeV protons. This is caused by a decrease in background radiation production processes over the region of the spectrum in which a particular process is dominant. In the interval dominated by secondary electron bremsstrahlung the decrease roughly corresponds to the increase in the S/N ratio for a particular sample when lowering proton energy to 1.0 MeV from 1.5 MeV. The detectability limit is improved for elements with x-ray energies greater than E_{max} as a result of a decrease in background from gamma ray processes which

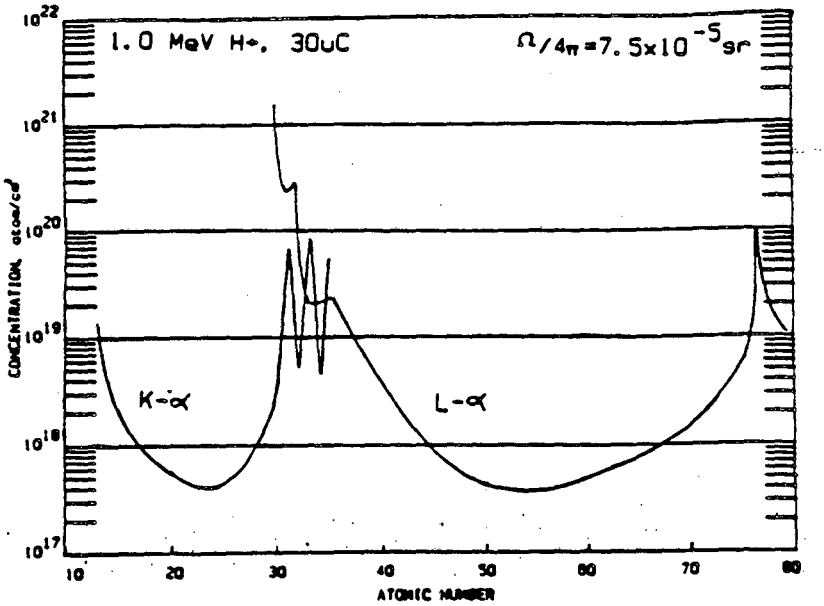

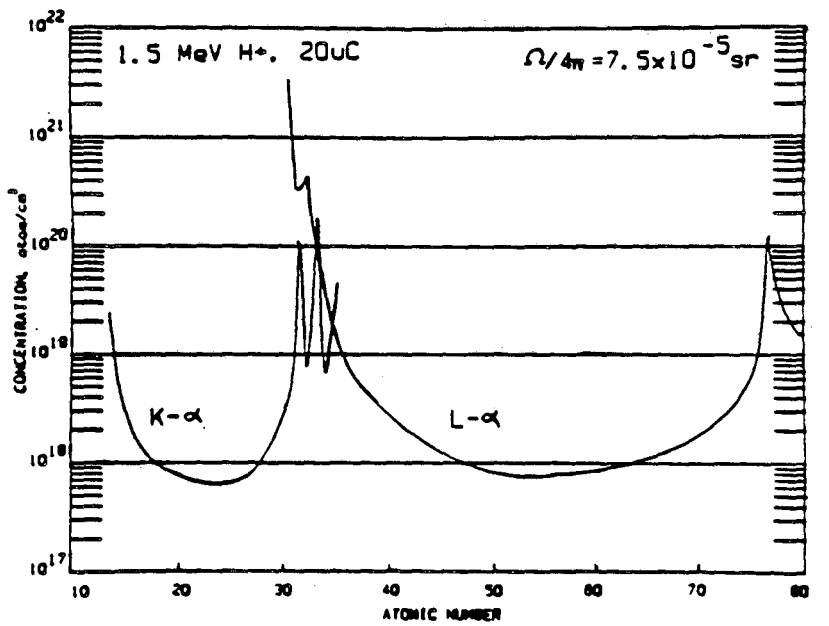

Fig. 58. The minimum detectable limit of trace elements in bulk GaAs for a) 1.0 MeV protons and b) 1.5 MeV protons.

counteracts the increase in projectile bremsstrahlung with decrease in projectile energy.

The detectibility limit for K-α x-rays decreases from Z = 13 to Z = 23 as a result of an increase in the fluorescence yield which is more than offset by a decrease in x-ray absorption arising from an increase in the x-ray energy. The increase in the MDL from Z = 23 to Z = 30 is attributed to a decrease in the x-ray production cross section with increase in Z. The sharp peaks about Z = 31 and Z = 33 are caused by the large number of counts arising from Ga and As K-α x-rays in those regions of the spectrum which will certainly mask small peaks from adjacent impurity elements. Likewise, a similar peak exists at Z = 77 owing to the As K-β x-rays. The MDL for Z = 31 (Ga) and Z = 33 (As) correspond to the amount of each element that must be present in addition to that which is already in the crystal (as in the case of non-stoichiometry) in order to be observed. Therefore, an excess of $\sim 10^{20}$ atoms/cm^3 of Ga or As are needed to observe non-stoichiometry in GaAs crystals.

The decrease in the MDL for L-α x-rays for Z = 30 to Z = ~50 is a result of the increase in the fluorescence yield and a larger decrease in absorption in a manner similar to that of the case for the K-α x-rays for Z = 13 to Z = 23. Both the presence of the As L-α x-ray and absorption of these low energy (< 1.2 keV) are responsible for the high MDL at Z = 30 to Z = 33. The increase in MDL for L-α x-rays for Z > ~70 is caused by the decrease of the x-ray production cross section with increase in Z.

The minimum detectable limit for thin (low Z) matrices of C and Al has been reported [JJ 76, FF 74] to be in the range of 10^{-7} to

10^{-6}. Furthermore, the shape of the MDL curve (Figs. 19 and 20) for all matrices is expected to be roughly the same over the range of elements of the periodic chart [JJ 76]. Also, with reference to the discussion on sensitivity, the increase in projectile bremsstrahlung with decrease in energy as it passes through the matrix should add a factor of about 10 to the MDL over that of the thin films of low Z. Absorption by the heavier matrix of GaAs add another factor of about 10 to the MDL. Therefore, the MDL of bulk GaAs was predicted to range from 10^{-5} to 10^{-4}. This was, in fact, observed as the best MDL was found for K-α x-rays to be in the mid 10^{17} atom/cm^3, as was the case for L-α x-rays for Z of about 50 to 60. Since the concentration of atoms in GaAs is on the order of 10^{22} atoms/cm^3, this corresponds to a lower limit of detectability of 10^{-5}, as predicted. Most of the minimum detectable concentrations are in the 10^{18} atom/cm^3 range, or, 10^{-4} as predicted.

The highest purity bulk GaAs crystals that can be obtained today have impurity concentrations on the order of 10^{15} atoms/cm^3, and require a MDL of 10^{-7}. This is far below that which is obtainable with this technique and, as such, PIXE with MeV protons is not suited to characterizing impurities in high purity GaAs as an aid to further reducing impurity levels. Better suited is the technique for mapping concentration profiles of dopants along the length and across the radius of crystals.

4.30 Channeling

4.31 Axial Scans, GaAs:In:Zn

An important part of this project was to achieve channeling with x-rays. Such a capability would enhance the ability to study semiconductor/semiconductor and metal/semiconductor systems. Of concern was the amount of beam divergence obtainable while still providing a current on the target of sufficient intensity so that measurement times remained practical. A perfectly parallel beam is the ideal toward which experimental arrangements are fashioned. Beam divergence is determined by both the collimator spacing and the aperture sizes. Collimator spacing (74 cm) was set by the configuration of the beam lines at the Van de Graaff facility so aperture size was the only free variable. An upstream collimator of 3 mm and a chamber collimator of 1 mm were employed to give a maximum beam divergence of 0.30°. This is well within the critical angle for channeling in GaAs (~0.55°-0.65°) for MeV projectiles and backscattering processes, so therefore it was predicted that the channeling phenomenon would be observed.

Initial experiments were carried out to investigate the channeling capability using 1.0 MeV protons incident upon <100> GaAs:In:Zn. Beam current was 6 nA (low to minimize channeling-destroying damage) and the accumulated charge was 4 μC. Fig. 59 a and b show the results of channeling along the <100>. The theoretical prediction of the minumum yield is about 3.3% while the experimentally measured minimum yield is about 5.3%. This is considered to be in good agreement with theory. The minimum yield for x-rays is about 50%. Since the x-ray signal is

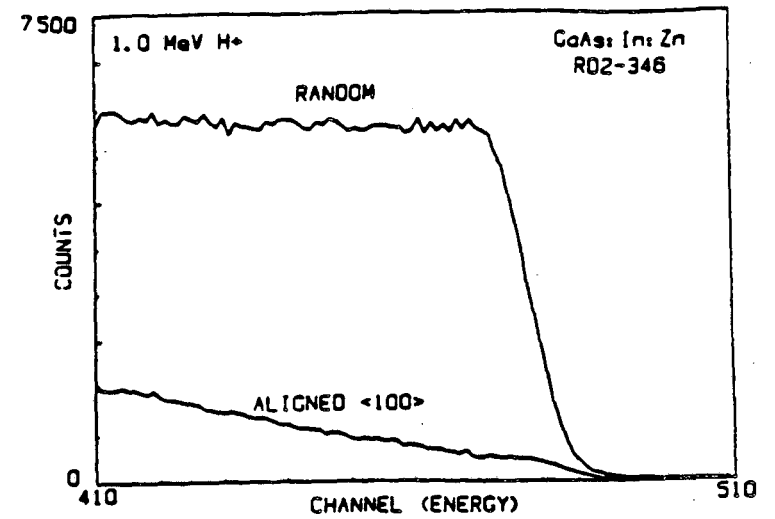

a)

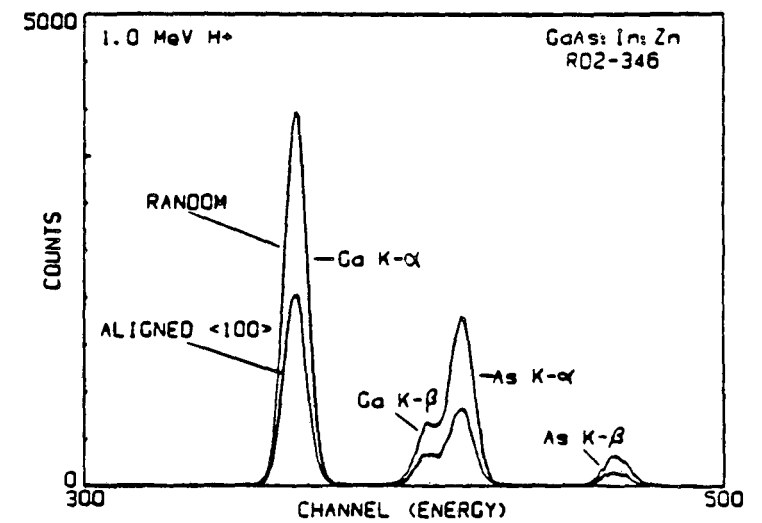

b)

Fig. 59. a) Channeled vs random backscattered particle yields for 1.0 MeV protons on <100> and "random" GaAs. b) The corresponding random and aligned x-ray yields.

the result of the integrated yield over the entire range of the particle in the matrix, this is in good agreement with what is expected from such an experiment. It is impossible to directly seperate the x-ray yield from just beneath the surface as can be accomplished with an RBS spectrum. Calculation of the minimum yield of x-rays just below the surface is possible when Eq. 37 is modified by the dechanneled fraction of the beam as in Eq. 66. This, however, does not represent a direct measurement of the minimum yield below the surface in the same manner that is realized in an RBS spectrum. Experimental values for the critical half-angle are not available as a complete axial scan of the <100> was not performed. The focus of this experiment was simply to establish the capability of channeling with PIXE in GaAs and in this sense was successful.

A complete axial scan was performed on a LEC grown GaAs:In:Zn crystal about the <110> direction. The beam characteristics were as those in the <100> channeling experiment. No attempt was made to tilt in the $(1\bar{1}0)$ plane toward the two <111> directions in that plane as in a sublattice site-preference experiment. The crystal was cut so that the surface normal was parallel to the [001] direction which, upon tilting to the [110] axis, would require rotation and tilting of the sample in order to remain in the (110) plane. This is not easily accomplished so <110> or <111> crystals are used for such experiments. Crystals of either of these orientations require only tilting to remain in the proper plane. This can be verified by noting the stereographic projections in Fig. 60.

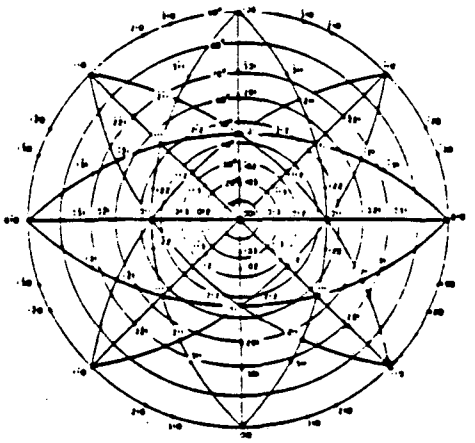

a)

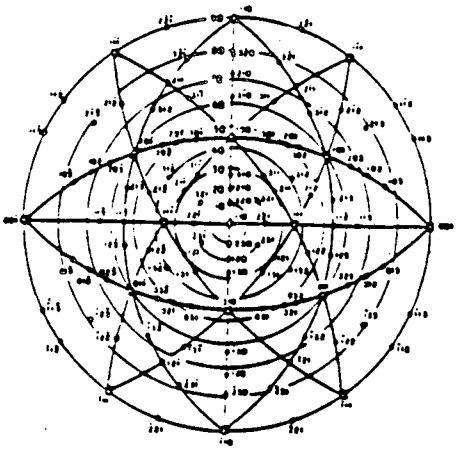

b)

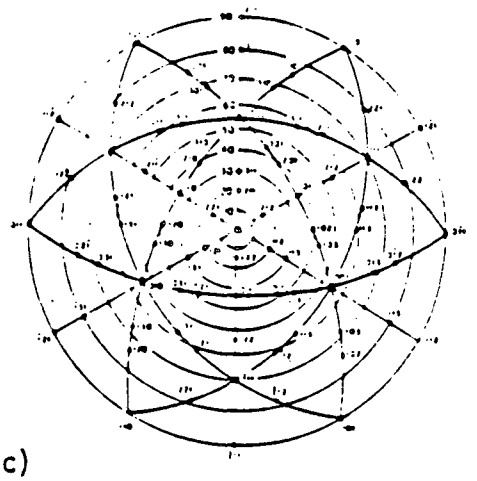

c)

Fig. 60 Stereographic projections for the major crystal axes of cubic crystals. a) <001>, b) <110>, and c) <111>. (AF 77).

Indexing the crystal surface as [001], the tilting in performed in this experiment, then, was along the (100) planar channel toward the [010] direction. The [011] axis bisects the angle between [001] and [010]. The point is that the axial scan was not performed in a random tilting direction but along the (100) plane. This becomes important when interpreting experimental results. The <001> stereographic projection of Fig. 60 maps the specific tilting condition.

The result of the <110> axial scan is shown in Fig. 61. The theoretically predicted minimum yield, χ_{min}, and critical half-angle, $\psi_{1/2}$, for backscattered particles are 2.33% and 0.643°, respectively. The experimentally measured minimum yield of backscattered particles is 4.30% which, as in the case of the <100> channel, is in good agreement with theory. The minimum yield for x-rays is in the neighborhood of 30% , not as low as the backscattered particle yield for reasons that have been discussed. There is a lower minimum yield for the x-rays in the <110> than in the <100> (30% vs 50%) because of the larger channel diameter. As predicted in the section on particle distributions within the channel, the flux is peaked in the channel center. In a larger channel, therefore, a greater fraction of the particles in the beam posses impact parameters too great for inner shell ionization processes so the yield of x-rays over the range of the projectiles decreases.

The measured critical half-angles for the backscattered particles and the x-rays are 0.78° and ~0.40°, respectively. There are no predictions of χ_{min} and $\psi_{1/2}$ for x-rays that are based on theory. Predictions, if necessary, are usually semi-empirical and

involve application of Eq. 66 to an experimentally generated RBS dip curve.

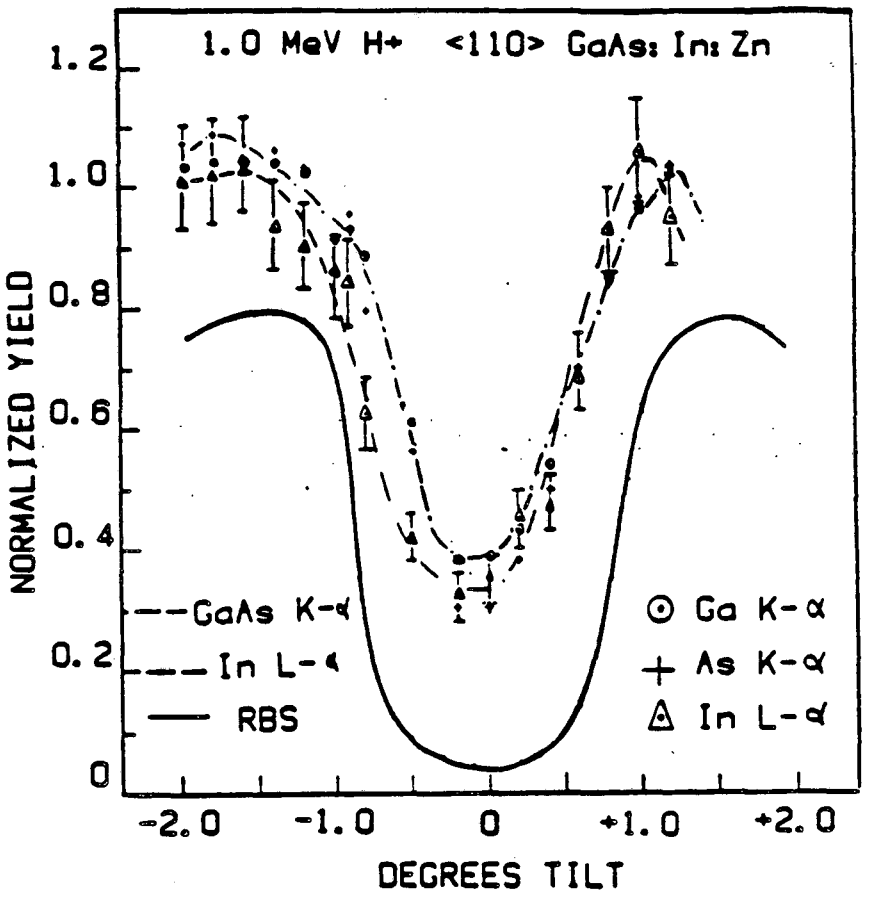

Fig. 61. <110> angular scan of GaAs:In:Zn using 1.0 MeV protons. Confirms directly that In is substitutional and indirectly that Zn is also substitutional.

The dip curve demonstrates the characteristic shoulder and flat bottom of such scans. However, the backscattered particle yield does not first exceed the random yield (in the shoulder) and then decrease to that yield outside of the channel. Furthermore, the measured $\Psi_{1/2}$ is greater than that predicted by theory. It would be expected that experimentally measured values of $\Psi_{1/2}$ would tend to be less than the predicted values. Both of these discrepancies can be explained by consideration of the specific path of the scan (ie., the specific tilting direction). Since tilting was carried out in the (100) plane a fraction of the beam experienced planar channeling when the conditions for [110] axial channeling were no longer met. The crystal was not in a random orientation with respect to the beam even though particles were no longer axially channeled. The effect of tilting in a plane through an axis is to lower the backscattered particle yield outside of the axial channel and to show an apparent broadening of the channeling dip. The effect is not as dramatic for x-rays since outside of the axial channel the dechanneled fraction of the beam over the range of the projectiles is high enough to cause high x-ray yields from deep within the sample which mask any surface effects. Also, in this particular case, the (100) channel in GaAs is quite narrow (~1.4 Å) leading to a shorter wavelength ocsillatory trajectory and more rapid dechanneling.

X-rays, like backscattered particles, can be used to evaluate substitutionality of dopants in semiconductors. Examination of the In L-α x-rays in the scan show indium to be strongly substitutional, as expected. The concentration of Zn was too low to be detectable by PIXE. However, it is still possible to assert with confidence that

the Zn is occupying substitutional sites. With regard to the flux distribution within the channel, interstitial impurities show a yield greater than that for random orientations. Given that the concentration of Zn in the crystal is known reasonably well from the segregation coefficient and from the concentration in the melt, it can be expected that if the Zn K-α x-ray yield was masked in random orientations interstitial Zn would produce an x-ray yield that would be present in the channeled x-ray spectrum. A look at the MDL plots shows that Zn must be present in concentrations in excess of $\sim 2.3 \times 10^{18}$ atoms/cm^3 for 1.0 MeV protons and that it lies next to gallium. The reduction in Ga K-α x-ray yield associated with channeling coupled with the increase in x-ray yield from interstitial Zn may allow the Zn to be seen. The concentration of Zn is the sample is as low as about 4.5×10^{18} atoms/cm^3. The measured value is $\leq 3.90 \times 10^{18}$ atoms/cm^3. This indicates that while some Zn x-rays are visible in the spectrum, they are not statistically significant when compared to the background. Since no Zn signal was observed in the channel (inside the dip curve), it was concluded that the Zn occupies substitutional sites.

TABLE IV

PREDICTED AND EXPERIMENTAL BACKSCATTERING CHANNELING PARAMETERS

Projectile	Axis	Predicted[ø] $\psi_{1/2}$	Predicted[ø] χ_{min}	Experimental $\psi_{1/2}$	Experimental χ_{min}
1.0 MeV H^+	<100>	0.540°	0.0334	NA*	0.0533±.0018
	<110>	0.643°	0.0233	0.78°	0.0430±.0014
	<111>	0.581°	0.0288	0.50°** 0.75°**	0.0567±.0019
1.5 MeV $4He^+$	<111>	0.674°	0.0291	NA*	0.0539±.0032

* NA: Experiment to obtain this data not performed.
** 0.50° for tilt toward <110>, 0.75° for tilt toward <001>.
ø Crystal temperature 300 K

TABLE V.

EXPERIMENTAL X-RAY CHANNELING DATA

Projectile	X-Ray	Axis	$\psi_{1/2}$	χ_{min}
1.0 MeV H+	Ga K-α	<100>	NA*	0.515±.006
	As K-α		NA	0.450±.008
	Ga K-α	<110>	0.39°	0.389±.004
	As K-α		0.42°	0.307±.005
	Ga K-α	<111>	0.30° 0.71°**	0.428α.004
	As K-α		0.36° 0.80°**	0.372±.005
1.5 MeV 4He+	Ga K-α	<111>	NA	0.139±.014
	As K-α		NA	0.151±.019

* Experiment to obtain this data not performed
** Lower value is for toward <110>, higher value for toward <001>.

4.32 Sublattice Site Preference, GaAs:Si

Compound semiconductors are unique in that, unlike those composed of a single element from Group IV, dopants may prefer one sublattice to another. Among the interesting phenomena to study is the question whether silicon, a Group IV semiconductor, resides in the gallium or the arsenic site in a GaAs crystal.

Silicon has long been incorporated into GaAs during crystal growth in quartz crucibles. The resulting material was n-type indicating that the majority of silicon atoms preferred the gallium site over that of the arsenic. However, it is not clear whether under certain conditions silicon will either switch preference or show none at all. Pronko and Bhattacharya [BP 83] have applied the standard technique described in the development of channeling to study site preference for Si implanted GaAs. Under the implantation and annealing process detailed in the reference, silicon appeared to show no tendency to occupy either sublattice over the other. There is some discussion [JJ 86] about silicon preferring the As site under high temperature crystal growth conditions and the Ga site under lower temperature growth. The standard technique of sub-lattice site determination detailed in Section 2.25.2 can be applied to this problem. However, it was of interest to see if there was a difference in x-ray or backscattered particle yields when the order in which the atomic species of the crystal were encountered and if any such differences could be applied to sublattice location studies. Therefore, channeling about the $[\bar{1}11]$ and $[\bar{1}\bar{1}1]$ directions was studied instead.

A description of the technique to be examined was given in the treatment of sublattice location techniques in Chapter II. A sample of LEC grown GaAs:Si with the surface normal parallel to the [001] direction was polished and prepared for study. Adhering to the advice given in Ref. [PB 83], protons were used to study the x-ray yields. The lowest energy practical for the Van de Graaff accelerator used was 1.0 MeV. Lower proton energy would be desirable for a sublattice preference study as any asymmetries are near surface effects and

lowering the projectile energy is the simplest way to reduce x-ray yields from deep within the sample. With reference to the discussion of the Kinematic Factor, K, and the mass resolution obtainable for various projectile/target systems, protons lack the mass resolution to seperate Ga and As surface peaks in a channeled RBS spectrum. Therefore, utilizing the fine versatility of the particular Van de Graaff machine at LBL, 1.5 MeV $4He^{+}$ ions were used to study the surface peak effects associated with $[\bar{1}11]$ and $[\bar{1}\bar{1}1]$ incidences. In both cases the beam current and accumulated charge were low (~6 nA, 2-4 μC, respectively) to minimize target damage and attempts were made to move the beam to new surface areas of the sample throughout beam exposure.

It is not easily possible to reverse the order in which the atomic species are encountered along <111> directions in a [001] crystal by tilting in the $(1\bar{1}0)$ plane through the [110] axis as in the standard technique. Study of the ZnS structure reveals that order reversal can be achieved by first locating the [001] channel then tilting along the (110) plane about the [110] axis toward the $[\bar{1}10]$ axis. At a distance of ~55° from the [001] lies the $[\bar{1}11]$ channel. A decrease in backscattered yield at a distance of ~35° resulting from the large $(1\bar{1}1)$ planar channel ($[\bar{1}12]$ direction) provides a useful checkpoint. To reverse the order of the atomic planes the crystal is rotated 90° about the sample normal ([001]) to reach the $[\bar{1}\bar{1}1]$ axis. Scans through the <111>'s are then accomplished along the respective {110} planes, not in a random direction. The significance of this was discussed in the previous section. Figs. 55 and 62 show the experimental arrangement, the crystallography is represented in the

<001> stereographic projection in Fig. 60.

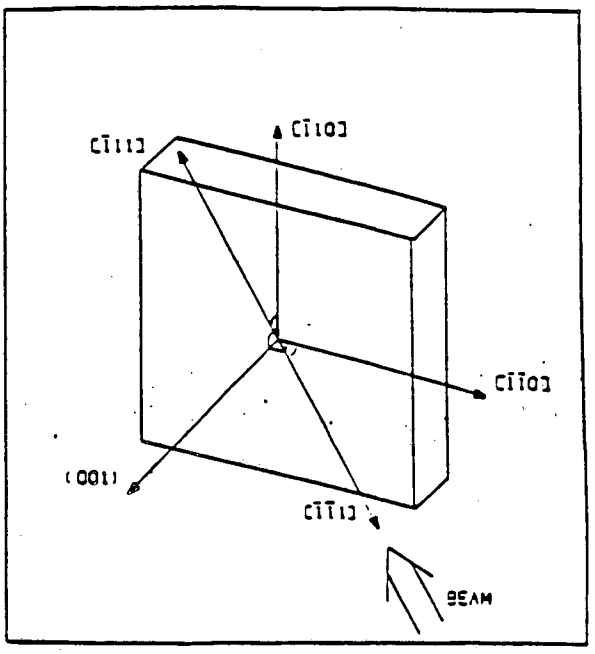

Fig. 62. Beam/Crystal geometry for the sub-lattice site determination experiments.

Although not required to observe any orientational effects with this technique, complete axial scans were conducted in both [$\bar{1}$11] and [$\bar{1}\bar{1}$1] directions. The order in which the scans were carried out were: 1) [$\bar{1}$11] 0° to +2° (toward [$\bar{1}$10]), 2) [$\bar{1}$11] 0° to -2° (toward [001]), 3) [$\bar{1}\bar{1}$1] 0° to -2° (toward [001]), and 4) [$\bar{1}\bar{1}$1] 0° to [$\bar{1}\bar{1}$0]). Crystal damage began to show up during the last scan. This, however, occurred after the critical 0° alignments were recorded so it did not have the effect of spoiling any asymmetry effect borne by the x-ray

yields that might have taken place.

The features of the dip curves are similar to those of the <110> curve generated with the GaAs:In:Zn sample. The backscattered particle and x-ray yields outside of the channel did not reach the random yields owning to the scan being performed along a planar channel. Small shoulders at the channel edges were observed in the RBS curves. The experimental values for the minimum yield and critical half-angle for the backscattered particles are compared with the theoretical predictions in Table IV. Again, acceptable agreement between the experimental and theoretical minimum yields (~5.6% vs ~2.9%, respectively) indicates that the crystal was adequately channeled.

An unexpected feature of the dip curves was the large difference in the widths about the 0° position of the channeling dips for the two tilting directions. This occurred for both $[\bar{1}11]$ and $[\bar{1}\bar{1}1]$ incidences. For simplicity only the results of the $[\bar{1}11]$ scan will be discussed witn all points being valid for the $[\bar{1}\bar{1}1]$ case. The channeling dip width of 0.75° for tilting in the [001] direction is greater than the predicted width of 0.58° and, based on the results of the <110> scan, is so by an amount that is reasonable given the larger spacing of the (110) planar channel (~2 Å vs ~1.4 Å). The effect of this on the yield outside of the channel as compared to that for the scan along the (100) plane can be seen in the plot of the axial scan RBS yield data in Fig. 63. The yield for the scan accomplished along the (110) is lower than that of the scan along (100) by a factor similar to the difference in size between the two. However, the narrow width for tilting in the $[\bar{1}10]$ direction must be explained.

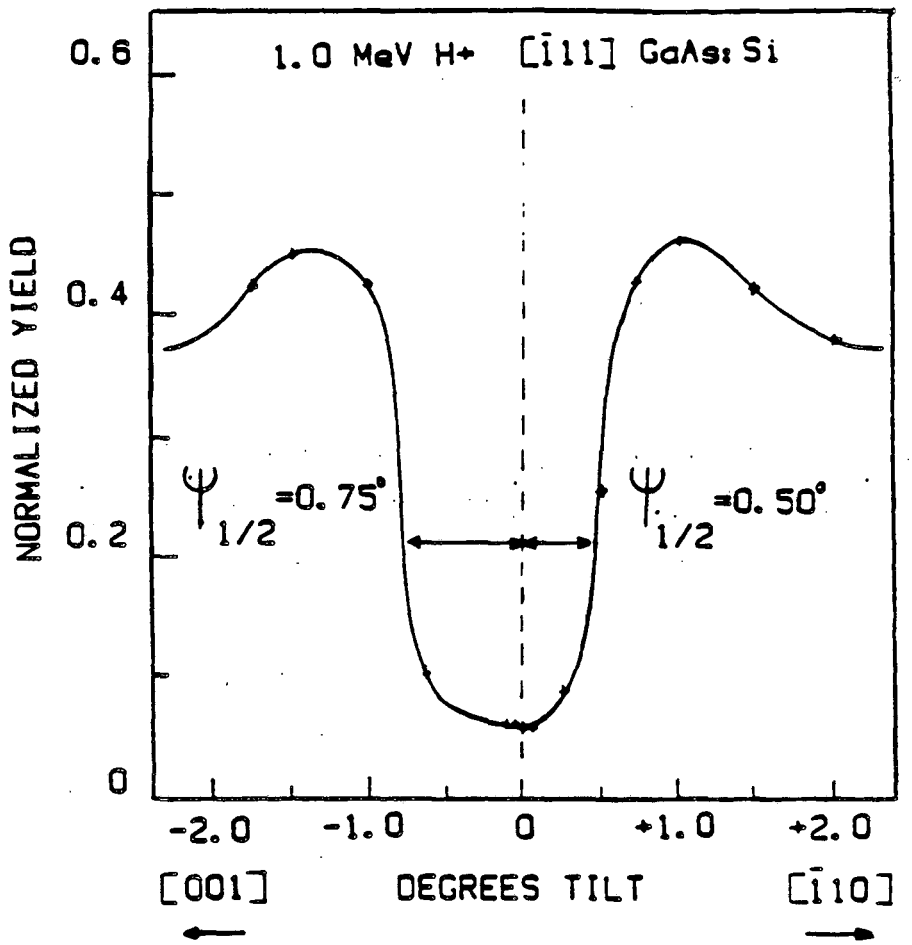

Fig. 63. Axial scan of backscatered particle yield for 1.0 MeV protons on [$\bar{1}$11] GaAs showing the unequal axial half-angles associated with the scan along the (110) planar channel toward [001] and [$\bar{1}$10]. Asymmetry results from the scan being accomplished by rotation about a two-fold rotational axis of symmetry ([110] axis).

Under typical experimental conditions and scanning paths not coinciding with a major crystallographic plane, an experimentally measured critical angle of 0.50° might be expected and as such, would

be considered to be in good agreement with the 0.58° predicted from theory and computer simulations. In most cases, crystal defects are the most probable cause of the narrower channeling dips. However, since the scan was accomplished along the (110) planar channel, the measured angle was expected to be greater than the predicted value by an amount similar to that found in the tilt toward the <100>. The reason for the discrepancy can be understood by considering the distribution of transverse energy of the projectiles and the equipotential contours which define their trajectories and the crystal geometry.

Under conditions of axial channeling the projectiles are contained by equipotentials that are defined by the aligned rows of atoms. With reference to the discussion of the spatial distribution of channeled particles, those ions with a high transverse energy are not confined to a specific channel as defined by specific atomic rows but are free to travel from channel to channel within the area bounded by the equipotential contour. Being of high transverse energy, the contours are very close (on the order of a few tenths of angstroms) to the atoms themselves. Thus, the more atoms encountered, the higher probability of a projectile experiencing a close-encounter event.

Although the projection of the atoms that make up the <111> channel onto a plane is symmetric about the tilting direction, or C_{3v}, the effect on the dechanneling behavior of the particles when a specific tilting path is followed is not. A crystal oriented with the beam along [$\bar{1}$11] tilted in the (110) plane is experiencing a rotation about an axis which is mutually perpendicular to the beam axis and the (110) plane. This is the [110] axis (note the stereographic

projection of the <100> in Fig. 60). Being a two-fold rotation axis and with the beam not aligned with a mirror plane of such an axis, a different arrangement of atoms is presented to the beam when tilting toward [$\bar{1}$10] than when toward [001]. With reference to the discussion of imparting a larger component of transverse energy (to the particles of the beam) in specific crystallographic directions, the basis for the standard sublattice location technique, an increased fraction of the particles in the beam experience a skew in their transverse energy toward a structure which is less open than when tilting in the other direction. Thus, more atoms which define the equipotentials containing ions of high transverse energy are encountered. The result is that the condition for axial channeling is no longer satisfied at smaller angles about the 0° position when tilting toward the [$\bar{1}$10] as opposed to tilting toward the [001]. A greater fraction of the projectiles possess increases values of transverse energy in directions of a more or a less dense atomic arrangement, depending on the direction of tilting, giving rise to the observed phenomenon. Axial scans of the <111> in random directions are expected to yield dip curves which are symmetric about the 0° orientation.

At the present, no application of this effect to the determination of sublattice site is seen as there appears to be no preference to interact with only one atomic species of the compound. This illustrates the degree to which the exact orientation of the crystal and the resulting atomic positions relative to the beam can be determined.

The motivation for performing this experiment was to try to observe asymmetries in x-ray yield in the bottom of the dip curves

that would reverse when the order of atomic species encounter was reversed. Differences between yields must be statistically significant in order to have meaning. Again, since projectiles penetrating deeper than ~1000 Å lose the initial conditions, any asymmetry effect was expected to be small, or nearly masked by the overwhelming number of x-rays originating from depths greater than 1000 Å . Ratios of As K-α to Ga K-α x-rays were used to examine the x-ray yield asymmetry. The standard <110> scan technique employs adding x-ray counts for the elements through the region of the asymmetry in the dip curve shoulders and then dividing these sums to obtain the asymmetry ratios. Since this proposed technique relies on differences in yields when the crystal is aligned 0° from the channel axis, only 0° yield are used with small angular divergence yields (±0.05°) checked to insure axial alignment. The results, as shown in Table III, display a difference in the As to Ga K-α x-ray ratios between the two <111> directions but the difference does not appear to be statistically significant and therefore no asymmetry in these x-ray yields was observed.

There does, however, appear to be a difference between the silicon yields which is statistically significant. It is entirely possible that an asymmetry effect in the Ga and As x-rays were overwhelmed by x-rays from beneath the near surface region of the crystal while, because of the strong absorption of the Si K-α x-rays by the matrix, a significantly greater fraction of those x-rays that were detected arise from a depth over which projectiles are preferentially interacting with the leading atoms of the set. This would account for the presence of the asymmetry effect in the (near surface) silicon

x-rays and the absence of the effect for the (deep bulk) gallium and arsenic x-rays.

Care must be taken when computing and interpreting these ratios. Allowances for the differences in the dechanneled fraction of the beam between the two channeling conditions must be accounted for. In the case of As K-α to Ga K-α x-ray ratios, each ratio is taken from Ga and As yields from the same channeling data ([$\bar{1}$11] As K-α/Ga K-α, [$\bar{1}\bar{1}$1] As K-α/Ga K-α). Then the two ratios are compared to each other without any differences in the dechanneled fraction of the beam affecting the results. This is not the case, however, when comparing the silicon yields from one <111> channel to the other. Differences in the dechanneled beam fraction can lead to incorrect ratios. Therefore, the ratio of silicon to an x-ray (Ga K-α, for example) from the same channeling data must first be taken. These ratios are then compared to see if there is, in fact, a difference in the silicon yields for the two orientations. The data from this experiment do show a difference in silicon yield between the two <111> directions which is statistically significant. Fig. 64 a and b is a plot of the x-ray yields for angular scans of +/-0.10° about 0° alignment. Table VI displays the ratios of the x-ray yields that were observed.

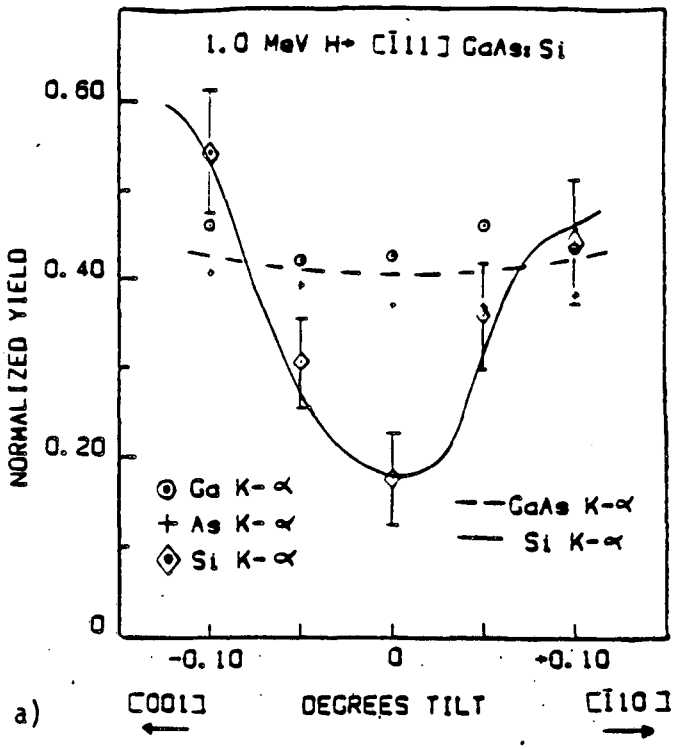

a)

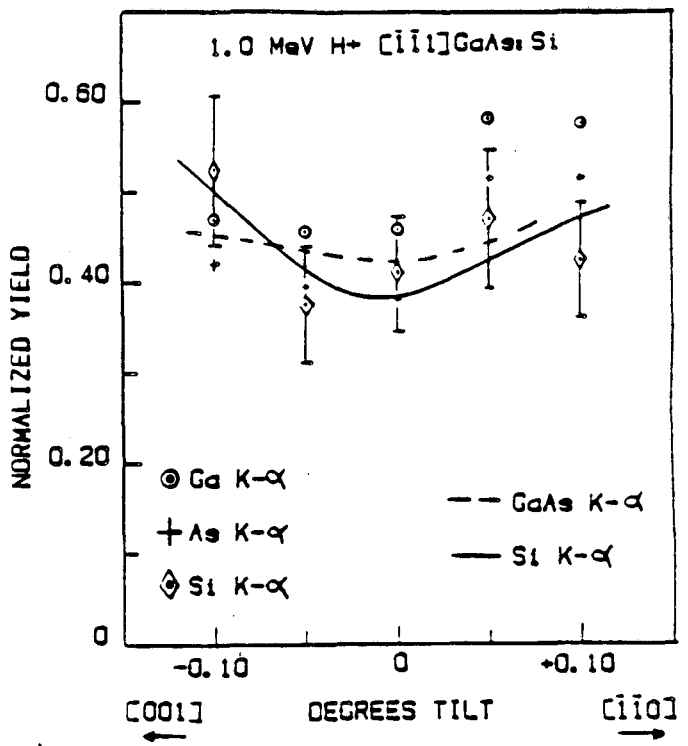

b)

Fig. 64. Axial scan (+/-0.10°) x-ray yields for a) [$\bar{1}$11] GaAs:Si and b) [$\bar{1}\bar{1}$1] GaAs:Si for 1.0 MeV protons. a) Shows marked decrease in the yield of Si K-α x-rays at the 0° position for [$\bar{1}$11] that is not present in b), [$\bar{1}\bar{1}$1]. Indicates a possible preference of the Si for one sub-lattice site over the other.

TABLE III.

[111] vs [$\bar{1}$11] Axis X-Ray Yield Ratios

Axis	X-Ray Ratio	Value	Stat. Significant
[111]	As K-α/Ga K-α	0.5277±.00733	NO
[$\bar{1}\bar{1}$1]	As K-α/Ga K-α	0.5233±.00714	
[$\bar{1}$11]	Si K-α/Ga K-α	0.0070 ±.0017	YES
[$\bar{1}\bar{1}$1]	Si K-α/Ga K-α	0.0155 ±.0020	
[$\bar{1}$11]	Si K-α/As K-α	0.0133 ±.0033	YES
[$\bar{1}\bar{1}$1]	Si K-α/As K-α	0.0297 ±.0038	

These results indicate that the silicon incorporated into the crystal under the associated growth conditions does indeed posses a sublattice site preference and that that site is the one which leads (encounters the beam first) in the [$\bar{1}\bar{1}$1] orientation. However, although the ratio of As K-α to Ga K-α x-rays is different for the two orientations, they are not different within the statistics. Therefore it is not yet possible to determine which of the sublattice sites the silicon prefers.

Since the x-ray yields alone were not sufficient to determine which sublattice site the silicon occupied, the surface peaks in the RBS data were examined. Protons lack the necessary mass resolution to separate Ga and As surface peaks so 1.5 MeV $^4He^+$ ions were employed. Although the sample was not repolished, attempts were made to conduct the study on fresh parts of the surface.

Some important differences between conducting PIXE/RBS experiments with H^+ vs $^4He^+$ were noted. Firstly, the surface peak of the spectra

channeled with alpha particles contained much more information regarding the Ga and As, as expected. Secondly, the dechanneled fraction of the beam was is far less for helium ions than it is for protons (Fig. 65 a). This, coupled with the lower x-ray production cross section, has significance in reducing the "noise" (ie., unwanted x-rays from deep within the sample) present in the surface x-ray yield which has been discussed. Therefore, to first order, it appears that using He ions results in a more near surface technique which is what is required by this technique. Dramatic differences are seen in the x-ray yields for Ga K-α and As K-α x-rays generated by protons and by alphas, as shown in Fig. 65 b and c. Unfortunately, the x-ray peaks produced by α-particle irradiation are not the smooth, large, near perfect Gaussians of those peaks produced by protons. Fitting of these peaks to Gaussians so as to determine the counts in the peak and, subsequently, the yield ratios results in uncertainties that are so large that they destroy any hope of observing the subtle differences in yield that may or may not exist. Attempting to improve the counting statistics by increasing the accumulated charge will cause more crystal damage and increase the buildup of contaminating layers on the surface of the sample which, too, may mask asymmetry effects.

It does not appear that α-particles will provide adequate x-ray data with which to work for this technique, the standard technique, and any experiment in which good, sharp, x-ray peaks with a minimum of sample damage is necessary for success. Therefore, for the purposes of x-ray analysis in situations such as this, protons are the particles of choice.

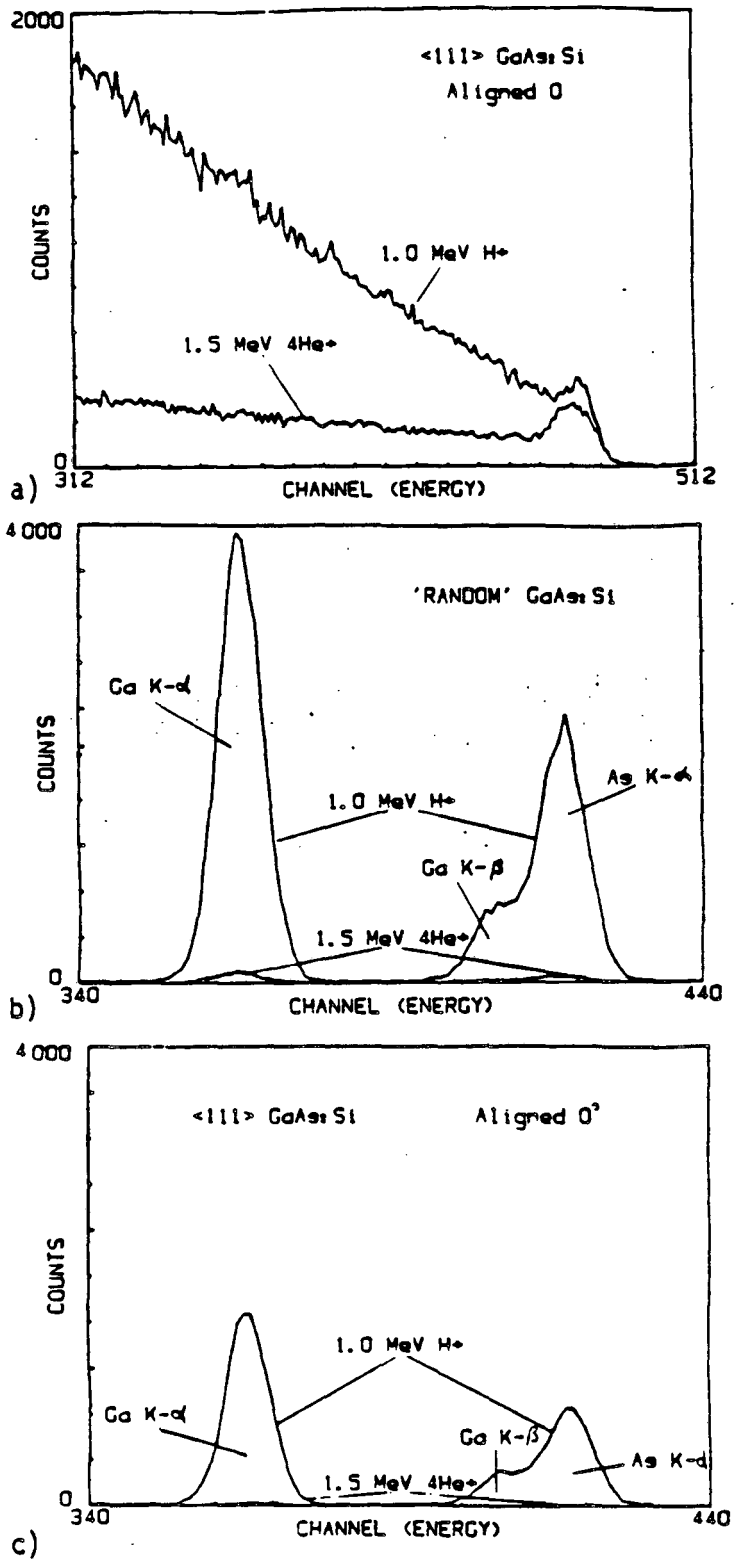

Fig. 65. a) Dechanneled particle yields for H^+ vs. $^4He^+$ projectiles. b) Random x-ray yields for H^+ and $^4He^+$ ions. c) Channeled x-ray yields for H^+ and $^4He^+$ projectiles.

The value of using $^{4}He^{+}$ projectiles in this case lies not in their x-ray production characteristics but in their superior mass resolution. It is impossible to study surface peak characteristics of GaAs using protons. Examination of the surface peak data from α-particles shows some promise in learning the identity of the atom occupying the lead position in the [$\bar{1}\bar{1}1$] orientation which is preferred by the silicon. When the surface peak spectra are overlayed on eachother (Fig. 66), there is a definite displacement of the surface peak for the [$\bar{1}\bar{1}1$] to lower channels (lower backscattered energy) relative to the surface peak for the [$\bar{1}11$]. This would be expected for the case where the dominant surface element was gallium. Coinciding with this displacement is an increase in yield of the gallium surface peak and decrease of the arsenic surface peak for this orientation relative to the other. Therefore, this result, in conjunction with the results of the x-ray yield experiments, seems to indicate that silicon tends to occupy the gallium sublattice site when a GaAs crystal is grown by the LEC technique under the conditions present. The ratios of the As/Ga surface yields are listed in Table IV and show that there is indeed a difference in the yields caused by the order of atomic stacking.

TABLE IV

Gallium and Arsenic Surface Peak Yields

Axis	Element	Yield	As/Ga
$[\bar{1}11]$	Ga	726 ±61.07	
			1.730 ±.169
	As	1258 ±62.21	
$[\bar{1}\bar{1}1]$	Ga	1035 ±63.68	
			0.881 ±.080
	As	912 ±61.17	

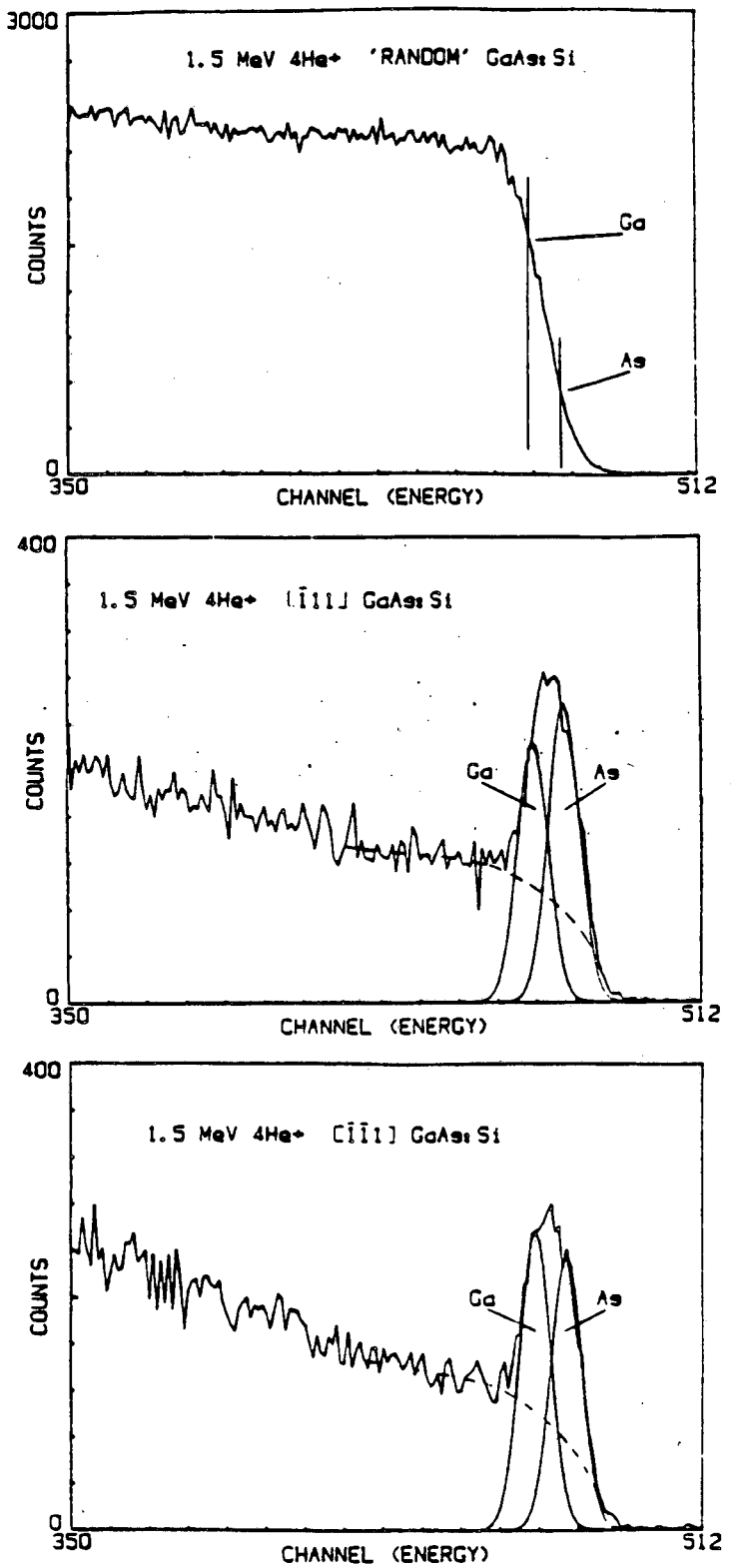

Fig. 66. Surface backscattered particle yields for 1.5 MeV $^4He^+$ ions on "random", [1̄11], and [1̄1̄1] GaAs:Si showing slight peak shift to lower energies corresponding to an increase in the yield from Ga atoms for [1̄11] incidence. Indicates the order of the stacking of the Ga and As atoms for each incidence.

Several factors must be considered when interpreting these results before definite conclusions can be drawn. The conclusion is based on a single set of data with the assumption that no unforseen systematic errors masked the true conditions existing in the dynamic interaction between the beam and the solid; the results present a true description of reality. With regard to the x-ray yields, an important factor affecting the near-surface yields is that the proton beam was collimated to a divergence of $\leq 0.30^{\circ}$. This may be too great of a divergence to ever see a difference in As K-α and Ga K-α ratios. Those who employ the standard site-preference technique do so with a beam divergence that is an order of magnitude less than what is available with this experimental configuration. It may not be possible to practice either technique with this degree of divergence. Likewise, conducting this experiment with $\leq 0.03^{\circ}$ beam divergence may yield the desired asymmetry effect from the x-rays alone eliminating the need for α-particle surface peak analysis.

Insofar as the interpretation of the surface peak data is concerned, it is assumed that any amorphous oxide or other impurity was formed on the surface had no preference for either a gallium or an arsenic oxide (or nitride, whatever the case may be). Our experiments were not conducted under high vacuum conditions as they are used for surface science. As a result, the surface of the sample was indeed contaminated with some sort of film. Analysis of the RBS spectrum (Fig. 67) showed this to be carbon-based. Surface peaks are very sensitive to impurity layers which serve to increase the width of the peak and alter the surface yields [CMN 78].

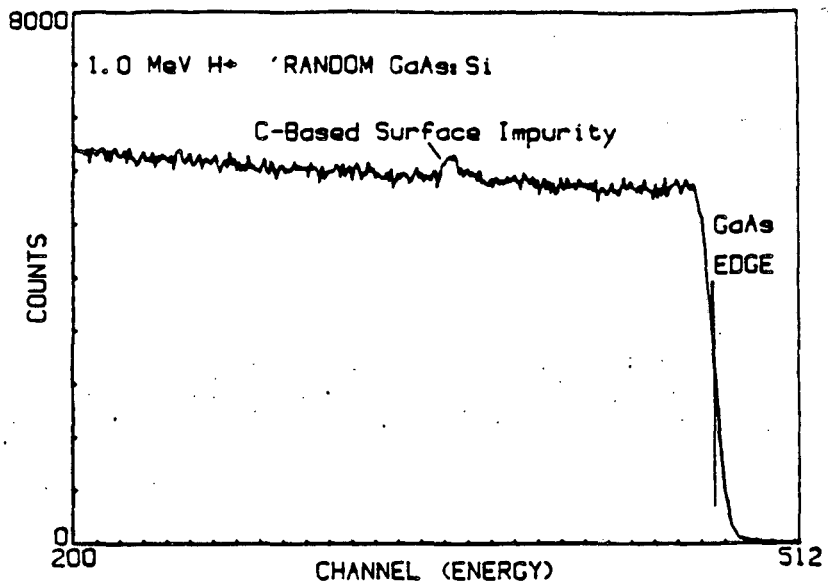

Fig. 67. "Random" spectrum of 1.0 MeV H^+ on GaAs:Si showing the presence of a carbon-based impurity on the surface of the sample as a result of imperfect vacuum and beam-spot heating of the target.

Therefore, the surface peak data is from a contaminated sample which may have influenced the results. Also, it is extremely difficult to separate overlapping peaks making such a procedure prone to error. Higher energy α-particles or the use of heavy ions for backscattering studies would serve to separate the Ga and As surface peaks and provide easier, more accurate determination of the associated yields.

The apparent observation of silicon occupying the Ga sublattice site is from results that appear to cross check among themselves and

with experience of many years of n-type GaAs containing silicon impurities. More work is required before it can be proven that there is indeed a <111> orientational effect that is expressed in the yield of characteristic x-rays and backscattered particles and that such an effect is applicable to specific site determination. Therefore, while there are strong suggestions that the asymmetry effect was observed and is applicable to sublattice site determination, it can not be concluded from this data that there is an orientational effect on the yield of characteristic x-rays and of the energy of backscattered particles.

V. CONCLUSIONS

As is the case when any analytical tool is introduced to a facility which heretofore had been lacking, there exists many possibilities for future work both within CAM and for groups in need of characterization of solids capabilities. When PIXE is used in conjunction with RBS, nearly the entire periodic chart can be covered in a fast, simple, non-destructive fashion. A solid state detector simultaneously measures the yield of x-rays over a wide range of energies making the technique extremely versatile. Sample preparation of solids, in most cases, consists of polishing to a mirror finish. Even this is not an absolute requirement as powder samples can also easliy be analyzed. The PIXE/RBS technique is a valuable addition to those interested in crystal growth, implantation and annealing studies, materials modification studies such as radiation damage and

ion beam mixing, surface properties such as the investigation of epitaxial films, and, of course, lattice and sublattice location of foreign elements within a matrix.

The procedure which has been established to determine the concentration of elements in a sample is both straightforward and accurate, requiring little time to aquire the data. Once calibration of the experimental system is achieved, analysis can be performed without the use of standards although, given the simplicity of running an experiment, there is no compelling reason to avoid running a standard along with the samples. The necessary software required to perform the analysis of the spectra to include modeling of the energy (depth) dependent x-ray production cross section and absorption, background radiation removal, and the fitting of the raw x-ray peak to a Gaussian distribution was developed as a part of the project. The resulting combination of experimental and data analysis procedures measures concentrations to an uncertainty of as good as 5% and it has been demonstrated that the resulting measurements are in good agreement with expected values.

Included in the project was the determination of the minimum detectable limit of trace elements in bulk GaAs crystals. Most elements, by using the characteristic K-α or L-α x-rays, are detectable to concentrations ranging from 10^{-5} to 10^{-4} atomic fractions, corresponding to 10^{17} to 10^{18} atoms/cm^3. Sensitivity is ultimately determined by the intensity of background radiation arising mainly from secondary (knock-on) electron and incident projectile bremsstrahlung. Protons of 1.0 MeV provide a better signal to noise ratio and a factor of 2 improvement in the minimum detectable

limit than exhibited by 1.5 MeV protons. Based on the rules for x-ray background production processes, this sensitivity can be expected for elements in matrices of mid-Z elements. Since these detectable limts are higher than the impurity levels found in most semiconductors today, the PIXE technique as practiced in this study will not serve as an aid to identifying the source of impurities in a crystal growth program dedicated to the production of ultra-pure material but is better suited to measure the concentration profiles of desired dopants along the longitudinal and radial dimensions of the crystal.

The PIXE technique has been succesfully combined with the RBS technique to provide the capability of channeling semiconductor, or other, crystals with x-rays and backscattered particles, allowing the characterization of elements which are lighter than the matrix to be accomplished. Therefore, this study has shown the promise that the combined PIXE/RBS technique holds for semiconductor crystal growth research. A scattering chamber that is efficient, compact, and portable was constructed with the feature that both RBS and PIXE measurements to include channeling can be conducted simultaneously. This apparatus was used to demonstrate the channeling technique with particle-induced x-rays. The resulting defining features of the channeled spectra, the minimum yield and critical half-angle for channeling, agree very well with the values that are predicted from channeling theory and computer simulations. Axial scan of the <110> axis in a sample of GaAs:In:Zn directly confirmed that, at least in this orientation, indium, added to decrease the dislocation density in as-grown crystals, is strongly substitutional. The substitutioanlity of Zn was indirectly confirmed by the absence of Zn K-α x-rays in the

channel dip curve.

Experiments were conducted to examine the sublattice site preference of Si in LEC grown GaAs using asymmetries in both x-ray and energy of backscattered particle yields in adjacent <111> directions. The results indicate that while this method of site determination unique to ZnS crystals show there to be a preference for the silicon to occupy one sublattice site over the other. Combined PIXE and RBS analysis suggest that the preferred site is the gallium site. However, owing to the beam divergence of the experimental set-up and to contamination of the surface during data aquisition, it can not be decisively concluded that this asymmetry effect was observed and is applicable to sublattice site determination. Suggestions for further study of this phenomenon include placement of the scattering chamber so that a beam divergence of $\leq 0.03^{\circ}$ is realized, application of UHV technology to a new scattering chamber, and use of heavy ions for RBS surface peak measurements.

It was shown that by tilting along specific directions about known axes of rotation it is possible to learn the precise orientation of the crystal and the associated arrangement of the atoms of a diatomic compound. This is of value when conducting implantation or epitaxial growth of semiconductor materials.

Finally, the educational experience contained in this project is invaluable and will serve the author well.

APPENDIX I

Crystal growth by the LEC method is a one pass procedure and as such is described by a "normal freeze" solidification process. The incorporation of dopants into a solid from a finite source in the melt is determined by its segregation coefficient, k. Table AI.I lists the effective segregation coefficients in GaAs for the dopants characterized in this study.

TABLE AI.I

SEGREGATION COEFFICIENTS FOR ELEMENTS IN GaAs

Element	k[a]
Ge	0.01
In	0.10
P	2.50
Si	0.13
Sn	0.08
Zn	0.40

a Ref [HL 80]. Data obtained frpm Cz crystals using (111) seeds, As face inserted into stoichiometric melt.

The relationship between the concentration of the dopant in the original melt to the concentration of the dopant in the solid as a function the fraction solidifies (g) is given by:

$$C_s = C_o k(1-g)^{k-1}, \qquad \text{(AI.1)}$$

where C_s and C_o are the dopant concentrations in the solid and the original melt (ie., g = 0), respectively, k is the effective segregation coefficient, and g is the fraction of the melt that is

solidified.

The normal freeze equation (Eq. AI.1) was applied to calculate the dopant concentration profile expected for each crystal studied. Using this information, predictions can be made as to the location in the crystal from where the samples were taken. Table AI.II lists the concentrations of the dopants as measured by PIXE. Figs. AI.1-AI.7 show the calculated dopant profiles.

TABLE AI.II

MEASURED DOPANT CONCENTRATIONS

Sample	Dopant	Conc. (atom/cm^3)
H276-1	In	2.78×10^{19} $\pm 1.22 \times 10^{18}$
H276-2	In	4.78×10^{19} $\pm 1.27 \times 10^{18}$
H288-1	In	1.30×10^{20} $\pm 2.36 \times 10^{18}$
H288-2	In	1.02×10^{20} $\pm 2.10 \times 10^{18}$
RD2-341	Sn	$\leq 1.11 \times 10^{18}$
RD2-342	Zn	$\leq 3.90 \times 10^{18}$
RD2-344	Si	$\leq 1.50 \times 10^{19}$
RD2-345	P	$\leq 1.05 \times 10^{19}$
RD2-346	In-Zn	In: 3.47×10^{19} $\pm 1.22 \times 10^{18}$ Zn: $\leq 3.68 \times 10^{18}$
RD2-035	Ge*	$\leq 1.95 \times 10^{19}$

* Melt data not available.

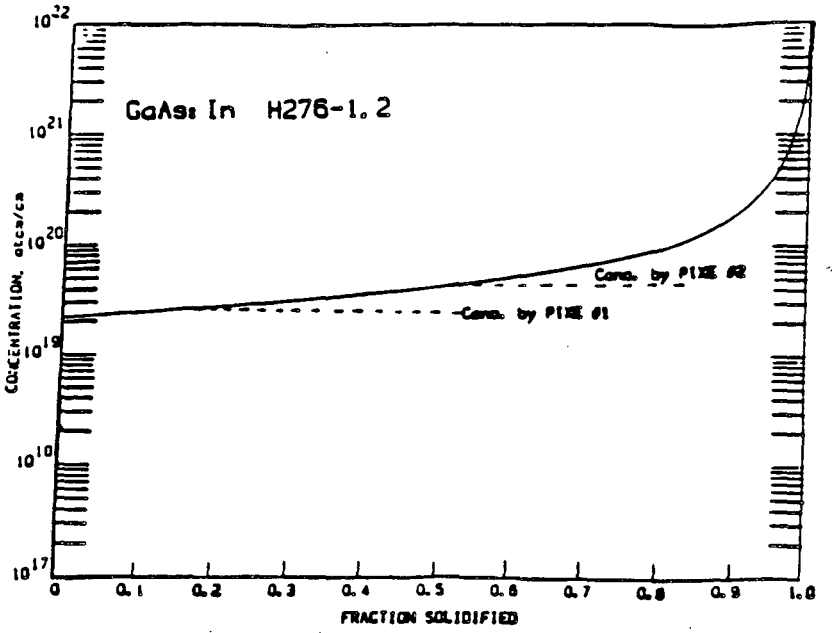

Fig. AI.1. Dopant concentration profile for the crystal H276 and the concentrations for samples #1 and 2 as measured by PIXE.

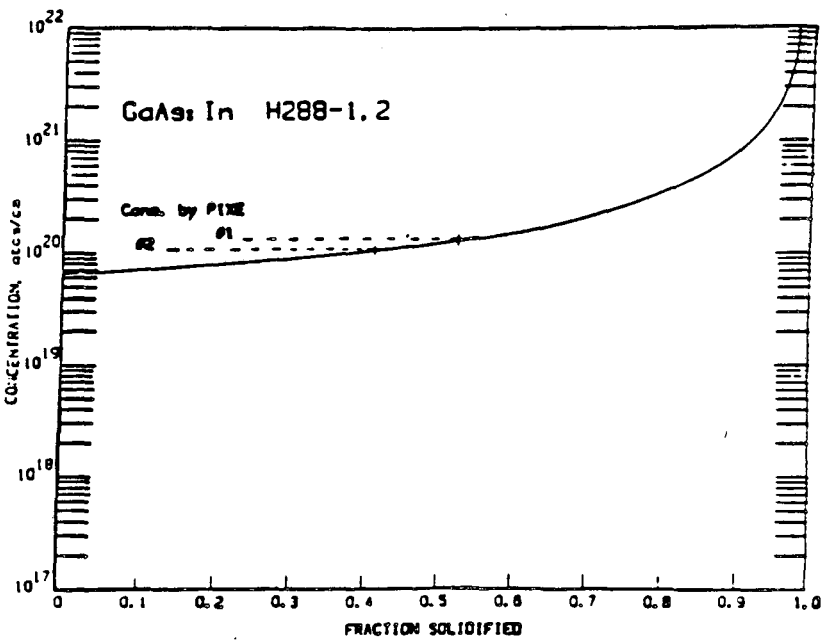

Fig. AI.2. Dopant concentration profile for the crystal H288 and the concentrations for samples #1 and 2 as measured by PIXE.

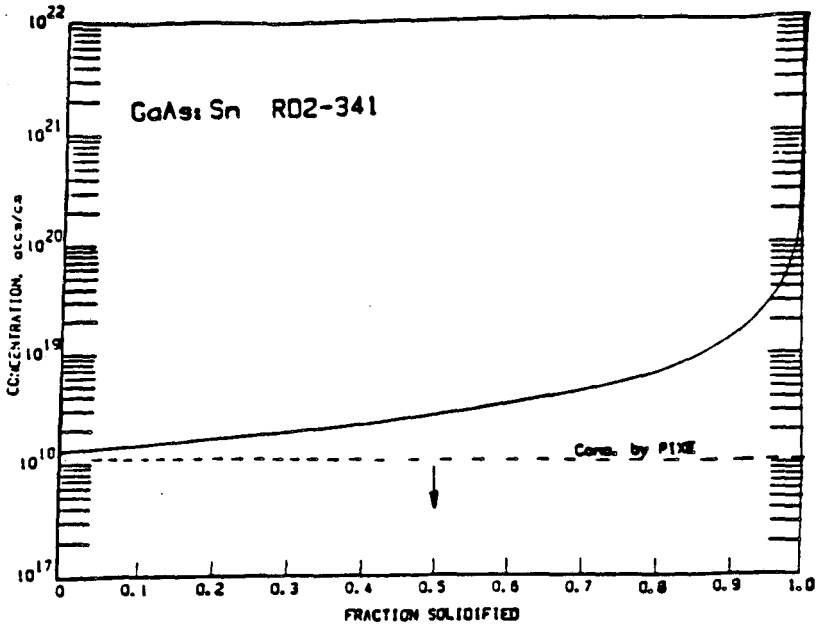

Fig. AI.3. Dopant concentration profile for crystal RD2-341 and the concentration as measured by PIXE.

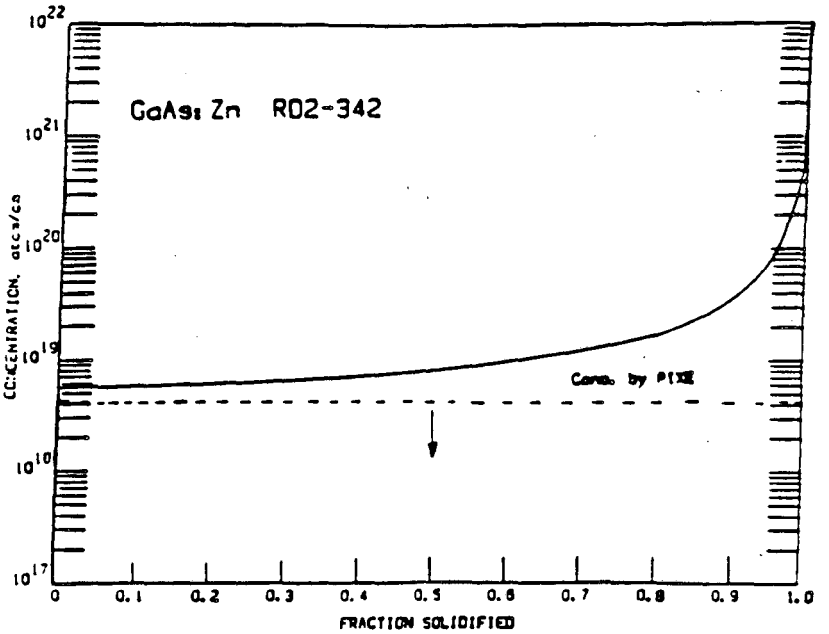

Fig. AI.4. Dopant concentration profile for crystal RD2-342 and the concentration as measured by PIXE. This crystal was used as a base for sample RD2-346.

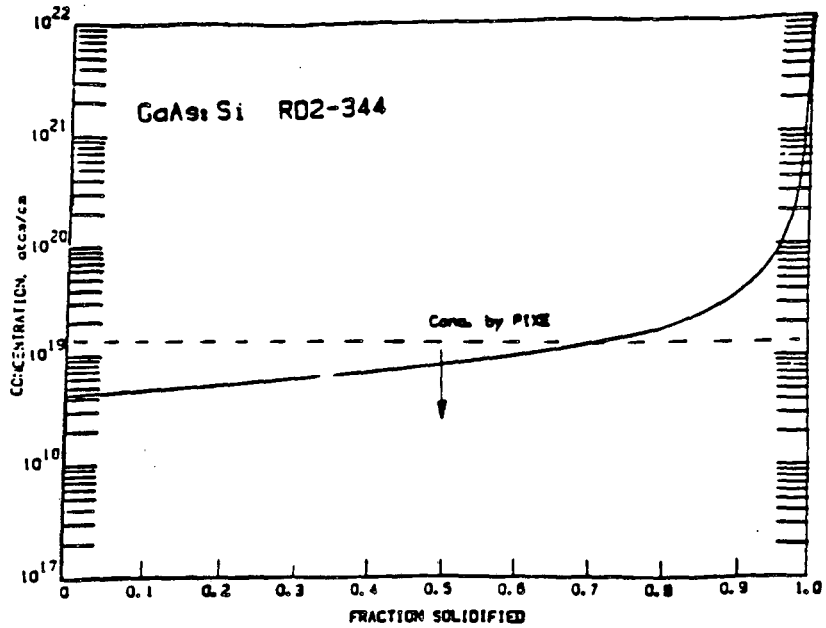

Fig. AI.5. Dopant concentration profile for crystal RD2-344 and the concentration as measured by PIXE.

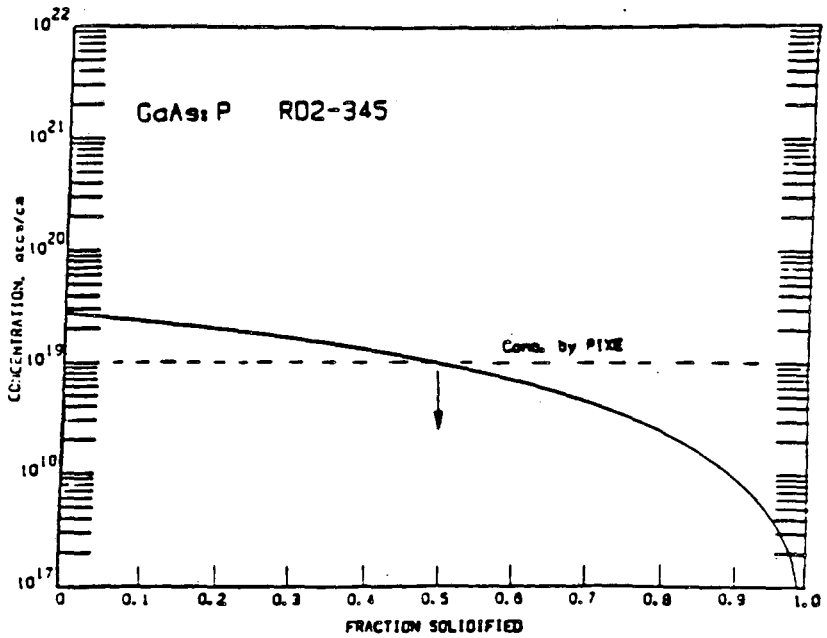

Fig. AI.6. Dopant concentration profile for crystal RD2-345 and the concentration as measured by PIXE.

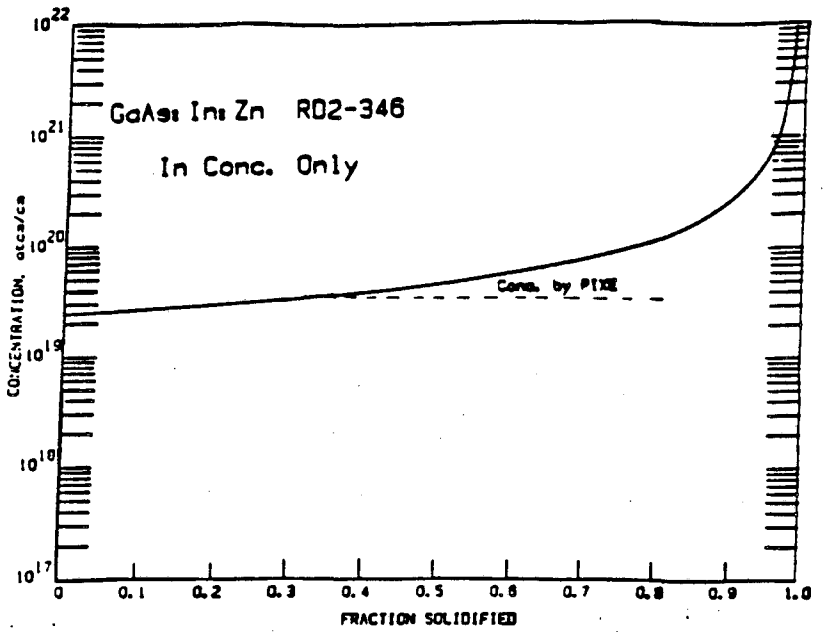

Fig. AI.7. Dopant concentration profile for In in crystal RD2-346 and the concentration of In as measured by PIXE. The profile and measured concentration for the Zn is identical to that for crystal/sample RD2-342.

APPENDIX II

Tables AII.I and AII.II list the data for a wide selection of elements in GaAs. The data was used in Eq. 37 to determine the dopant concentrations and the minimum detectable limit.

TABLE AII.I

PIXE ANALYSIS DATA

Matrix: GaAs
Projectile: proton

$\Omega/4\pi = 7.75\times10^{-5}$ sr
Energy: 1.0 MeV

Z	X-Ray	Binding/X-ray Energy (keV)	α, air, 1/cm	I 3mm	α, Be, 1/cm	I 3mil	α, GaAs, 1/cm	ω	$\omega\sum\sigma(x)e^{-\alpha x}$ (cm^2)
13 Al	K-α	1.56/1.49	1.582	0.62	342.3	0.074	31915	0.039	2.97E-26
14 Si	K-α	1.84/1.74	0.925	0.75	194.3	0.228	22650	0.050	2.83E-26
15 P	K-α	2.14/2.02	0.636	0.83	120.3	0.340	13050	0.063	3.29E-26
16 S	K-α	2.47/2.31	0.417	0.88	79.6	0.545	10730	0.078	2.88E-26
19 K	K-α	3.61/3.13	0.157	0.95	25.5	0.823	3974	0.140	2.91E-26
20 Ca	K-α	4.04/3.70	0.120	0.96	18.5	0.869	2988	0.163	2.74E-26
24 Cr	K-α	5.99/5.41	0.033	0.99	5.92	0.956	1067	0.275	1.74E-26
26 Fe	K-α	7.11/6.40	0.020	0.99	3.70	0.972	645	0.340	1.23E-26
28 Ni	K-α	8.33/7.48	0.012	0.99	2.50	0.981	443	0.406	7.84E-27
29 Cu	K-α	8.98/8.05	0.010	0.99	1.94	0.985	382	0.440	6.15E-27
30 Zn	K-α	9.66/8.14	0.008	0.99	1.54	0.989	295	0.474	4.90E-27

Z	X-Ray	Binding/X-ray Energy (keV)	α, air, 1/cm	I 3mm	α, Be, 1/cm	I 3mil	α, GaAs, 1/cm	ω	$\omega\Sigma\sigma(x)e^{-\alpha x}$ (cm^2)
31 Ga	K-α	10.4/9.25	0.007	0.99	1.39	0.990	249	0.507	3.81E-27
32 Ge	K-α	11.1/9.89	0.006	0.99	1.11	0.992	211	0.535	2.92E-27
33 As	K-α	11.9/10.5		0.99		0.993	640	0.562	1.90E-27
34 Se	K-α	12.7/11.2		0.99		0.995	152	0.589	1.73E-27
35Br	K-α	13.5/11.9		0.99		0.997	537	0.618	1.04E-27
30 Zn	L-α	1.07/1.01	4.459	0.26	1073	0.0003	26507	0.008	1.14E-25
31 Ga	L-α	1.17/1.09	3.645	0.34	870	0.0013	8599	0.009	2.39E-25
32 Ge	L-α	1.28/1.19	2.922	0.42	703	0.0047	27800	0.010	7.41E-26
33 As	L-α	1.39/1.28	2.232	0.51	537	0.017	22523	0.011	5.95E-26
35 Br	L-α	1.62/1.38	1.567	0.63	342	0.074	32546	0.014	3.99E-26
36 Kr	L-α	1.75/1.59	1.17	0.70	268	0.130	29420	0.015	3.59E-26
37 Rb	L-α	1.89/1.69	1.07	0.73	226	0.179	24751	0.017	3.44E-26
38 Sr	L-α	2.03/1.81	0.87	0.77	178	0.260	20470	0.018	3.30E-26
39 Y	L-α	2.17/1.92	0.74	0.80	147	0.328	17158	0.019	3.04E-26
40 Zr	L-α	2.32/2.04	0.63	0.83	122	0.394	14158	0.022	3.19E-26
42 Mo	L-α	2.64/2.30	0.46	0.87	85.1	0.523	11669	0.027	2.81E-26
43 Tc	L-α	2.80/2.42	0.38	0.89	69.4	0.590	9254	0.029	2.93E-26

Z	X-Ray	Binding/X-ray Energy (keV)	α, air, 1/cm	I 3mm	α, Be, 1/cm	I 3mil	α, GaAs, 1/cm	ω	$\omega\sum\sigma(x)e^{-\alpha x}$ (cm^2)
44 Ru	L-α	2.97/2.56	0.33	0.91	58.3	0.641	7956	0.032	2.92E-26
46 Pd	L-α	3.32/2.84	0.24	0.93	42.0	0.726	6130	0.037	2.69E-26
49 In	L-α	3.91/3.29	0.16	0.95	27.4	0.812	4173	0.047	2.44E-26
50 Sn	L-α	4.12/3.44	0.14	0.96	23.1	0.840	2163	0.055	3.95E-26
55 Cs	L-α	5.28/4.29	0.07	0.98	11.8	0.914	2020	0.077	1.97E-26
60 Nd	L-α	6.58/5.23	0.04	0.99	6.48	0.952	1161	0.104	1.40E-26
65 Tb	L-α	8.00/6.28	0.02	0.99	4.07	0.970	880	0.138	8.42E-27
70 Yb	L-α	9.59/7.41	0.013	0.99	2.41	0.982	444	0.181	5.84E-27
72 Hf	L-α	9.92/7.90		0.99	2.04	0.985	379	0.202	5.71E-27
73 Ta	L-α	10.6/8.15		0.99	1.85	0.986	350	0.213	4.33E-27
74 W	L-α	11.0/8.40		0.99	1.73	0.987	327	0.224	3.89E-27
76 Os	L-α	11.7/8.91		0.99	1.47	0.989	278	0.227	2.90E-27
80 Hg	L-α	13.4/9.99		0.99	1.09	0.992	205	0.262	1.80E-27

TABLE AII.II

PIXE ANALYSIS DATA

Matrix: GaAs
Projectile: proton

$\Omega/4\pi = 7.75\times10^{-5}$ sr
Energy: 1.5 MeV

Z	X-Ray	Binding/X-ray Energy, (keV)	α, air, 1/cm	I 3mm	α, Be, 1/cm	I 3mil	α, GaAs, 1/cm	ω	$\omega\sum\sigma(x)e^{-\alpha x}$ (cm^2)
13 Al	K-α	1.56/1.49	1.582	0.62	342.3	0.074	31915	0.039	4.69E-26
14 Si	K-α	1.84/1.74	0.925	0.75	194.3	0.228	22650	0.050	4.71E-26
15 P	K-α	2.14/2.02	0.636	0.83	120.3	0.340	13050	0.063	5.73E-26
16 S	K-α	2.47/2.31	0.417	0.88	79.6	0.545	10730	0.078	5.24E-26
19 K	K-α	3.61/3.13	0.157	0.95	25.5	0.823	3974	0.140	5.74E-26
20 Ca	K-α	4.04/3.70	0.120	0.96	18.5	0.869	2988	0.163	6.22E-26
24 Cr	K-α	5.99/5.41	0.033	0.99	5.92	0.956	1067	0.275	3.73E-26
26 Fe	K-α	7.11/6.40	0.020	0.99	3.70	0.972	645	0.340	2.75E-26
28 Ni	K-α	8.33/7.48	0.012	0.99	2.50	0.981	443	0.406	1.82E-26
29 Cu	K-α	8.98/8.05	0.010	0.99	1.94	0.985	382	0.440	1.46E-26
30 Zn	K-α	9.66/8.14	0.008	0.99	1.54	0.989	295	0.474	1.19E-26

Z	X-Ray	Binding/X-ray Energy (keV)	α, air, 1/cm	I 3mm	α, Be, 1/cm	I 3mil	α, GaAs, 1/cm	ω	$\omega\Sigma\sigma(x)e^{-\alpha x}$ (cm^2)
31 Ga	K-α	10.4/9.25	0.007	0.99	1.39	0.990	249	0.507	9.37E-27
32 Ge	K-α	11.1/9.89	0.006	0.99	1.11	0.992	211	0.535	7.33E-27
33 As	K-α	11.9/10.5		0.99		0.993	640	0.562	4.29E-27
34 Se	K-α	12.7/11.2		0.99		0.995	152	0.589	4.46E-27
35Br	K-α	13.5/11.9		0.99		0.997	537	0.618	2.73E-27
30 Zn	L-α	1.07/1.01	4.459	0.26	1073	0.0003	26507	0.008	1.80E-25
31 Ga	L-α	1.17/1.09	3.645	0.34	870	0.0013	8599	0.009	3.82E-25
32 Ge	L-α	1.28/1.19	2.922	0.42	703	0.0047	27800	0.010	1.23E-25
33 As	L-α	1.39/1.28	2.232	0.51	537	0.017	22523	0.011	1.01E-25
35 Br	L-α	1.62/1.38	1.567	0.63	342	0.074	32546	0.014	7.12E-26
36 Kr	L-α	1.75/1.59	1.17	0.70	268	0.130	29420	0.015	6.55E-26
37 Rb	L-α	1.89/1.69	1.07	0.73	226	0.179	24751	0.017	6.41E-26
38 Sr	L-α	2.03/1.81	0.87	0.77	178	0.260	20470	0.018	6.26E-26
39 Y	L-α	2.17/1.92	0.74	0.80	147	0.328	17158	0.019	5.88E-26
40 Zr	L-α	2.32/2.04	0.63	0.83	122	0.394	14158	0.022	6.05E-26
42 Mo	L-α	2.64/2.30	0.46	0.87	85.1	0.523	11669	0.027	5.18E-26
43 Tc	L-α	2.80/2.42	0.38	0.89	69.4	0.590	9254	0.029	6.02E-26

Z	X-Ray	Binding/X-ray Energy (keV)	α, air, 1/cm	I 3mm	α, Be, 1/cm	I 3mil	α, GaAs, 1/cm	ω	$\omega\sum\sigma(x)e^{-\alpha x}$ (cm^2)
44 Ru	L-α	2.97/2.56	0.33	0.91	58.3	0.641	7956	0.032	6.07E-26
46 Pd	L-α	3.32/2.84	0.24	0.93	42.0	0.726	6130	0.037	5.71E-26
49 In	L-α	3.91/3.29	0.16	0.95	27.4	0.812	4173	0.047	5.29E-26
50 Sn	L-α	4.12/3.44	0.14	0.96	23.1	0.840	2163	0.055	8.25E-26
55 Cs	L-α	5.28/4.29	0.07	0.98	11.8	0.914	2020	0.077	4.37E-26
60 Nd	L-α	6.58/5.23	0.04	0.99	6.48	0.952	1161	0.104	3.18E-26
65 Tb	L-α	8.00/6.28	0.02	0.99	4.07	0.970	880	0.138	1.99E-26
70 Yb	L-α	9.59/7.41	0.013	0.99	2.41	0.982	444	0.181	1.43E-26
72 Hf	L-α	9.92/7.90		0.99	2.04	0.985	379	0.202	1.41E-26
73 Ta	L-α	10.6/8.15		0.99	1.85	0.986	350	0.213	1.09E-26
74 W	L-α	11.0/8.40		0.99	1.73	0.987	327	0.224	9.86E-27
76 Os	L-α	11.7/8.91		0.99	1.47	0.989	278	0.227	7.44E-27
80 Hg	L-α	13.4/9.99		0.99	1.09	0.992	205	0.262	4.74E-27

[AF 77] Appleton BR and Foti G, "Channeling" in: Ion Beam Handbook for Materials Analysis Mayer JW and Rimini E, ed. (NY: Academic Press, 1977), pp. 69-85.

[AJ 67] Anderson JU, K. Vidensk. Selsk., Mat.-Fys. Medd. 30, 7 (1967).

[AJ 81] Anderson JU, et al, Appl. Phys. Lett. 39, (9) (1981).

[AZ 77] Anderson HH and Ziegler JF, Hydrogen: Stopping Powers and Ranges in all Elements (NY: Pergamon press, 1977).

[BF 75] Bontemps A and Fontenille J, Phys. Lett. 55A, 6 (1976).

[BJ 71] Barrett J, Phys. Rev. B3, 5 (1971).

[BK 05] Bragg WH and Kleeman R, Phil. Mag. 10, 5318 (1905).

[BM 55] Blackman M, in Encyclopedia of Physics, Part I Vol 7, Flugge S, ed. (Springer, Berlin 1955).

[BP 82] Bhattacharya R and Pronko PP, Appl. Phys. Lett. 40, 10 (1982).

[BP 83] Bhattacharya RS and Pronko PP, Nucl. Inst. Meth. Phys Res. 218, (1983) pp. 515-518.

[BW 72] Bambynek W, et al, Rev. Mod. Phys. 44, 716 (1972).

[CB 78] Cullity BD, Elements of X-Ray Diffraction, 2nd ed., (Addison-Wesley Publ. Co., Inc. 1978).

[CC 81] Chaudhri MA and Crawford A, Nucl. Inst. Meth. 181, (1981) pp. 31-35.

[CF 75] Cairns JA and Feldman LC, "Ion-Induced X-Rays in Solids," in: New Uses of Ion Accelerators, Ziegler J, ed. (NY: Plenum Press 1975).

[CMN 78] Chu WK, Mayer JW, Nicolet MA, Backscattering Spectrometry, (NY: Academic Press 1978).

[DN 73] Dyson NA, X-Rays in Atomic and Nuclear Physics, (London: Longman Group, Ltd. (1973).

[EK 83] Kern E, Solid State Technology, (1983).

[FF 74] Folkmann F, et al, Nucl. Inst. Meth. 116, (1974) pp. 487-499.

[FKS 77] Feldmann LC, Kauffman R, and Silverman PJ, Phys. Rev. Lett. 39, 1 (1977).

[FMP 82] Feldman LC, Mayer JW, and Picraux ST, Materials Analysis by Ion Channeling, (NY: Academic Press 1982).

[GD 74] Gemmell D, Rev. Mod. Phys. 46, 1 (1974).

[GGK 81] Garten RPH, et al, Nucl. Inst. Meth. 181, (1981) pp. 185-188.

[GJ 73] Garcia JD, e Rev. Mod. Phys. 45, 2 (1973).

[GM 47] Moliere' G, Z. Naturforsch 2a, 133 (1947).

[HL 80] Hollan L, et al, "The Preparation of Gallium Arsenide," in: Current Topics in Materials Science, Vol. 5, Kaldis E, ed., (North-Holland Pub. Co. 1980).

[HM 81] Hill MW, et al, Nucl. Inst. Meth. 181, (1981) pp. 31-35.

[HT 86] Haga T, et al, Proc. from 4th Conf. on Semi-Insulating III-V Mat., Hakone, Japan, May 18-21, 1986.

[JG 73] Goulding FS and Jaklevic JM, "Photon-Excited Energy Dispersive X-Ray Fluorescence Analysis for Trace Elements" in: Annual Reviews of Nuclear Science, Segre, E ed., (Palo Alto: Annual Reviews, Inc. 1973) pp. 45-74.

[JJ 76] Johansson SA and Johansson TB, Nucl. Inst. Meth. 137, (1976) pp. 473-516.

[JJ 86] Jaklevic JM, Private Communication, (1986).

[KC 76] Kittel C, Introduction to Solid State Physics, 5th ed., (NY: John Wiley and Sons, Inc. 1976).

[KMY 84] Man-Yu K, "Heavy Ion Rutherford Backscattering Spectrometry for Near Surface Characterizaton of Electronic Materials" (MS Thesis), Dept. Mat. Sci., Univ. of Calif., Berkeley, Calif. (1984).

[LJ 65] Lindhard J, Mat. Fys. Medd. Dan. Vid. Selsk. 34, 14, 1 (1965).

[LS 61] Lindhard J and Scharff M, Phys. Rev. 124, 128 (1961).

[MA 62] Messiah A, Quantum Mechanics, (NY: J. Wiley 1962).

[ML 58] Merzbacher E and Lewis HW, Handbuch der Physik, 34, Flugge S, ed., (Berlin: Springer Verlag 1958) p. 61.

[MM 65] Mott NF and Massey SN, The Theorey of Atomic Collisions, 3rd ed., (London: Oxford Press 1965).

[PB 83] Pronko PP and Bhattacharya RS, IEEE Trans. Nucl. Sci. NS-30, 2 (1983).

[PP 78] Price PB, et al, Radiation Effects 39, (1978) pp. 205-212.

[PST 69] Picraux ST, et al, Phys. Rev. 180, 3 (1969) pp. 873-882.

[RF 84] Richter FW, Nucl. Inst. Meth. Phys. Res. B3, (1984) pp. 105-113.

[RW 81] Richter FW and Watjen U, Nucl. Inst. Meth. 181, (1981) pp. 189-194.

[SM 83] Sarkar M, Nucl. Inst. Meth. 214, (1983) pp. 557-559.

[TBE 86] Tabache MG, Bourret ED, Elliot AG, Appl. Phys. Lett. 49, 5, (1986).

[VV 73] Valkovic V, Contemp. Phys. 14, 5 (1973) pp. 415-438.

[WR 77]. Willis RD, et al, Nucl. Inst. Meth. 142, (1977) pp. 67-77.

This report was done with support from the Department of Energy. Any conclusions or opinions expressed in this report represent solely those of the author(s) and not necessarily those of The Regents of the University of California, the Lawrence Berkeley Laboratory or the Department of Energy.

Reference to a company or product name does not imply approval or recommendation of the product by the University of California or the U.S. Department of Energy to the exclusion of others that may be suitable.

LAWRENCE BERKELEY LABORATORY
TECHNICAL INFORMATION DEPARTMENT
UNIVERSITY OF CALIFORNIA
BERKELEY, CALIFORNIA 94720